DETERMINATION OF CRYSTALLITE PARAMETERS OF TITANIUM DIOXIDE DOPED ZINC OXIDE NANOPARTICLES

by

ROXANA JAHAN

FARIHA BINTA HYDER

SANJIDA NAJNIN

BACHELOR OF SCIENCE IN ELECTRICAL AND ELECTRONIC ENGINEERING

Department of Electrical and Electronic Engineering
INTERNATIONAL ISLAMIC UNIVERSITY CHITTAGONG

DECEMBER 2021

DETERMINATION OF CRYSTALLITE PARAMETERS OF TITANIUM DIOXIDE DOPED ZINC OXIDE NANOPARTICLES

by

ROXANA JAHAN

FARIHA BINTA HYDER

SANJIDA NAJNIN

A thesis
submitted as partial fulfillment of the requirement for the degree of

BACHELOR OF SCIENCE IN ELECTRICAL AND ELECTRONIC ENGINEERING

Department of Electrical and Electronic Engineering
INTERNATIONAL ISLAMIC UNIVERSITY CHITTAGONG

DECEMBER 2021

CERTIFICATE OF APPROVAL

The thesis entitled as **"Determination of crystallite parameters of Titanium Dioxide (TiO_2) doped ZnO nanoparticles"** submitted by **Fariha Binta Hyder,** bearing Matric ID. **ET171202** and **Sanjida Najnin,** bearing Matric ID. **ET171203,** and **Roxana Jahan**, bearing Matric ID**. ET171207** of session **Autumn 2020**, to the Department of Electrical and Electronic Engineering, International Islamic University Chittagong, has been accepted as satisfactory in partial fulfilment of the requirements for the degree of Bachelor of Science in Engineering and approved for the examination held on **24 December, 2021**.

Supervisor
Dr. Mohammad Shamimul Haque Choudhury
Associate Professor,
Department of Electrical and Electronic Engineering
International Islamic University Chittagong.

DECLARATION

It is hereby declared that this work has been done by me and no portion of the work contained in this thesis has been submitted elsewhere for the award of any degree or diploma.

Fariha Binta Hyder

Sanjida Najnin

Roxana Jahan

ACKNOWLEDGMENT

Alhamdulillah, all praises and gratitude to Allah for giving us strength and helping us to complete this work.

This thesis has been kept on track and been seen through to completion with the support and encouragement of the following persons and at the end of our thesis, we would like to thank all those people who made this thesis possible and an unforgettable experience for us. First and foremost, we pay our gratitude to our supervisor, Dr. Md. Shamimul Haque Choudhury for guiding and providing us necessary infrastructure and resources to accomplish our research work. This work would not have been possible without his guidance, support and encouragement. Under his guidance we successfully overcame many difficulties and learned a lot. We would like to express our deep gratitude to him for providing us the data we needed for this work and his advice, guidance, patience & understanding throughout whole period of conducting the research. We are especially indebted to him in this regard as we got the chance to develop our skill on how to conduct research and use statistical software. At this Juncture we think of our parents whose selfless sacrificial life and their great efforts with pain and tears and unceasing prayer has enabled us to reach the present position in life. we should not forget to acknowledge brother and sisters for their continuous love, support, understanding and good wishes whenever we needed. We are thankful to the faculty members of department of EEE for their kind support in this regard. We owe to all those authors and researchers whose work. I used in designing the research and in preparing this dissertation. Finally, we thank all those who have helped us directly or indirectly in the successful completion of our thesis. Anyone missed in this acknowledgement are also thanked.

Authors

ABSTRACT

In this thesis, we report on crystallite parameters of Zinc Oxide nanoparticles doped with several concentrations of P25 type Titanium dioxide (TiO_2). The films were prepared using conventional Doctor Blade coating method along with hot-compression as an effective post-deposition treatment. For the characterization of the films, X-ray Diffraction (XRD) techniques were used. For new material enacting, the XRD method is a very dynamical technique used in modern applied science. Crystallite attributes such as crystallite size, lattice strain, stress and energy density were more effectively evaluated for all of the XRD reflection peaks communicating to the wurtzite hexagonal phase of ZnO operating a modified form of the methods including the Wagner-Agua technique, Halder-Wagner method, Size-Strain Plot, and the Williamson-Hall (W-H) models. Comparisons of the effect were made to see the result of unlike doping percentage on the crystallite parameters. Reasoning appear that ZnO nanoparticles were crystallite in nature with a hexagonal wurtzite phase and the crystallinity was not harmed by absorbing Titanium dioxide (P25). Crystallite dimension got from all the methods were almost similar excluding Halder-Wagner method which appears a much lower value of crystallite size compared to other methods. All these methods recognize that while the Titanium dioxide (P25) concentration rises, the crystallite dimension rises and the lattice strain drops. Among all the methods SSP and Wagner-Agua method appears more correct values while the points fit the linear line strongly preferable compared to other methods. But, change in many crystallite characteristics caused by dissimilar percentage of Titanium dioxide (P25) was observed to explain the effect of doping on crystallite parameters. The changes in various crystallite parameters can effect greatly on the device performance.

TABLE OF CONTENTS

LIST OF TABLES

LIST OF FIGURES

LIST OF ABBREVIATIONS

TiO_2	Titanium dioxide
XPPA	X-ray Peak Profile Analysis
NP	Nanoparticle
ZnO	Zinc Oxide
SEM	Scanning Electron Microscope
TEM	Transmission Electron Microscope
EPR	Electron Spin Resonance
FTIR	Fourier Transform Infrared Spectroscopy
XRD	X-ray Diffraction
PEN	Polyethylene naphthalate
DSCs	dye-sensitized solar cells
T	℃ temperature
MPa	Mega pascal
UDM	Uniform Deformation Model
USDM	Uniform Stress Deformation Model
UDEDM	Uniform Deformation Energy
SSP	Size-Strain Plot
H-W	Halder-wagner
W-A	Wagner-agua
LED	Light Emitting Devices
DLS	Dynamic Light Scattering

CHAPTER 1
INTRODUCTION

1.1 Introduction

Research on physics and engineering, solid-state materials has taken capital stage in recent discoveries. The safety and life style of mankind has reformed after the determining of semiconducting materials. The features and applications of semiconductor in communication, military equipment, medical equipment, security, and entertainment industries. Semiconducting nano materials are receiving considerable observation because of their novel optical, electronic and magnetic properties for applications in the field of solar cells (photovoltaic cells), optical planer wave guides, electronics, catalysis, optical communication, energy storage, sensing, data storage, transmission, environmental protection, cosmetics, and Light emitting devices (LED) [1].

The properties of nanoscale material are different than their bulk equivalents because of the high surface-to-volume ratio, at the molecular level an exponential increase in reactivity because of that. Some of them are Electronic, optical, and chemical properties, although the mechanical properties of nanoparticles (NPs) can also vary greatly [4]. Becauseof their academic profits and the potential technical applications in different fields, they can be the subject of intense research. A variety of methods, including mechanical, chemical, and other pathways, can be used to create such nano structures [5]. nanoparticles are particles that are fewer than 100 nano metres in size on a one-dimensional scale. The characteristics of nanoparticles vary as they are employed to make traditional materials. While a bulk material's physical characteristics should be constant irrespective of its height, nano scale size dependencies are often found [6]. Asa result, as a material's size reaches the nano scale and the percentage of atoms on its surface begins to become important, its properties typically change.

The synthesis, characterization, and application of semiconductor nanoparticles, which are fundamental in many new technologies, has recently sparked a lot of interest. Because of their large surface area or quantum size effect, when semiconductor materials are reduced to the nano scale, their physical and chemical properties change dramatically, resulting in unique properties. The semiconductor's conductivity as well

as its optical properties (absorption coefficient and refractive index) can be modified. Semiconductor nano materials and devices are still in the research stage, but they have the potential to be used in a variety of fields such as solar cells, nano scale electronic devices, light-emitting diodes, laser technology, wave guide, chemical and biosensors, packaging films, super absorbents, armour, automobile parts, and catalysts.

Zinc oxide (ZnO) based flexible dye-sensitized solar cell (DSCs) have drawn the interest of the research community because of its superior fundamental physical properties suchas long carrier lifetime, wide band gap, high electron mobility and better chemical stability [7]-[11]. ZnO has wide gap (3.37 eV), high mobility of electron, high exciton banding energy, long carrier life, an electronic band structure similar to TiO_2, and outstanding chemical stability, causing an intense interest in the application for the dye-sensitized solar cell (DSC) [12].

To improve photo-current density and efficiency of power conversion, research into the fabrication and manipulation of the nano-sized ZnO has therefore been extremely attractive. Enhancing charge collecting efficiency, suppressing recombination and charge transport, have all been used to dope metal oxides. When the concentration of doping exceeds the solubility of the host crystal's functional nano structures, doped impurities tend to aggregate on the surface of the host material during crystal formation.[13].

There are several material characterization techniques i.e. scanning electron microscopy (SEM), Transmission electron microscopy (TEM), X -ray diffraction (XRD), Fourier Transforms Infrared Spectroscopy (FTIR), UV-visible spectroscopy, Dynamic lightscattering (DLS). X-ray diffraction (XRD) is used to measure crystalline compounds and provides a quantitative and qualitative analysis of compounds that cannot be measured by other means. By shooting an X-Ray at a compound, XRD can measure the diffraction of the beam from different sections of the compound. This measurement can then be used to understand the composition of the compound on an atomic level, since all compounds diffract the beam differently. XRD measurements show structural make-up, content a size of crystalline structures. However, it has size limitations. It is much more accurate for measuring large crystalline structures rather than small ones. Small structures that are present only in trace amounts will often go undetected by XRD readings, which can resultin skewed results [14]

1.2 Objectives

- Characterization of ZnO nanoparticles with different percentage of Titanium dioxide (TiO_2) doping by XRD Technique and determine crystallite parameters namely crystal size, lattice strain, stress, energy density etc.
- Characteristics of different X-ray Peak Profile Analysis (XPPA) methods i.e. Williamson-Hall method (UDM, USDM and UDEDM), Size-Strain Plot (SSP) method, Halder-Wagner method and Wagner-Agua method at different doping Titanium percentage.
- Comparison of Geometrical parameters of ZnO nanoparticles with and without Titanium dioxide (P25) doping.

1.3 Outline of this work

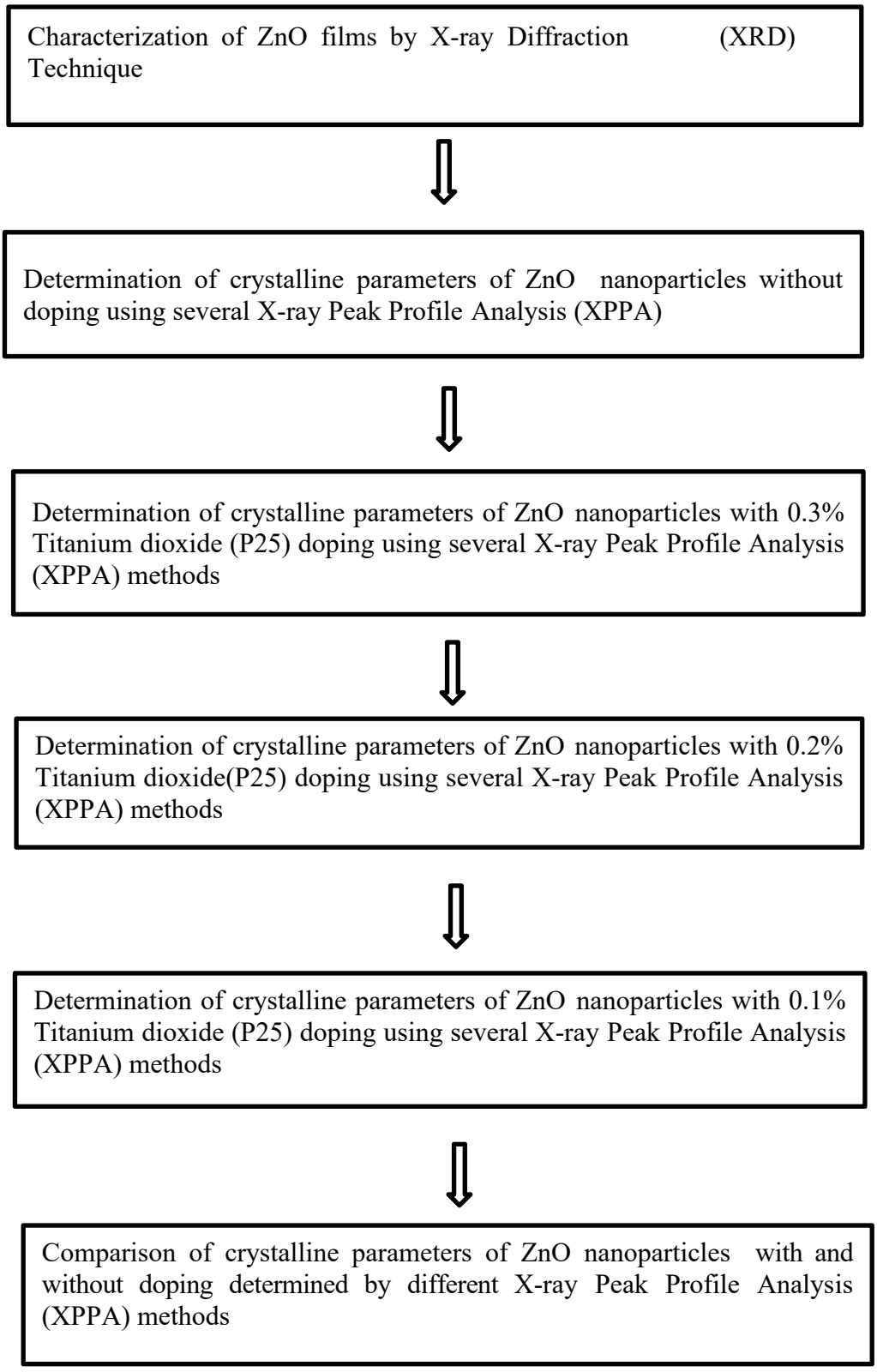

Fig. 1.1 Outline of this thesis work.

1.4 Thesis Layout

- ✓ This thesis is organized by six different chapters.
- ✓ Chapter one provides a general introduction and objectives of this study.
- ✓ Chapter two discusses about literature review, introduction of ZnO, the underlying theories and fundamental properties of ZnO. It also explains different application of ZnO. A summary of different material characterization techniques is also presented in this chapter.
- ✓ Chapter three gives a brief description of the X-ray Diffraction (XRD) techniques.
- ✓ Chapter four provides the exploration of experimental work and methodology conducted to estimate the value of different parameters.
- ✓ Chapter five presents analysis of the results obtained and compared different crystallite parameters of ZnO films without doping and at different TiO_2 doping percentage.
- ✓ Chapter six provides the summary according to the finding of this study. In addition, some limitations and suggestion for future researchers also discuss there.

CHAPTER 2

LITERATURE REVIEW

2.1 Introduction

Semiconductor nanoparticles have attracted much attention in the past decade because of their unusual photonic characteristics. When the size of semiconductor materials is reduced to nanoscale, their physical and chemical properties change drastically, resulting in unique properties due to their large surface area or quantum size effect. Nanoparticles,particles of material with diameters in the range of 1 to 20 nm, exhibit unique physical properties that give rise to many potential applications in areas such as nonlinear optics, luminescence, electronics, catalysis, solar energy conversion, and optoelectronics.

Nanoparticles are significant research materials for biotechnology and pharmacology applications. They connect the fields of bulk materials and molecular structures. While the physical properties of bulk materials remain constant regardless of size, the physicaland chemical properties of nanoparticles are determined by their size. As a material's size approaches nanoscale proportions and the percentage of atoms at the surface of a material becomes important, its properties change [15].

In the field of materials science, Zinc oxide (ZnO) holds a very important position because of its transparency in the visible range with wide band gap, optical and electrical properties, high chemical and mechanical stability. Due to its abundance in nature, it is considered as a lower cost material compared to the most currently used transparent conductive oxide materials. Zinc oxide (ZnO) is a direct band gap, II-VI compound semiconductor material with many promising properties for blue/UV optoelectronics, transparent electronics, spintronic devices and sensor applications. Fromall the oxide materials studied, in the recent years, the ZnO has emerged as one of the most promising materials that attracted much attention within the scientific c*ommunity as a ‘future material’.

For the combination of ZnO nanomaterials, several combination techniques are used, along with bottom-up approaches including sol-gel, chemical precipitation, and top-down ball milling. Precipitation produces a high-quality, high-purity nano

powder. In this analysis the enactment of ZnO nanoparticles was completed, and the particle size was deliberated using the XRD technique.

2.2 Nanoparticles

Nanoparticles are particles that have one dimension that is 100 nanometers or less in size. The properties of many conventional materials change when formed from nanoparticles. This is typically because nanoparticles have a greater surface area per weight than larger particles; this causes them to be more reactive to certain other molecules. Nanoparticles are used, or being decided for use, in variety fields.

Nanoparticles are of considerable interest to scientists because they act as a contact between bulk materials and atomic or molecular structures. The physical properties of a bulk material should remain constant regardless of its size, but size-dependent properties are often observed at the nanoscale. As a result, as the size of a material reaches the Nano scale and the percentage of atoms on its surface begins to become important, the properties of the material change. The interesting and sometimes unexpected properties of nanoparticles are therefore largely due to the large surface area of the material, which dominates the contributions made by the small bulk of the material. Nanoparticles often possess unexpected optical properties as they are small enough to confine their electrons and produce quantum effects. Other size-dependent property changes include quantum confinement in semiconductor particles, surface Plasmon resonance in some metal particles and super paramagnetism in magnetic material [16].

2.2.1 Properties of nanoparticles

- A bulk material should have constant physical properties regardless of its size, but at the Nano scale size-dependent properties are often observed. Thus, the properties of materials change as their size approaches the Nano scale and as the percentage of atoms at the surface of a material becomes significant.
- For bulk materials larger than one micrometer (or micron), the percentage of atoms at the surface is insignificant in relation to the number of atoms in the bulk of the material. The interesting and sometimes unexpected properties of nanoparticles are therefore largely due to the large surface area

of the material, which dominates the contributions made by the small bulk of the material.

- Nanoparticles of usually yellow gold and gray silicon are red in color; gold nanoparticles melt at much lower temperatures (nearly 300° C for 2.5 nm size) than the gold slabs (1064° C); and absorption of solar radiation in photovoltaic cells is much higher in materials composed of nanoparticles than it is in thin films of continuous sheets of material, the smaller the particles, the greater the solar absorption.
- Suspensions of nanoparticles are possible since the interaction of the particle surface with the solvent is strong enough to overcome density differences, which otherwise usually result in a material either sinking or coating in a liquid.
- Nanoparticles also often possess unexpected optical properties as they are small enough to confine their electrons and produce quantum effects. For example, goldnanoparticles appear deep red to black in solution.
- The high surface area to volume ratio of nanoparticles provides a tremendous driving force for diffusion, especially at elevated temperatures.
- Moreover, nanoparticles have been found to impart some extra properties to various day to day products. For example, the presence of titanium dioxide nanoparticles imparts what we call the self-cleaning effect, and the size being nanorange, the particles cannot be observed. Zinc oxide particles have been found to have superior UV blocking properties compared to its bulk substitute. This is one of the reasons why it is often used in the preparation of sunscreen lotions, andis completely photo stable.

2.2.2 Advantage of nanoparticles

The advantage of using nanoparticles include the following:

1. Because of the ability to produce different intensities of colors in solutions by adjusting the thickness of the nanoshell, the aspect ratio, and the percentage of gold, nanoparticles are widely used in bioimaging applications. For example, a 20-nm gold solution produces a wine red color, whereas a 20-nm platinum solution produces a yellowish-gray color [17].

2. Gold nanoparticles, for example, have the benefit of melting at lower temperatures (300 °C for 2.5 nm size) than their bulkier equivalents (gold slabs melt at 1064 °C).

3. Targeting ligands may be attached to the surface of particles, or magnetic guidance can be used to achieve site-specific targeting.

4. Oral, nasal, parenteral, intraocular, and other routes of administration are possible with the system.

5. It may come as a surprise, but the rubber industry uses more than half of the Zinc Oxide produced. In the vulcanization of rubber, ZnO is combined with stearic acid to create tires, shoe soles, and even hockey pucks.

6. Antibacterial and deodorizing properties are also found in zinc oxide. As a result, it's used in medicinal products like baby powder and creams to treat things like diaper rash, other skin irritations, and even dandruff. It is also used in sunblocks and can be seen on the nose and lips of lifeguards at the beach due to its reflective properties.

2.2.3 imitation of nanoparticles

In spite of these Benefits, nanoparticles do have limitation. Until nanoparticles can be made commercially accessible, these functional issues must be resolved. The current analysis examines the most recent advances in nanoparticulate drug delivery systems, as well as surface modification problems, drug loading methods, release control, and nanoparticle applications.

- When their size is in the micrometre range, they appear on the skin as an opaque white film, causing customers to be hesitant to use sunscreens that contain them. These oxides, on the other hand, are transparent and do not show up on the skin when used as nanoparticles (NPs), but they maintain or even improve their UV-sunscreening properties [19].For example, their small size and large surface area can lead to particle aggregation, making physical handling of nanoparticles difficult in liquid and dryforms.
- In addition, small particles size and large surface area readily result in limited drugloading and burst release.
- These practical problems have to be overcome before nanoparticles can be made commercially available. The present review details the latest development of nanoparticulate drug delivery systems, surface modification issues, drug loading strategies, release control and potential applications of nanoparticles.

2.3 Zinc oxide

Zinc oxide, ZnO is an inorganic compound also known as zincite and occurs rarely in nature, generally in a crystalline form. It's a widely used semiconductor found in our daily lives. It is usually orange or red in color due to presence of manganese impurity [20]. It usually takes the form of a white crystalline powder that is nearly water insoluble. Synthetically produced ZnO contributes for the majority of commercial ZnO. The semiconductor group II-VI includes ZnO, which is a large bandgap semiconductor. Because of oxygen vacancies, the semiconductor is doped n-type. High electron mobility, excellent transparency, large bandgap for semiconductivity, high room-temperature luminescence, and so on are all advantages of this material. These characteristics are used in electrodes for liquid crystal displays, energy-saving and heat-protecting windows, electronic applications of ZnO such as thin-film transistors and light emitting diodes, and ceramics plastic. The wurtzite structure of zinc oxide (ZnO) is stable, with lattice spacing of a = 0.325 nanometers and c = 0.521 nanometers. Because of its unique properties and versatile Applications, it is used in transparent electronics, ultraviolet (UV) light emitters, piezoelectric devices and chemical sensors. These remarkable physical properties form the basis for motivation of device miniaturization, large effort has been focused on the synthesis, characterization and device applications of ZnO nano materials

2.3.1 Structure of the crystal

Hexagonal wurtzite and cubic zincblende are the two major types of zinc oxide crystallization. At ambient temperatures, the wurtzite structure is the most stable and therefore the most common. By growing ZnO on substrates with a cubic lattice structure, the zincblende shape can be stabilized. The zinc and oxide centres are tetrahedral in both cases, which is the most common geometry for Zn (II). At moderately high pressures of about 10 GPa, ZnO converts to the rocksalt motif. There is no inversion symmetry in hexagonal and zincblende polymorphs (reflection of a crystal relative to any given point does not transform it into itself). Piezoelectricity of hexagonal and zincblende ZnO, as well as pyroelectricity of hexagonal ZnO, are causedby this and other lattice symmetry properties.

The lattice constants are a = 3.25 *Å* and c = 5.2 *Å*; their ratio c/a ~ 1.60 is close to the ideal value for hexagonal cell c/a = 1.633. As in most group II-VI materials, the bondingin ZnO is largely ionic (Zn^{2+}–O^{2-}) with the corresponding radii of 0.074 *nm* for Zn^{2+} and 0.140 nm for O^{2-}. This property accounts for the preferential formation of wurtzite ratherthan zinc blende structure, as well as the strong piezoelectricity of ZnO. Because of the polar Zn-O bonds, zinc and oxygen planes are electrically charged. To maintain electrical neutrality, those planes reconstruct at atomic level in most relative materials, but not in ZnO – its surfaces are atomically flat, stable and exhibit no reconstruction. This anomaly of ZnO is not fully explained. However, studies using wurtzite structures explained the origin of surface flatness and the absence of reconstruction at ZnO wurtzite surfaces in addition to the origin of charges on ZnO planes [20]. Fig.2.1 and Fig.2.2 shows the wurtzite structure of ZnO and zinc cube blende respectively

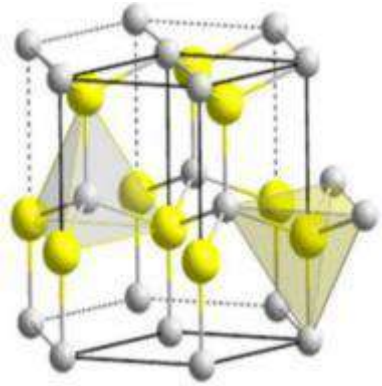

Fig. 2.1 Wurtzite structure of ZnO [21]

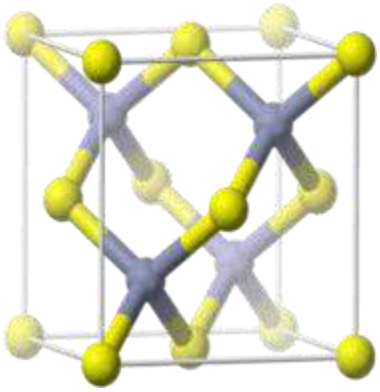

Fig. 2.2 Zinc cube blende [22]

2.3.2 Physical characteristics

Some physical characteristics of ZnO are summarized in Table 2.1 [22].

Table 2.1 Physical parameters of ZnO

Physical parameters	**Values**
Stable phase at 300 K	Wurtzite
Lattice parameters in nm at 300 K a c c/a u	 0.32495 0.52069 1.602 (ideal hexagonal structure shows 1.63) 0.345
Energy band gap (eV)	3.37, direct
Density (g/cm^3)	5.606
Refractive index	2.008−2.029
Melting point (^oC)	1975
Thermal conductivity (W/K.cm)	0.6−1.2
Exciton binding energy (meV)	60
Electron effective mass (m_o)	0.24
Electron Hall mobility at 300 *K* for low n-type conductivity (cm^2/Vs)	200
Linear expansion coefficient (/°C)	a: 6.5 ×10^{-6} and c: 3.0 × 10^{-6}
Static dielectric constant	8.656
Hole effective mass (m_o)	0.59
Hole Hall mobility at 300 *K* for low p-type conductivity (cm^2/Vs)	5–50
Intrinsic carrier concentration	<106 cm^{-3} (max n-type doping >1020 cm^{-3} electrons; max p-type doping <1017 cm^{-3} holes)

The free electron mass is denoted by the symbol m_o. Energy band gap, excitons binding energy, electron effective mass, hole effective mass, hole hall mobility, and lattice parameter are some of the physical parameters that are simple and easy to understand. It should also be remembered that some of these data are still subject to uncertainty. Since there are few records of p-type ZnO, the hole mobility and effective mass are stillup for discussion. Similarly, the values for thermal conductivity indicate a wide range of values, which may be due to defects such as dislocations.

2.3.3 Mechanical Properties

ZnO is a relatively soft material, with a hardness of just 4.5 on the Mohs scale. Its elastic constants are lower than those of other III-V semiconductors such as GaN. ZnO has a high heat ability and conductivity, low thermal expansion coefficients, and high melting points, to mention a few characteristics. Because of its higher exciton binding energy (60 meV), ZnO has been proposed as a more promising UV emitting phosphor than GaN. The maximum piezoelectric tensor is found in ZnO among the tetrahedrally bonded semiconductors. This makes it a crucial material for a wide range of piezoelectric applications that involve a high degree of electromechanical coupling. As the loading of synthesized ZnO nanoparticles is increased, the deformation is reduced. The mechanical properties such as Hardness, tensile strength, 100 percent and 300 percent modulus, tear strength, and elongation at break are all enhanced without compromising other properties [23]. A Cure Characteristics and Mechanical Properties of ZnO nano-particles as Activator in Unfilled Natural Rubber, Rudeerat Suntako1.

2.3.4 Piezoelectric effect and polar surfaces

Piezoelectricity of ZnO has been extensively studied for various applications in force sensing, acoustic wave resonator, acousto-optic modulator, etc. The origin of the piezoelectricity lies due to its crystal structure, in which the oxygen atoms and zinc atoms are tetrahedrally bonded. In such a structure which is non-centrosymmetric, the centre ofpositive charge and negative charge can be displaced due to external pressure induced lattice distortion. This displacement results in local dipole moments; thus, a macroscopic dipole moment appears over the entire crystal. In fact, among the tetrahedrally bonded semiconductors, ZnO has the highest tensor which provides a

large electro-mechanical coupling [24]. The spontaneous polarization and polar face dominated nanostructures are another consequence of the non-centrosymmetric ZnO crystal structure. The crystal structure of ZnO can be visualized as a tetrahedral bond between oxygen and zinc atoms. These tetrahedrons are stacked in a specific direction. The location of positive charge is displaced from that of negative charge in that set particular direction due to the effect of random polarization. A charged ZnO surface is the end product of this random polarization. The charged surface produces a specific nano-ring and nano-coil structure in order to minimize energy.

2.3.5 Electrical properties

The fundamental study of the electrical properties of ZnO nanostructures is crucial for developing their future applications in nanoelectronics. ZnO has a quite large band gap of 3.3 eV at room temperature. The advantages of a large band gap include higher values of breakdown voltages, sustaining large electric fields, high-temperature and high-power operations. ZnO has n-type character, in the absence of doping. Non-stoichiometry is usually the origin of n-type character. Due to defects such as oxygen vacancies and zinc interstitials, ZnO nanowires are reportedly show n-type semiconductor behaviour. The main impediment of ZnO for wide-ranging applications in electronics and photonics restswith the difficulty of p-type doping. Successful p-type doping for ZnO nanostructures will greatly enhance their future applications in nanoscale electronics and optoelectronics. P-type and n-type ZnO nanowires can serve as p-n junction diodes and light emitting diodes (LED) [25].

2.3.6 Optical properties

In the visible and near ultraviolet ranges of the spectrum, ZnO is a wide band gap semiconductor with high optical transparency and Luminescence. As a result, it's often used in light-emitting diodes and solar cells. The exciton binding energy of ZnO nanoparticles is approximately 60 meV. This means that the excitonic transition in ZnO nanoparticles will occur at room temperature as well. Furthermore, zinc oxide is both environmentally friendly and simple to synthesize [26]. Zinc oxide is transparent to visible light but absorbs intensely ultraviolet light below 3655 Å. White pigments absorb more light than other white pigments. Standard zinc oxide appears white in the visible wavelength range. The band gap energy (between the valence and conducting bands) is 3.2 eV, which is equivalent to 3655 Å photons of energy. Zinc oxide is

photo- conductive when exposed to ultra violet radiation. Doped zinc oxide is a candidate for new generations of devices because of its optical and semiconductor properties. Solar cells need a clear conductive coating, and the best materials are indium tin oxide and zinc oxide (doped). ZnO nanostructures' intrinsic optical properties are being investigated intensively that can be used in photonic devices. ZnO nano-structures' photo-luminescence (PL) spectra have been extensively studied [27]. The photo-luminescence spectra of ZnO nano-rods have revealed excitonic emissions. Quantum size confinement has been shown to increase the exciton binding energy significantly. There is a strong emission peak at 380 nm due to a band-to-band transition, as well as a green-yellow emission band dueto oxygen vacancy. ZnO nano-wire is a promising material for UV emission, according to PL spectra, but its UV lasing property is of greater importance and interest ZnO nano-wire/nano-rod is a natural candidate for optical wave-guide due to its near- cylindrical geometry and high refractive index (2.0). The excitonic recombination lowers the lasing threshold, and quantum confinement yields a significant density of states at the band edges and improves radiative efficiency, which are both advantages of ZnO nano-wire lasers. The use of dielectric nano-wires to direct optical waves has also made significant progress. ZnO nano-wires have recently been identified as a sub- wavelength optical wave-guide. ZnO nano-wire driven optically pumped light emission and was coupled into SnO2 nano-ribbon. These results suggest that ZnO nanostructuresmay be important aspects in integrated optoelectronic circuits.

2.3.7 Chemical properties

ZnO has the following chemical properties [28]:

ZnO is found in the mineral zincite and as zinc white, a white powder. Due to manganese impurity, it is typically orange or red in colour.
Crystalline zinc oxide is thermochromic, when heated, crystalline zinc oxide changes color from white to yellow, and returns to white when cooled. At high temperatures, a slight loss of oxygen causes this color shift.

Zinc oxide is amphoteric, meaning it reacts with acids as well as alkalis. It reacts with acid to form zinc sulphate, which is a well-known compound. Zincates are formed when alkali is added.

$$ZnO + 2\,HCl \rightarrow ZnCl_2 + H_2O$$

$$ZnO + 2\,NaOH + H_2O \rightarrow Na_2(Zn(OH)_4)$$

At around 1975 °C, ZnO decomposes to zinc vapor and oxygen, suggesting its high stability. ZnO is converted to Zn, which is more volatile, when heated with carbon.

$$ZnO + C \rightarrow Zn + CO$$

The following reaction is extremely important in zinc pyrometallurgy-

$$ZnO + CO \rightarrow Zn + CO_2$$

Water solubility of commercial zinc oxide is 0.005g/litre, which is measurable but poor.

2.3.8 Applications of ZnO

The inorganic compound zinc oxide (ZnO) has the formula ZnO. It comes as a white powder that is water insoluble. The mineral zincite contains ZnO, which can be found in the Earth's crust. However, the majority of commercially available ZnO is synthetic. Zinc oxide is a common ingredient in medical ointments for treating skin irritations. Zinc oxide has recently found applications in semiconductors, concrete, ceramic and glass compositions, etc. ZnO's property has its own collection of applications. ZnO's large band gap allows it to form clusters of ZnO nano-crystals and ZnO nano-wires. Synthesis of P–N homojunctions has also been documented in some literatures due to the large band gap. Many fine optical devices can be fabricated using ZnO's 60 meV free-exciton binding energy, because such ZnO's large exciton binding energy allows it to persist at room temperature and higher temperatures. Non-linear optical devices can be made with ZnO crystals and thin films because they show second- and third-order non-linear optical behavior. In general, the ability to tune the physical properties of these oxides, such as zinc oxide, becomes the driving force behind the creation of smart application devices [29]. The electrical, optical, magnetic, and chemical properties of cations with mixed valence states and anions with deficiencies can be fine-tuned by permuting and combining their two basic structural characteristics (vacancies). The numerous applications of ZnO are summarized in Fig.2.3. and Fig.2.4 shows pictorials of some applications of ZnO.

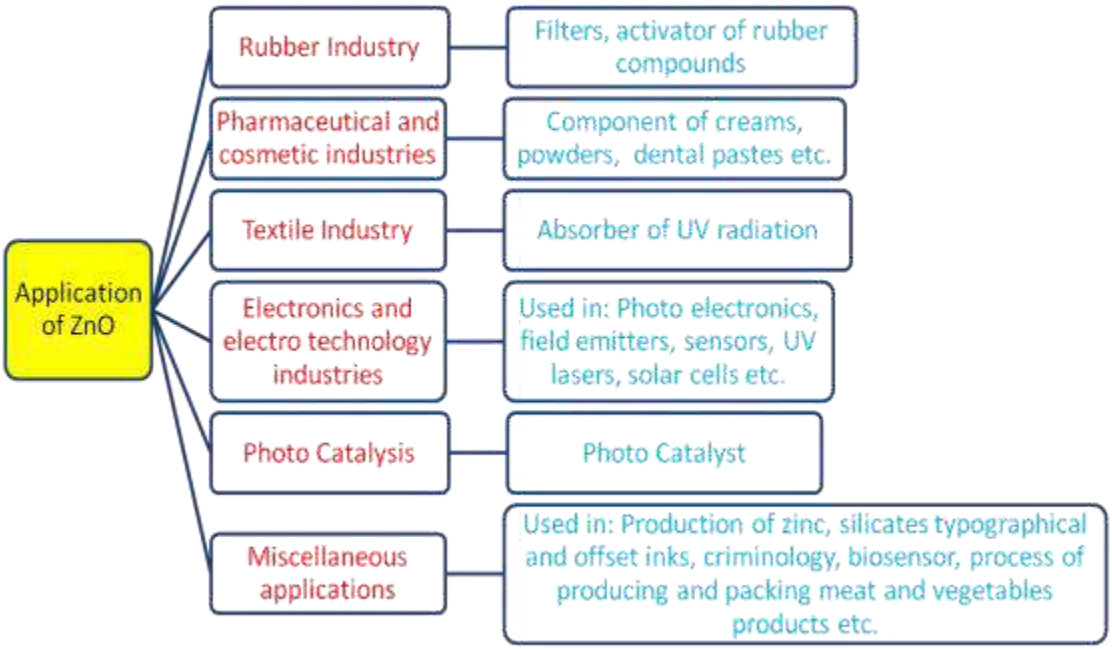

Fig. 2.3 ZnO applications are represented in schematic form [29]

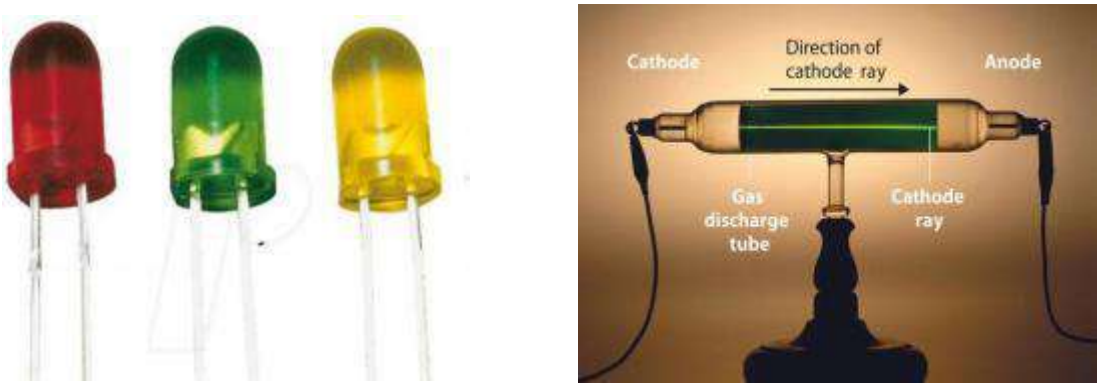

(a) (b)

Fig. 2.4 Pictorials of some applications of ZnO (a) pure green and blue LEDs (b) Cathode Ray Tube

2.3.9 ZnO Nanostructures with Morphology Control

Nanostructured materials are a class of materials having the dimensions in 1-100 nm range. This property provides greatest potential applications because of improved performance of the materials. ZnO provides a great deal of variations of particles structures among all the known materials. ZnO can occur in 1-dimension (1-D), 2 dimension (2-D) and 3-dimension (3-D) forms. One dimensional nano structures are morein number forming the largest group amongst all which includes nanorods , needles , rings, ribbons , tubes , belts , wires and combs . Zinc oxide can be obtained in 2D structures such as nanoplate, nanosheet and nanopellets . There have also been many solution basedchemicals methods which involve the calcinations step as the final step for the synthesisof hierarchical porous ZnO micro-/nano- structures.

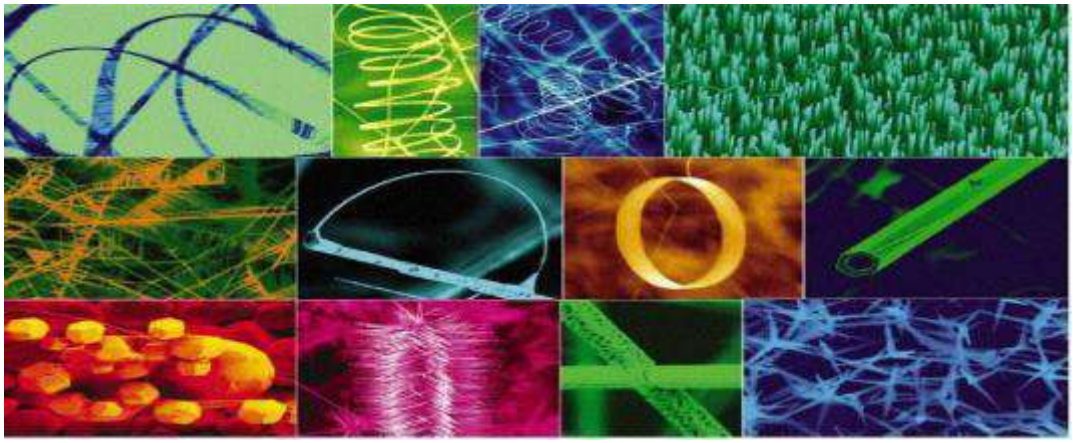

Fig. 2.5 Various nanostructures of ZnO [29].

2.4 X-ray Diffraction (XRD)

X-ray diffraction (XRD) is a powerful non-destructive technique for characterizing crystalline materials. It provides information on crystal structure, phase, preferred crystalorientation (texture), and other structural parameters, such as average grain size, crystallinity, strain, and crystal defects.Constructive interference of a monochromatic X-ray beam diffracted at specific angles from each set of lattice planes in a sample produces X-ray diffraction peaks. The distribution of atoms within the lattice is what determines the peak intensities. As a result, the fingerprint of periodic atomic arrangements in a given material is the X-ray diffraction pattern. The phase detection ofa wide range of X-ray diffraction patterns is possible using the ICDD (International Centre for Diffraction Data) data base. The Schematic diagram of X-ray Diffraction

(XRD) technique is shown in Fig. 2.6.

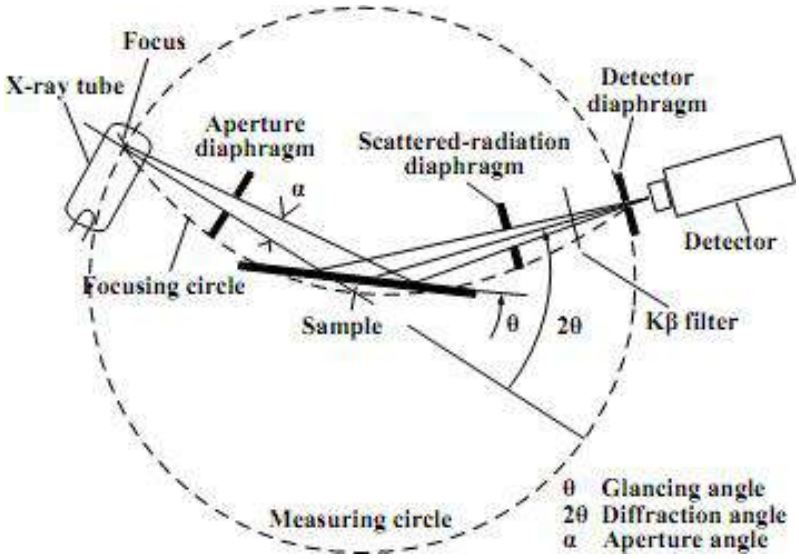

Fig. 2.6 X-ray Diffraction (XRD) technique schematic diagram [30]

This approach is crucial because, similar to how fingerprints can be used to identify a person, diffraction data can be used to identify a substance. The atomic arrangements ofthe material are determined using XRD patterns. It can also be used to differentiate between crystalline and nanocrystalline materials. The structural analysis is carried out by comparing the X-ray diffraction pattern analysis to an internationally recognized database (JCPDs).

CHAPTER 3

X-RAY DIFFRACTION

3.1 Introduction

X-ray diffraction (XRD) is a non-destructive technique for analyzing a wide range of materials, including fluids, powders, and crystals. X-ray powder diffraction (XRD) is a rapid analytical technique that can provide information on unit cell dimensions and is mainly used for phase identification of crystalline materials. XRD is an indispensable method for materials characterization and quality control, from research to manufacturing and engineering.

X-ray diffraction techniques are used for the identification of crystalline phases of various materials and the quantitative phase analysis subsequent to the identification. X-ray diffraction techniques are superior in elucidating the three-dimensional atomic structure of crystalline solids. Materials' properties and functions are primarily determined by their crystal structures. As a result, X-ray diffraction techniques have become an indispensable tool in materials research, development, and production [31].

3.2 X-ray (XRD) Diffraction's Historical Background

In 1985, Wilhelm Conrad Rontgeń, a Professor of Physics at the University of Wurzburg, Germany, discovered X-ray which enabled scientist and researchers to probe crystalline structure. Because of the centrality of radiotherapy in the marketplace during the interwar period, much effort had gone into measuring dose, the intensity of x-ray radiation. Physicists were more interested in x-ray wavelength. A crucial finding was that x-rays actually did produce interference patterns when they impinged upon and were diffracted by a crystal and historical reviews often assert that the 1912 x-ray diffraction experiment proved beyond doubt the electromagnetic wave nature of x-rays. However, the proof was demonstrated using both models of x- rays: EM radiation and the bunched-up, particle-like theory by Max von Laue, who was awarded the Nobel Prize for the discovery. Crystallographers were beginning to believe in the space-lattice-like structure of crystals at the same time, which von Laue explored with his

friend Paul Peter Ewald. In one conversation, Ewald revealed that if the approximate wavelengths were right, the spacing between lattice points might be a reasonable distance for causing X-ray interference [32]. At the same time as the diffraction spots were caused by X-rays impinging on a normal array of scatters, in this case, the repeating arrangement of atoms within the crystal, Von Laue's experiment provided evidence for the wave existence of X-rays and the space lattice of crystals. The scatters resulted in a constant series of spherical waves that interfered destructively in most directions but constructively in others, resulting in bright spots on the photographic plate [33]. The Braggs, father and son, were the ones who focused on x-rays as a crystallographic instrument, ultimately concluding that they were electromagnetic waves. Their findings confirmed that x-rays had an atomic-scale wavelength, 1000 times smaller than visible light, allowing them to interact with lattices and yield details about crystal structure that visible light could never provide. This was the first instrument to produce photographs from which solid-state atomic structures could be inferred, and it was widely used in the twentieth century. The Braggs were effective in defining very simple structures like rock salt (NaCl) [34]. In addition, studies of the intensities of x-rays reflected by crystals confirmed Niels Bohr's atomic model and a hypothesis of chemical bonding. The Braggs published a highly influential textbook on x-rays and crystal structure, educated a large number of people, and built a large collaborative network.

However, because the inference from x-ray evidence to the structure of matter was complex, the progress from simple to more complex structures was laborious. In the 1920s, molecules of inorganic chemistry were examined and in the 1930s Desmond Bernal and co-workers, such as Dorothy Crowfoot (later Hodgkin), determined the structure of sterols, and in the following decades that of other biologically interesting molecules, including penicillin and vitamin B12, were also determined. X-ray analysis always required much effort and ingenuity [34].

Structure determination by X-ray techniques, however, does not yield a clear path from experimental data to structure even today [1964]. In difficult situations, the scientist can only come up with a solution after putting in a lot of mental effort, which includes chemical awareness, creativity, and intuition. Furthermore, experimental data is often subjected to a variety of mathematical treatments, which must be tailored to the situation. Add in the fact that the more complex the structure, the larger the amount

of experimental data that must be collected and processed. It was possible to do the calculations with a pencil and paper for relatively simple compounds. Electronic computers are almost always needed nowadays, and their introduction has significantly improved the ability to perform structure determinations [34]. However, it is not always possible to simply feed in the experimental data and get the figures that provide thefinal structure; the scientist's ability to manage the data remains crucial.

X-ray analysis techniques were adopted in other life science sub-fields, such as virology, where crystalline forms of plant viruses were being prepared in the 1930s, rendering xrayanalysis feasible. Crick and Watson concluded in 1956 that a small virus comprises similar subunits that are packed together in a normal pattern. During the same time period, they worked on the structure of DNA, for which they and Maurice Wilkins were awarded the Nobel Prize in 1962. Rosalind Franklin, who died in 1958, was famously overlooked for her contribution to DNA analysis, but historians have since madeamends [35].

3.3 Bragg's Law

X-ray powder diffraction (XRD) is a versatile, non-destructive, rapid and analytical technique, which is used for phase identification of crystalline material. The basic principle involved in the diffraction method of structural analysis is the Bragg's law [35].

The basic principle behind Bragg's Law is that when it is satisfied, X-ray beams dispersed from successive planes in the crystal (as shown) can travel distances varying by exactly one wavelength (for n=1); this can be proven reasonably easily from a geometrical consideration of the above diagram. When X-rays scattered from successive planes meet the X-ray detector in this particular direction, i.e. at the angle determined by Bragg's Law, they will interact constructively, registering the passing of an extreme beam called the diffracted beam. Of course, it's the atoms with their electronic clouds that disperse the X-rays, not the planes in the crystal (since planes are abstract mathematical objects). Crystals' atoms interact with X-rays in such a way that interference results. The interaction can be compared to the waves being reflected by the atoms in a crystal structure [36]. The reflections, however, arise from the atomic planes since a crystal structure is made up of an ordered arrangement of atoms.

Consider a monochromatic X-ray beam that enters a crystal with one of its planes angled at an angle of to the incoming beam. Two such X-rays are shown in **Fig. 3.1**, where the spacing between the atomic planes occurs over the width, d.

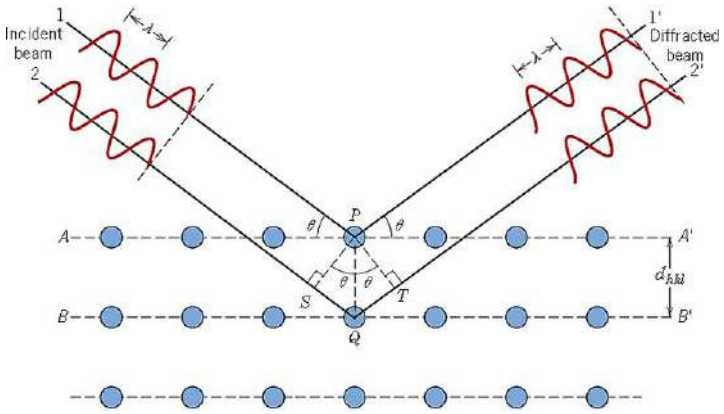

Fig. 3.1 X-rays that are monochromatic and enter a crystal [37]

Ray A reflects off of the upper atomic plane at an angle θ equal to its angle of incidence. Similarly, Ray B reflects off the lower atomic plane at the same angle θ. While Ray B isin the crystal, however, it travels a distance of 2a farther than Ray A. If this distance 2a is equal to an integral number of wavelengths (nλ), then Rays A and B will be in phase on their exit from the crystal and constructive interference will occur. If the distance 2a is not an integral number of wavelengths, then destructive interference will occur and the waves will not be as strong as when they entered the crystal. Thus, the condition for constructive interference to occur is

$$n\lambda = 2a$$

However, using trigonometry, we can calculate the distance 2a between the atomic planes in terms of the spacing d.

$$a = d \sin \theta$$

or, $2a = 2\, d\sin\theta$

Thus, $n\lambda = 2d \sin\theta$

This is known as **Bragg's Law** for X-ray diffraction [37].

It states that if we know the wavelength, λ, of the X-rays entering the crystal and can

determine the angle,θ, of the diffracted X-rays exiting the crystal, we can calculate the spacing (d-spacing) between the atomic planes.

3.4 X-ray Powder Diffraction Fundamental Principles (XRD)

In 1912, Max von Laue discovered that crystalline substances function as three-dimensional diffraction gratings for X-ray wavelengths that are close to plane spacingin a crystal lattice. The technique of X-ray diffraction plays an important role in research crystal structures and atomic spacing.

Compounds may be classified using a database of diffraction patterns since most materials have special diffraction patterns. The purity of a sample, as well as the composition of any impurities present, can be determined using its diffraction pattern. A diffraction pattern can also be used to assess and refine a crystal structure's lattice parameters. The Rietveld refinement method can be used to refine a theoretical structure. The Scherrer formula, which relates particle size to peak width, can also be used to calculate the powder particle size. Constructive interference of monochromatic X-rays and a crystalline sample is the basis of X-ray diffraction. A cathode ray tube produces the X-rays, which are then filtered to produce monochromatic radiation, collimated to focus the beam, and guided at the sample. When Bragg's Law ($n\lambda=2d\sin\theta$) is satisfied, positive interference (and a diffracted ray) results from the interaction of incident rays with the sample. The wavelength of electromagnetic radiation is relatedto the diffraction angle and lattice spacing in a crystalline sample by this law. The observed, processed, and counted diffracted X-rays are then analyzed.

Due to the random orientation of the powdered material, scanning the sample across a range of 2 angles should yield all possible diffraction directions of the lattice. Since each mineral has its own collection of d-spacings, converting the diffraction peaks to d- spacings allows the mineral to be identified. This is usually accomplished by comparing d-spacings to normal reference patterns [39].

The generation of X-rays in an X-ray tube is the basis of all diffraction methods. The diffracted rays are obtained after these X-rays are guided at the sample. Fig.3.2 shows a typical ZnO nano-particles XRD spectrum. The angle between the incident and diffracted rays is a significant factor in all diffraction [39]. Beyond that, the instrumentation for powder and single crystal diffraction varies.

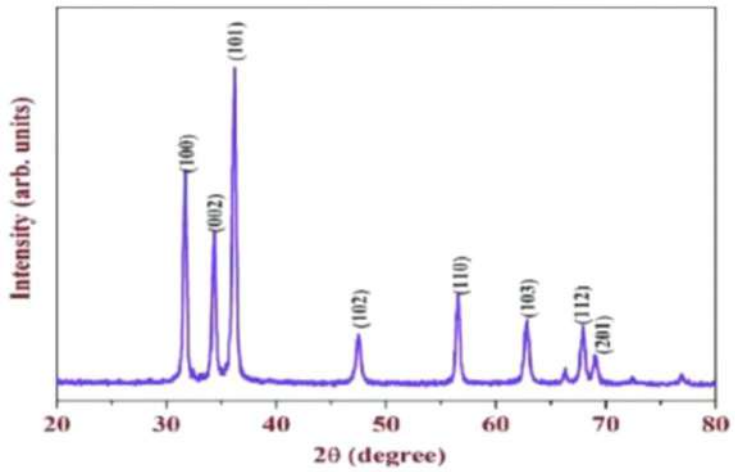

Fig. 3.2 Typical ZnO nano-particles XRD spectrum [18].

3.5 Working principle of X-ray Diffraction (XRD) machine

X-ray diffractometers consist of three basic elements: An X-ray tube, a sample holder, and an X-ray detector. X-rays are generated in a cathode ray tube by heating a filament to produce electrons, accelerating the electrons toward a target by applying a voltage, and bombarding the target material with electrons. When electrons have sufficient energy to dislodge inner shell electrons of the target material, characteristic X-ray spectra are produced [39]. These spectra consist of several components, the most common being

K_α and K_β. K_α consists, in part, of $K_{\alpha 1}$ and $K_{\alpha 2}$. $K_{\alpha 1}$ has a slightly shorter wavelength and twice the intensity as $K_{\alpha 2}$. The specific wavelengths are characteristic of the target material (Cu, Fe, Mo, Cr). Filtering, by foils or crystal monochromators, is required to produce monochromatic X-rays needed for diffraction. $K_{\alpha 1}$ and $K_{\alpha 2}$ are sufficiently closein wavelength such that a weighted average of the two is used. Copper is the most common target material for single-crystal diffraction, with CuK_α radiation = 1.5418 $\AA$. These X-rays are collimated and directed onto the sample. As the sample and detector arerotated, the intensity of the reflected X-rays is recorded. When the geometry of the incident X-rays impinging the sample satisfies the Bragg Equation, constructive interference occurs and a peak in intensity occurs. A detector records and processes this X-ray signal and converts the signal to a count rate which is then output to a device suchas a printer or computer monitor.[39]

An X-ray diffraction machine is shown in Fig.3.3. An X-ray diffractometer's geometry is such that the sample rotates at an angle θ in the direction of the collimated X-ray beam, while the X-ray detector is placed on an arm that rotates at an angle of 2θ to absorb the diffracted X-rays. A goniometer is an instrument that is used to maintain the angle and rotate the sample.

Fig. 3.3 An X-ray diffraction machine in practice.

3.6 Advantage of XRD

The advantage of XRD are summarized below

- X-ray is the cheapest, the most convenient and widely used method.
- X-rays are not absorbed very much by air, so the specimen need not be in an evacuated chamber.
- Powerful and rapid (< 20 min) technique for identification of an unknown mineral.
- In most cases, it provides an unambiguous mineral determination.
- Minimal sample preparation is required.
- XRD units are widely available.
- Data interpretation is relatively straight forward.

3.7 Limitation of XRD

XRD technique has the following limitation:

- If the crystal sample is not isometric, measuring unit cells can be difficult.
- Peak overlay will happen, and it gets worse for high-angle reflections.
- Lighter elements do not have a good interaction with them.
- The sample should be homogeneous in order to better distinguish an unknown powder content.
- XRD analysis usually necessitates the use of standard reference data.
- It is limited in scale. XRD readings often miss small structures that are only present in trace quantities, resulting in distorted findings.

3.8 XRD Technique Application

- To identify the formation of a particular material system.
- To study unit cell structure, lattice parameters and miller indices.
- Identify the type of phases present in the material.
- Estimation of crystalline and amorphous content present in the sample.
- To determine the average crystallite size, strain, or micro-strain effects in bulk materials and thin-film.
- To study the structural and thermal distortion.

CHAPTER 4
EXPERIMENTAL AND METHODOLOGY

4.1 Introduction

Doctor blade (or tape casting) is one of the widely used techniques for producing thin films on large area surfaces. The doctor blading can operate at speed up to several metersper minute and it is suitable to coat substrate with a very wide range of wet film thicknesses ranging from 20 to several hundred microns [37].

Well mixed slurry containing a suspension of ceramic particles as well as other additives (such as binders, dispersants, or plasticizers) is mounted on a substrate beyond the doctor blade in the doctor blading method .The slurry spreads on the substrate to form a thin film, which dries to form a gel-layer when a constant relative movement is formed between the blade and the substrate.

4.2 Experimental investigation

4.2.1 Film preparation

TiO_2 and ZnO NPs were purchased from Aldrich and usedwithout further purification. A schematic diagram of the molecular structure of TiO_2 is shown in Fig. 1. TiO_2 doped ZnO photoanodes were prepared by the blade coating method. The blade coating paste was prepared using 0.35 g of ZnO NPs (<100 nm), 2ml of ethanol (99.5%), and TiO_2 at various percentages (0, 0.3, 0.7, 1, and 2) as a dopant material. The mixture was dispersed vigorously using a homogenizer (Sonic VCX-130) at 60% amplitude and 1 :3 pulse rate for 30 min. Before coating, all the indium–tinoxide coated poly(ethylene naphthalate) (ITO-PEN) substrates (~ 15Ω=square) were sequentially cleaned in an ultrasonic bath using acetone (twice) and methanol (once). The substrates were then dried in nitrogen gas flow and subsequently treated in a UV–ozone chamber (Filgen, Japan) for 20 min. The paste thus prepared was coated onto the substrates using polyimide tape as the frame and spacer. We coated the layer four times to obtain a thick, adherent layer photoanode. All the samples were air-dried at room temperature for 1 h. The target thickness of the film was in the range from 9 to 12 μm.After coating, the

films were dried at 100 °C using a hot plate for 10 min and compressed using a mechanical compression machine (Mini TEST Press-10) at 130 MPa compression with 60 °C heating for 1 min [40].

4.2.2 Film Preparation and Characterization

In this experiment, the film were prepared using the doctor blade technique where the ZnO used. Our supervisor, Dr. Md. Shamimul Haque Choudhury, conducted XRD during his Master's program in Japan using an XRD system (Rigaku RINT 2100 diffractometer) equipped.

Modified Williamson-Hall (W–H) models, Size-Strain Plot (SSP), Halder-Wagner (H–W) method, and Wagner-Agua Method were all used to characterize the XRD properties.

4.3 Methodology

4.3.1 Williamson-Hall method (1953)

4.3.1.1 Introduction

The Williamson-Hall system, which was discovered in 1953, has been used for the past five tenner. The plots caused by strain were peaked by W-H plots. The peak width obtained from crystallite dimension varies from $1/\cos\theta$, as the strain varies from $\tan\theta$. This distinction in conduct as a purpose of 2θ allows us to comparison between the effects of strain and size on peak expansion. When the width of peaks as a function of 2θ was studied by Williamson-Hall, deconvoluted sizes and strain-induced expansion were used to simplify integral breadth approaches [44].

There are three modified W-H models [52]. They are:

- Uniform deformation model (UDM)
- Uniform Stress Deformation Model (USDM)
- Uniform Deformation Energy Density Model (UDEDM)

4.3.1.2 Uniform deformation model (UDM)

The line broadening because of the finite dimension of the rational scattering area and

the inner tension in the arranged film are also taken into account in the Williamson–Hall approach. The diffraction line broadening, as per Williamson and Hall, is reasoned by crystallite size and strain contribution.But, by considering the peak width as a purpose of 2 [45], the XPPA by W–H methods is a easier approach that specifically determines between size-induced and strain-induced peak broadening. The formula was familiar wirh evaluate the strain-induced broadening in powders because of crystal flaw and deformation,

$$\varepsilon = \beta_{hkl}/(4\tan\theta) \tag{4.13}$$

From eqs. (4.7) and (4.11), the peak width from crystallite size varies as 1/Cos and strain varies as tanθ according to the findings. The sum of the contributions of crystallite size and strain in the material now represents the complete peak broadening, which can be written as [45],

$$\beta_{hkl} = \beta_D + \beta_\varepsilon \tag{4.14}$$

where $\mathscr{B}$D denotes crystallite size contribution, $\mathscr{B}\varepsilon$ denotes strain-induced broadening, and $\mathscr{B}$hkl denotes the width of the half-maximum amplitude of instrumental corrected broadening. Eq. (4.6) is used to measure the instrumental corrected broadening of each diffraction peak. The observed line breadth is the sum of Eqs. (4.7) and (4.11) and given as [45] if the particle size and strain contributions to line broadening are independent of each other and both have a Cauchy-like profile.

$$\beta_{hkl} = \frac{K\lambda}{D.\cos\theta} + 4.\varepsilon.\tan\theta \tag{4.15}$$

By rearranging Eq. (4.15), we get

$$\beta_{hkl} = \frac{K\lambda}{D\cos\theta} + 4.\varepsilon.\tan\theta \tag{4.16}$$

The uniform deformation model (UDM) is described by Eq. (4.16), which is Williamson–Hall equation. Equation (4.16) is known as the uniform deformation model since it assumes uniform strain in all crystallographic directions (UDM). The

crystal in this model is assumed to be isotropic in nature, and the properties of the material are assumed to be independent of the measurement direction. The crystalline size D was calculated from the y-intercept, and the micro-strain e was estimated from the slope of the linear fit, based on the values of $\mathscr{B}$hkl cosθhkl on the y-axis as a function of 4. sinθhkl on the x-axis **(Fig. 4.2). Fig. 4.2** depicts the UDM for ZnO nanoparticles. This strain may be caused by the lattice shrinkage that was observed during the lattice parameter measurement.

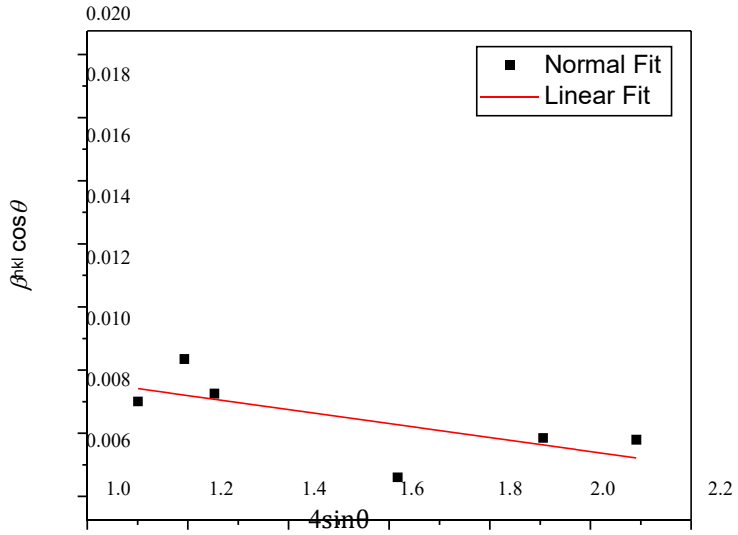

Fig. 4.1 Plot of $\beta_{hkl} \cos \theta_{hkl}$ versus 4 $\sin\theta_{hkl}$

4.3.1.3 Uniform stress deformation model (USDM)

The homogeneity and isotropy assumptions are often violated. An anisotropic solution was used to introduce a more practical scenario. An an-isotropic strain modifies the Williamson–Hall equation, as a result. The lattice deformation stress is believed to be constant in all crystallographic directions in the uniform stress deformation model (USDM), and the particles are assumed to have a minimal microstrain. The strain is referred to by Hooke's law in USDM, and there is a linear proportionality betweenstress and strain as determined by Hooke's law.

$$\sigma = \varepsilon Y_{hkl} \text{ or } \varepsilon = \sigma / Y_{hkl}, \tag{4.17}$$

where σ is the stress of the crystal, ε is anisotropic microstrain, this will depend on the crystallographic directions and Y_{hkl} is the modulus of elasticity or Young‘s modulus. This equation is only a rough approximation, and it is only true for a very small strain; as strain increases, the particles deviate from the linear proportionality. The Williamson–Hall equation is modified in this method by substituting the value of ε in Eq (4.16), we get

$$\beta_{hkl} \cos \theta_{hkl} = \frac{K\lambda}{D} + 4.\sigma. \tag{4.18}$$

For a hexagonal crystal, Young‘s modulus is given by the following relation,

$$Y_{hkl} = \frac{\left[h^2 + \frac{(h+2k)^2}{3} + \left(\frac{al}{c}\right)^2\right]^2}{s_{11}\left(h^2 + \frac{(h+2k)^2}{3}\right)^2 + ss_{33}\left(\frac{al}{c}\right)^4 + (2s_{13}+s_{44})\left(h^2 + \frac{\left(h+2k\right)^2}{3}\left(\frac{al}{c}\right)^2\right.} \tag{4.19}$$

Where _a‘ and _c‘ are lattice parameters; s11, s13, s33 and s44 are the elastic compliances of ZnO with values 7.858x10-12, -2.206x10-12, 6.940x10-12 and 23.57x10-12 m2 N-1, respectively [46]. Young‘s modulus, Y_{hkl}, for hexagonal ZnO nanoparticles was calculated as ~127 GPa.

The uniform deformation stress can be calculated from the slope of the linear fit, andthe y-intercept gives the crystallite size, when plotting $\mathscr{B}$hkl cosθhkl as a function of 4sinθ/Y_{hkl} **(Fig. 4.3)**. If the Young's modulus, Y_{hkl}, of hexagonal ZnO nano-particlesis determined, the strain ε can be measured

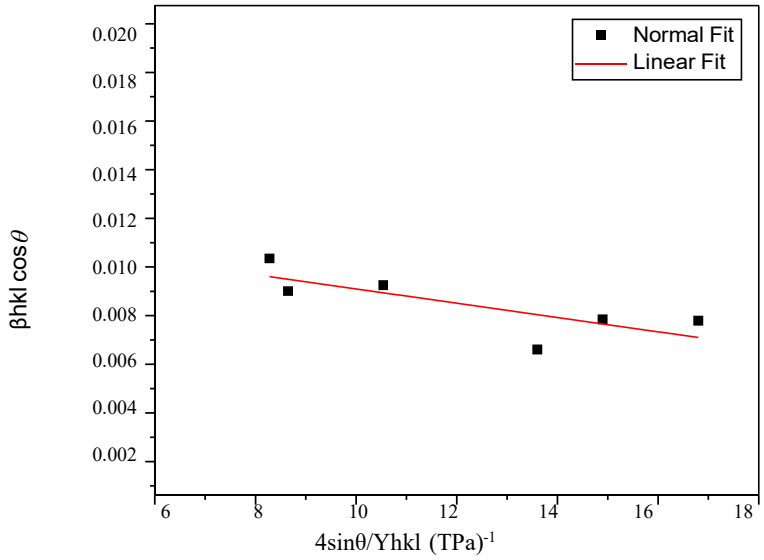

Fig. 4.2 Plot of $\beta_{hkl}\cos\theta_{hkl}$ versus $4\sin\theta/Y_{hkl}$

4.3.1.4 Uniform deformation energy density model (UDEDM)

The USDM model assumes a linear relationship between stress and strain, according to Hook's law, while the UDM model assumes the crystal is isotropic. However, since different defects, dislocations, and agglomerates cause imperfections in almost all crystals, the isotropic nature and linear proportionality between stress and strain cannot be considered in real crystals. As a result, a new model is required to research various crystal microstructures. For this function, the Uniform deformation energy density model (UDEDM) is used, which takes into account uniform anisotropic lattice strain in all crystallographic directions, with the density of deformation energy as the cause of that uniform anisotropic lattice strain [47].

Energy density (u), according to Hooke's law, is proportional to strain.

$$\mu_{ed} = (\varepsilon^2 Y_{hkl})/2 \; or \; \varepsilon = \sqrt{\frac{2\mu_{ed}}{Y_{hkl}}} \tag{4.20}$$

Where Y_{hkl} is the anisotropic Young‘s modulus.

Then, Eq. (4.18) can be rewritten according to the energy and strain relation as

$$\beta_{hkl}\cos\theta_{hkl} = \left(\frac{K\lambda}{D}\right) + \left(4\sin\theta_{hkl}\left(\frac{2\mu_{ed}}{Y_{hkl}}\right)^{1/2}\right) \tag{4.21}$$

$$\beta_{hkl}\cos\theta_{\text{hkl}} = \left(\frac{K\lambda}{D}\right) + \left(4\sin\theta_{hkl}\left(\frac{2\mu_{ed}}{Y_{hkl}}\right)^{1/2}\right) \quad (4.21)$$

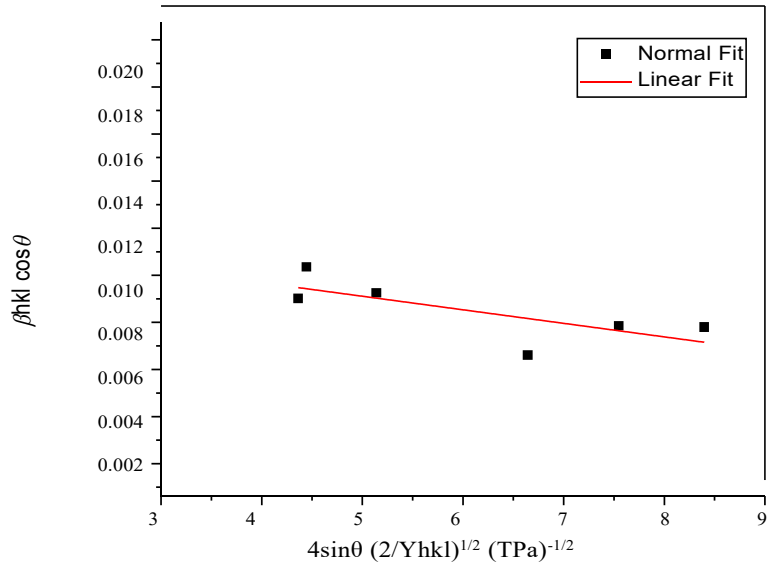

Fig. 4.3 Plot of $\beta_{hkl}\cos\theta_{\text{hkl}}$ versus $4\sin\theta\ (2/Y\text{hkl})^{1/2}$

4.3.2 Size–strain plot (SSP)

The Williamson-Hall method takes into account peak broadening as a function of diffraction angle (2), which is thought to be a combination of size and strain induced broadening. There are, however, models that deal with the analysis of peak profiles. One such method is the Size-Strain plot (SSP), which assumes that the XRD peak profile is a combination of Lorentzian and Gaussian functions, with the size broadened profile labeled as a Lorentz function and the strain broadened profile labelled as a Gaussian function [48]. As a result, the total SSP broadening can be written as

$$\beta_{hkl} = \beta_L + \beta_G$$

The peak broadening due to Lorentz and Gaussian functions, respectively, is βL and βG. Furthermore, the SSP approach often produces a better result for isotropic broadening since it prioritizes low angle reflections, which have higher accuracy and precision, over higher angle reflections. This is because XRD data is of poorer qualityat higher angles, and peaks are usually heavily overlapped at higher diffracting angles.

As a result, the SSP calculation is done using the following equation.

$$(\beta_{hkl}\cos\theta_{hkl})^2 = \frac{k}{D}(d^2{}_{hkl}\beta_{hkl}\cos\theta_{hkl}) + (\frac{E}{2})^2 \quad (4.22)$$

where d_{hkl} is the lattice distance between the <h k l> planes and for the hexagonalcrystal structure,

$$d_{hkl} = \frac{a}{\left[\sqrt{4/3(h^2 + k^{2+}hk) + \left(\frac{al}{c}\right)^2}\right]} \quad (4.23)$$

K is a constant that depends on the shape of the particles; for spherical particles it is given as ¾ and ε is a measure of the apparent strain which is related to the root mean square (RMS) strain ε_{RMS}..

$$< \varepsilon_{RMS} > = \left(\frac{\varepsilon}{2\sqrt{2\pi}}\right) \quad (4.24)$$

In **Fig. 4.4**, similarly to the W-H methods, the term $(d_{hkl}\mathscr{B}_{hkl}\cos\theta_{hkl})^2$ is plotted with respect to $(d^2_{hkl}\mathscr{B}_{hkl}\cos\theta_{hkl})$ for the all orientation peaks of ZnO-NPs with the wurtzite hexagonal phase. In this case, the particle size is determined from the slope of the linearly fitted data and the root of the y-intercept gives the strain.

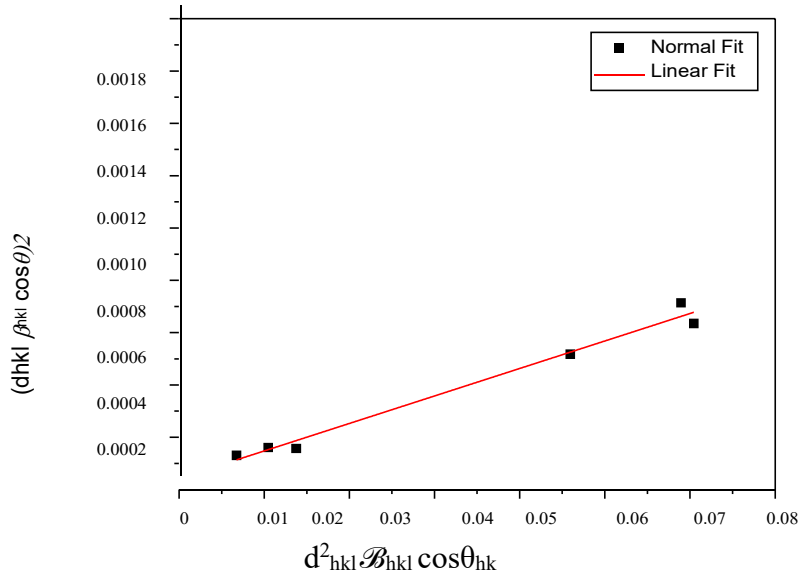

Fig. 4.4 Plot of $(d_{hkl}\mathscr{B}_{hkl}\cos\theta_{hkl})^2$ versus $(d^2_{hkl}\mathscr{B}_{hkl}\cos\theta_{hkl}$

4.3.4 Halder-Wagner Method

Size broadening of the XRD peak profile was assumed to be a Lorentzian function in the SSP system, while strain broadening was assumed to be a Gaussian function. However, the XRD peak is neither a Lorentzian nor a Gaussian function, since the XRD peak region matches well with the Gaussian function, but its tail falls off too quickly without matching, and the tails of the profile, on the other hand, match well with the Lorentz function, but do not match the XRD peak region [49]. To get around this problem, the Halder-Wagner approach is used, which is based on the assumption that peak broadening is a symmetric Voigt function [49] because it is a convolution of Lorentzian and Gaussian functions. As a result, the full width at half limit of the physical profile for the Voigt function can be written using the Halder-Wagner Method as

$$\beta_{hkl}^2 = \beta_L \cdot \beta_{hkl} + \beta_G^2 \qquad (4.25)$$

Where, β_L and β_G are the full width at half maximum of the Lorentzian and Gaussian function. This approach has the advantage of giving more weight to peaks in the low and mid angle ranges, where there is less duplication of diffracting peaks. According to the Halder-Wagner Method, the relationship between crystallite size and lattice strain is now:

$$\left(\beta_{hkl}^* / \beta_{hkl}^*\right)^2 = \frac{1}{D} \cdot \left(\beta_{hkl}^* / {d_{hkl}^*}^2\right) + \left(\frac{\varepsilon}{2}\right)^2 \qquad (4.26)$$

Where $\beta_{hkl}^* = \beta_{hkl}.\cos\theta/\lambda$ and $d^*_{hkl} = 2d_{hkl}.\sin\theta/\lambda$.

Plot of equation (4.26), with $(\beta^*_{hkl}/d^{*2}_{hkl})$ term along X-axis and $(\beta^*_{hkl}/ d^*_{hkl})^2$ along Y-axis for each peak of the XRD pattern, is shown in (**Fig. 4.6)**. The slope of the plotted straight line provides the average size, whereas the intercept gives the intrinsic strain of the ZnO nanocrystals.

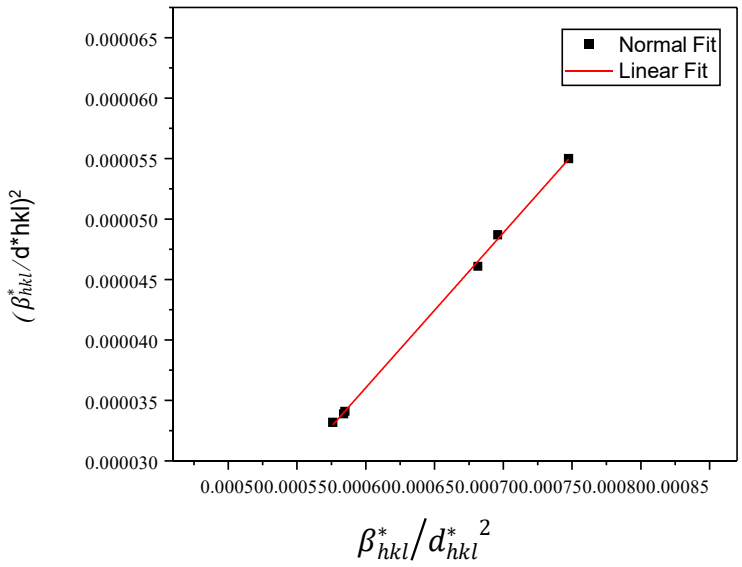

Fig. 4.5 Halder-Wagner plot for ZnO nanoparticles.

4.3.4 Wagner-Agua Method

The method proposed by Wagner and Agua to determine crystallite size and strain has also been considered. Describes the Wagner and Agua equation [50],

$$(\beta_{hkl}\cos\theta)^2 = (4\varepsilon_{WA}\sin\theta_{hkl})^2 + \left(\frac{K\lambda}{D_{WA}}\right)^2 \qquad (4.27)$$

Where and represent the Wagner-Agua crystallite size and lattice strain, respectively. The W-A plots of Zn-nanoparticles are drawn taking $(\mathscr{B}_{hkl}\cos\theta_{hkl})^2$ in the vertical and horizontal axis, respectively. In the Wagner-Agua (W- A) plots shown in (**Fig. 4.7**), We fit the experimental data with linear fits, from which the slope yields the strain (ε_WA), and the intercept on the vertical axis yields a crystallite size calculation (DWA).

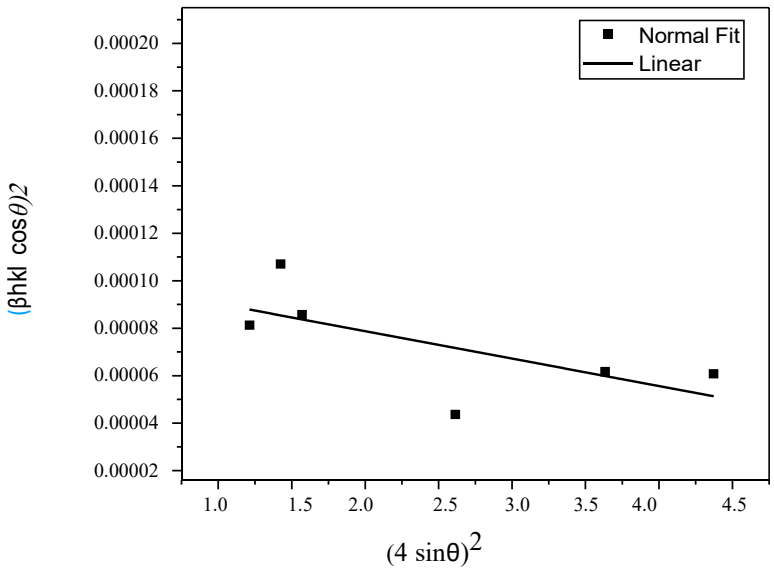

Fig. 4.6 Wagner-Agua plot for ZnO nanoparticle

4.3.6 Determination of lattice parameters

As ZnO crystallizes, the oxygen atoms are arranged in a hexagonal close packed form, with zinc atoms occupying half of the tetrahedral sites. The atoms Zn and O are tetrahedrally coordinated to each other and thus have the same position. All of the octahedral and half of the tetrahedral sites in the zinc structure are empty. Bragg's law [51] states that,

$$n\lambda = 2d \sin\theta \qquad (4.28)$$

Where n is the order of diffraction (usually n = 1), is the X-ray wavelength and d is the spacing between planes of given Miller indices h, k and l. The plane spacing d is related to the lattice constants a, c, and Miller indices in the ZnO hexagonal structure by the following relationship [51],

$$\frac{1}{d^2_{(hkl)}} = \left(\left(\tfrac{4}{3}(h^2+k^2+hk)\right)/a^2\right) + {}^{1^2}/_{c^2} \qquad (4.29)$$

With the first-order approximation, n = 1;

$$sin^2\theta = \frac{\lambda^2}{4a^2}\left[\tfrac{4}{3}(h^2+k^2+hk) + \left(\frac{a}{c}\right)^2 l^2\right] \qquad (4.30)$$

The lattice constant a for <100> plane is calculated by [51]

$$a = \frac{\lambda}{\sqrt{3}\sin\theta_{(100)}} \tag{4.31}$$

For the <002> plane, the lattice constant c is calculated by [51],

$$c = \frac{\lambda}{\sin\theta\theta_{(002)}} \tag{4.32}$$

The unit cell volume V is obtained from the following equation [52]

$$V = \frac{\sqrt{3}a^2c}{2} \tag{4.33}$$

CHAPTERR 5

RESULT AND DISCUSSIONS

5.1 Introduction

In this chapter, We have determined and compared different structural parameters of P25 type Titanium dioxide doped ZnO nanoparticles. The parameters are crystallite size (D), strain (ε), stress (σ) and energy density (u). The method used to determine the parameters are modified W-H models i.e. Uniform deformation model (UDM), Uniform stress deformation model (USDM), Uniform deformation energy density model (UDEDM), size-strain plot (SSP), Halder-Wagner method and Wagnner agua method.

5.2 XRD analysis of ZnO nanoparticles without doping

The XRD patterns of the prepared samples of ZnO nanoparticles without doping were shown in **Fig. 5.1** which is determined by placing the value of 2θ along x-axis and intensity along y-axis. All the diffraction peaks could be well indexed as the ZnO wurtzite structure found in the standard reference data.

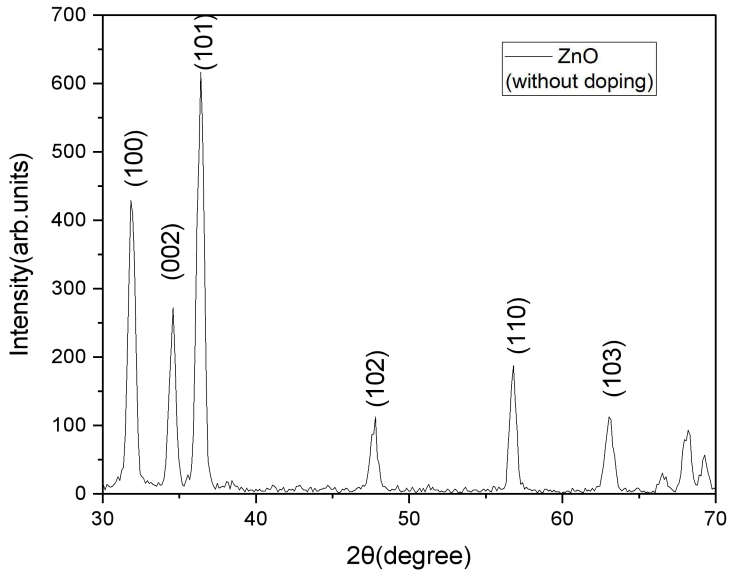

Fig. 5.1 XRD pattern of ZnO nanoparticles without doping

Analysis of first peak (100)

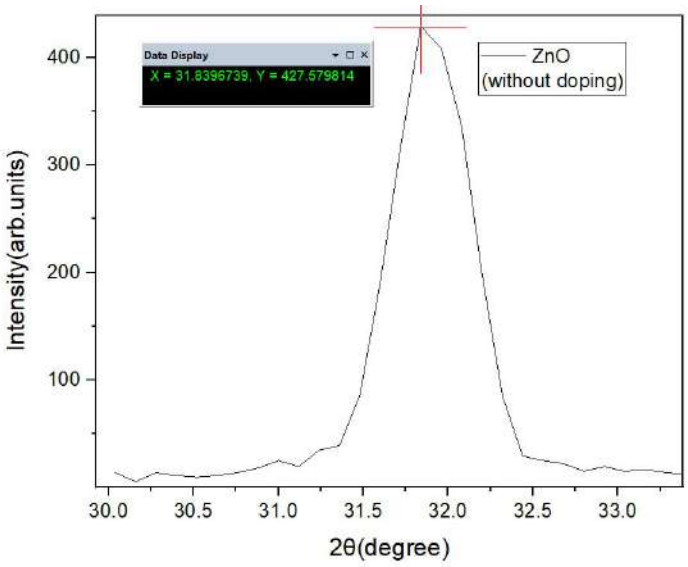

Fig. 5.2 Measurement of θ of peak

(a)

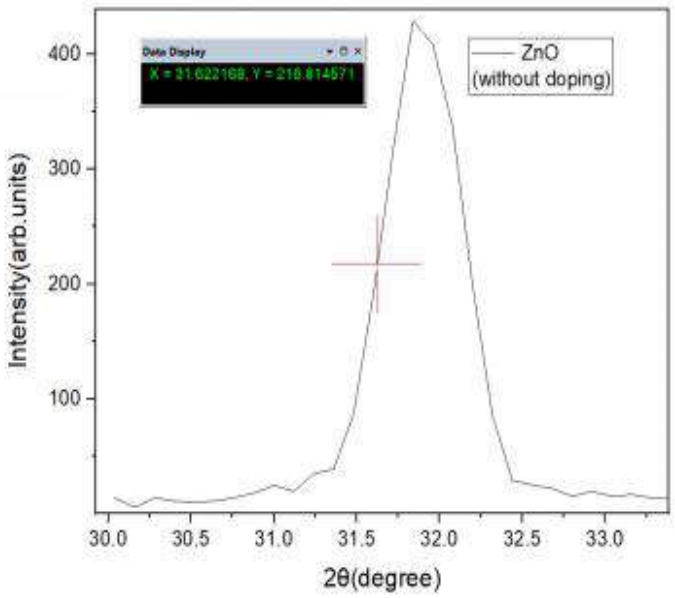

(b)

Fig. 5.3 Measurement of βhkl of peak (100): (a) Value of 2θ at right of the broadening at half maximum and (b) Value of 2θ at left of the broadening at half maximum.

For (100) peak, the line broadening at full width half maximum (FWHM):

βhkl = (32.1879986-31.622168)

=0. 5658306

In radian,

Bhkl = 0.5658306×(π/180)

= 0.00987560697

Analysis of 2nd peak (002)

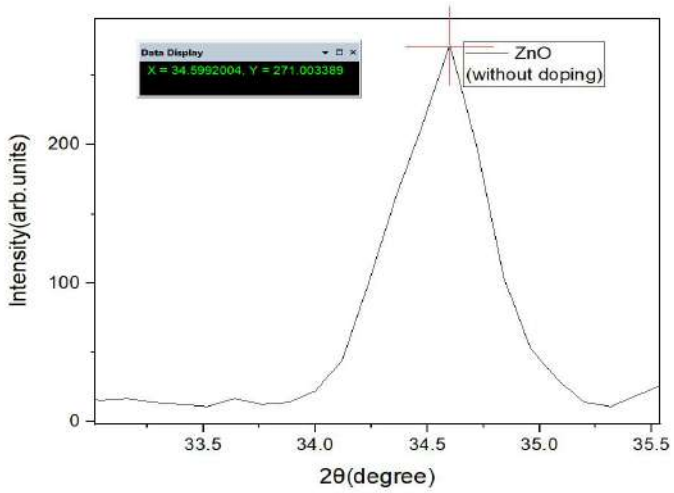

Here,
2θ=34.5992
θ=17.2996

Fig. 5.4 Measurement of θ of peak (002)

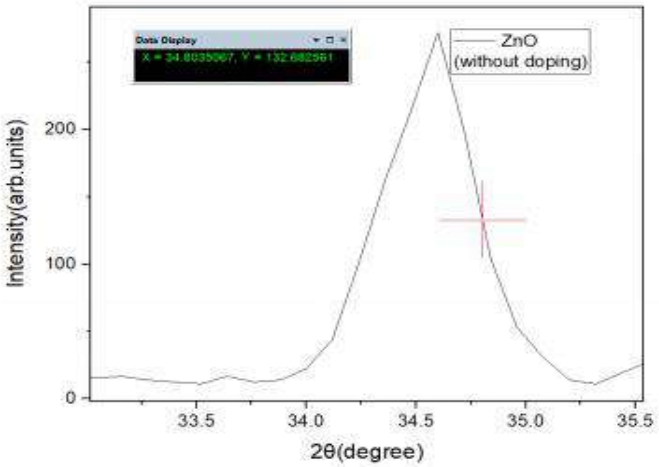

(a)

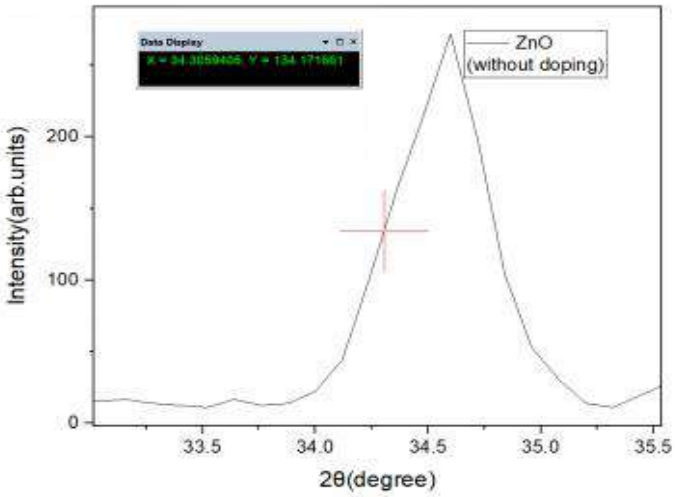

(b)

Fig. 5.5 Measurement of βhkl of peak (002): (a) Value of 2θat right of the broadening at half maximum and (b) Value of 2θ at left of the broadening at half maximum.

For (002) peak, the line broadening at full width half maximum (FWHM):

βhkl = (34.8035067-34.3059405)

= 0.4975662

In radian,

βhkl = 0.4975662×(π/180)

= 0.00868416843

Analysis of third peak (101)

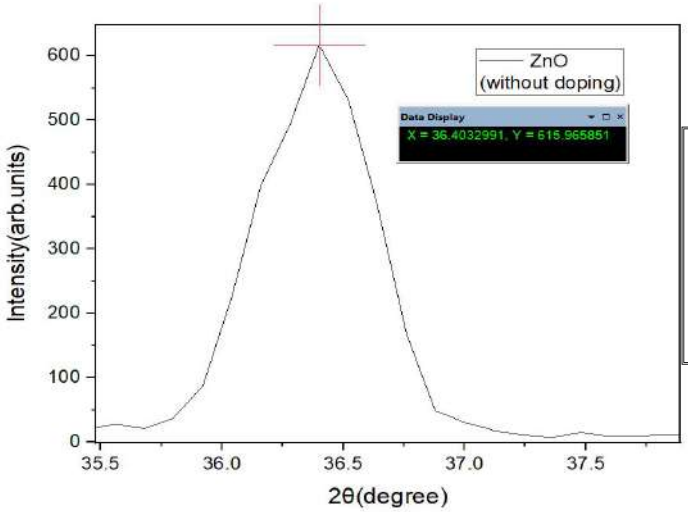

Here,
2θ=36.4032
θ =18.2016

Fig. 5.6 Measurement of θ of peak (101)

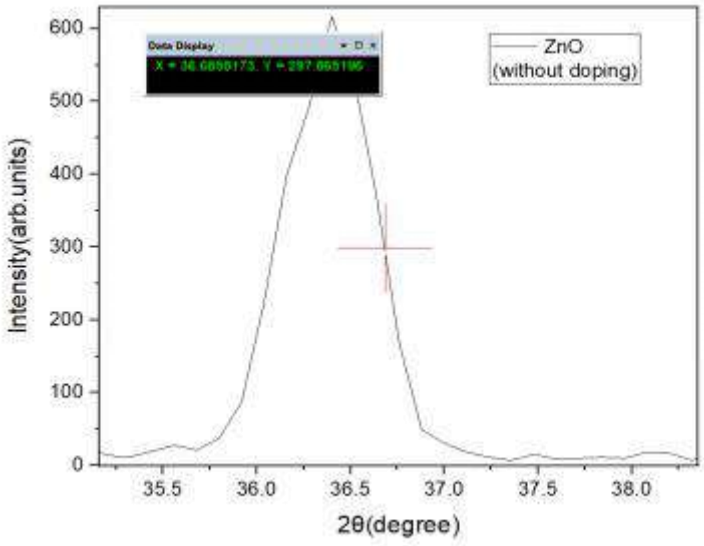

(a)

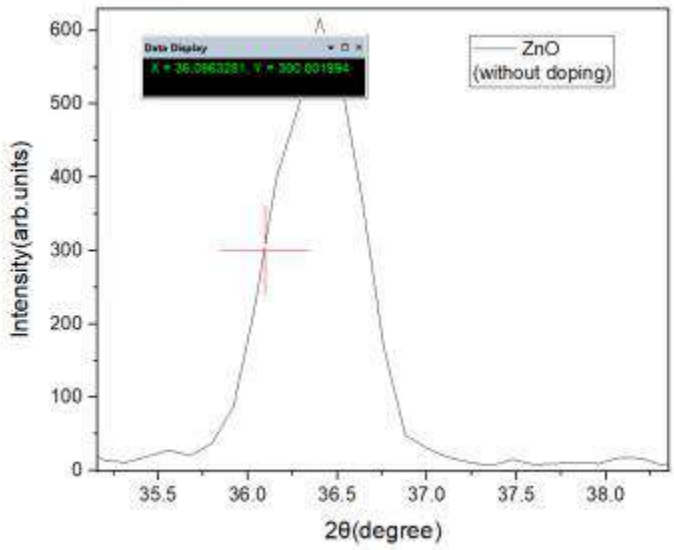

(b)

Fig. 5.7 Measurement of βhkl of peak (101): (a) Value of 2θ at right of the broadening at half maximum and (b) Value of 2θ at left of the broadening at half maximum.

For (101) peak, the line broadening at full width half maximum (FWHM):

βhkl = (36.77647-35.84386)

= 0.93261

In radian,

βhkl = 0.93261×(π/180)

= 0.01627712

Analysis of fourth peak (102)

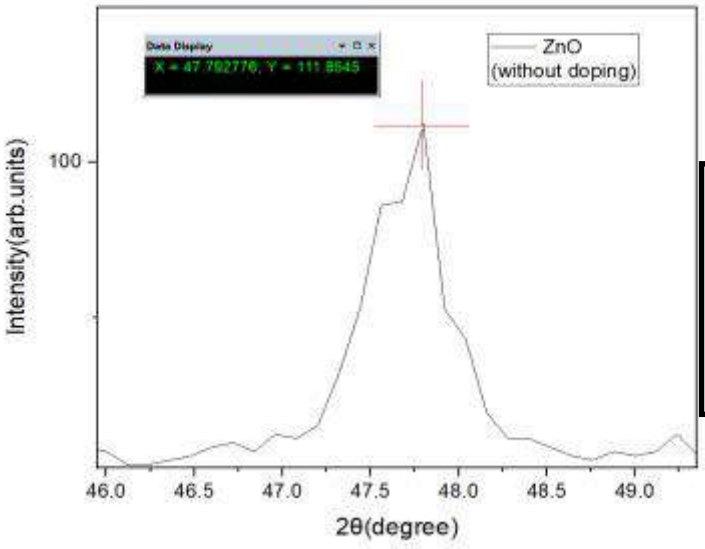

Here,
2θ=47.7927
θ= 23.8963

Fig. 5.8 Measurement of θ of peak (102)

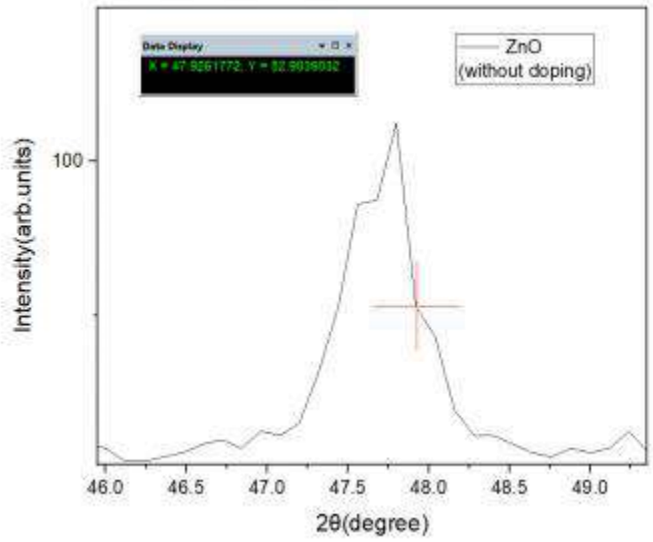

(a)

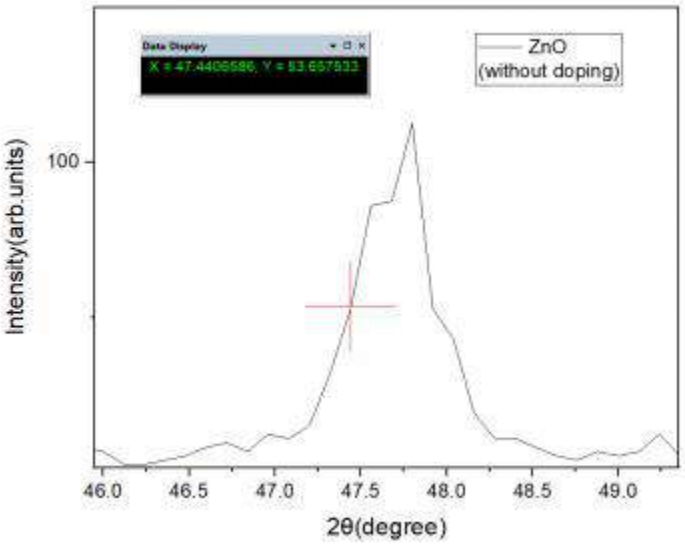

(b)

Fig. 5.9 Measurement of βhklof peak (102): (a) Value of 2θ at right of the broadening at half maximum and (b) Value of 2θ at left of the broadening at half maximum.

For (102) peak, the line broadening at full width half maximum (FWHM):

βhkl = (47.9261772-47.4406586)

= 0.4855186

In radian,

βhkl = 0.4855186×(π/180)

= 0.0084738981

Analysis of fifth peak (110)

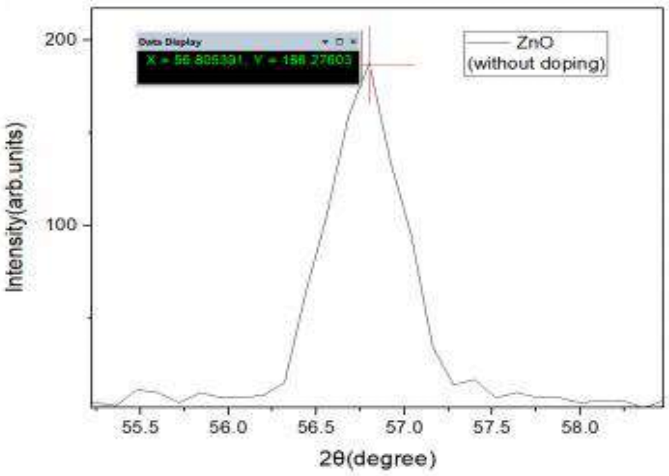

Here,
2θ=56.8053
θ=28.4027

Fig. 5.10 Measurement of θ of peak (110)

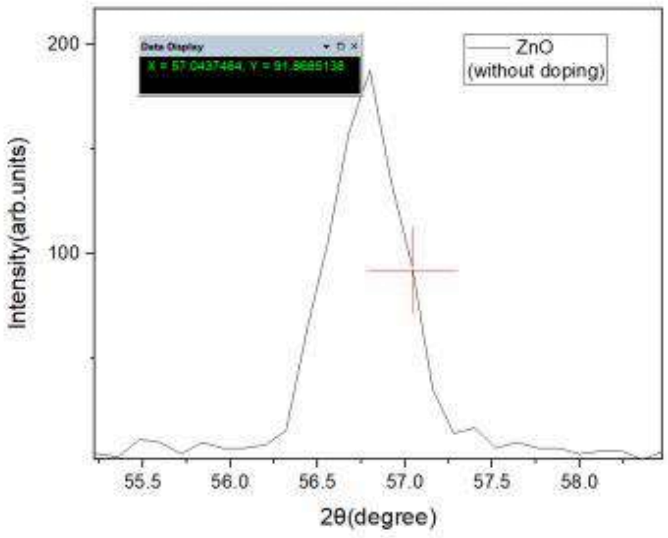

(a)

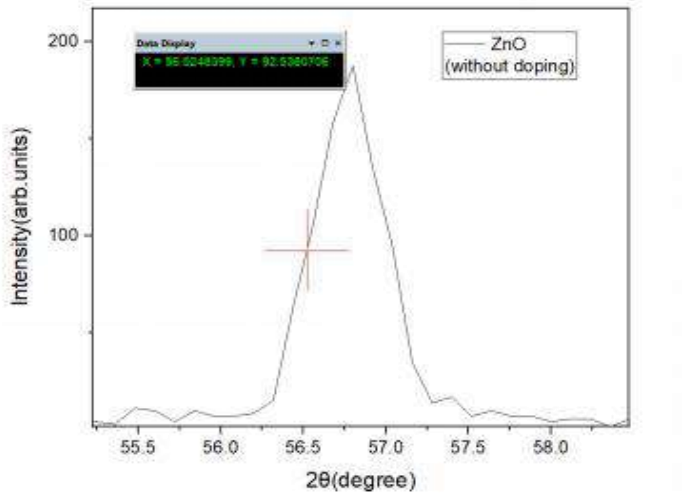

(b)

Fig. 5.11 Measurement of βhkl of peak (110): (a) Value of 2θ at right of the broadening at half maximum and (b) Value of 2θ at left of the broadening at half maximum.

For (110) peak, the line broadening at full width half maximum (FWHM):

Bhkl = (56.93185-56.38744)

= 0.54441

In radian,

Bhkl = 0.45853×(π/180)

= 0.00950175

Analysis of sixth peak (103)

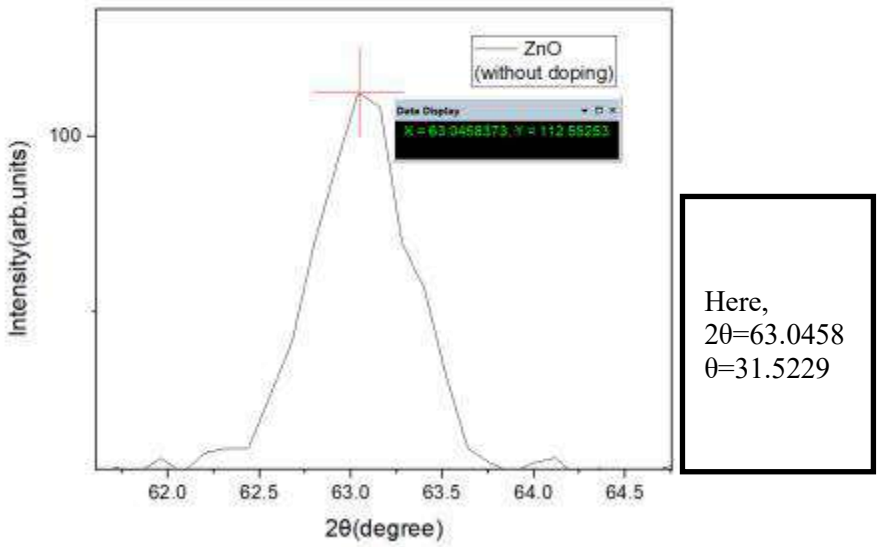

Fig. 5.12 Measurement of θ of peak (103)

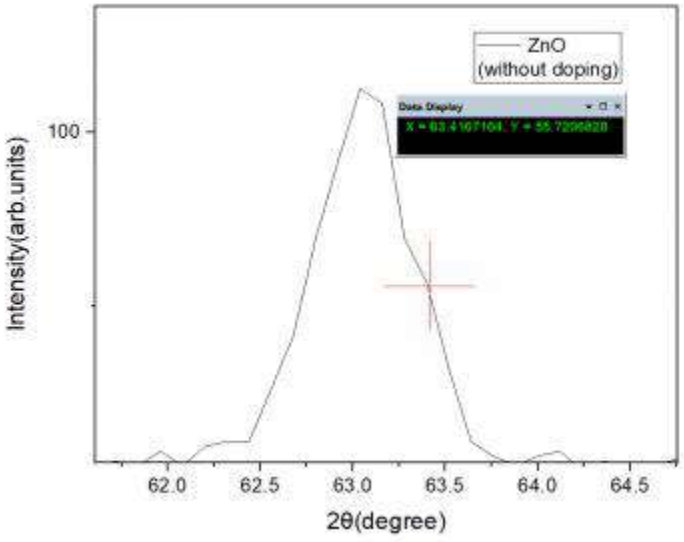

(a)

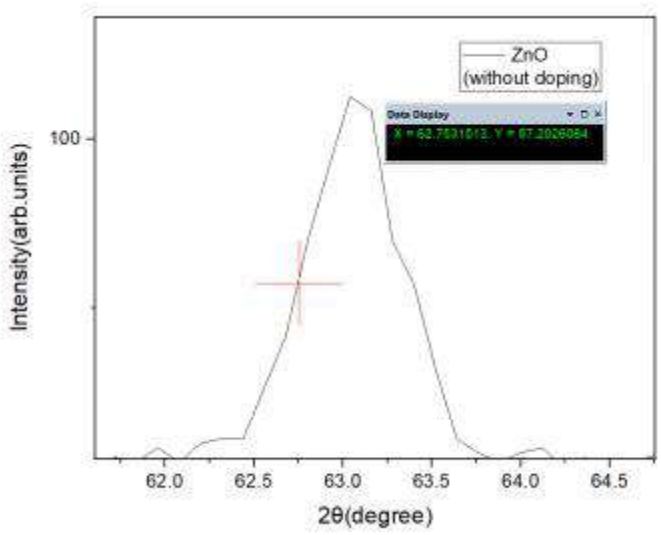

(b)

Fig. 5.13 Measurement of βhkl of peak (103): (a) Value of 2θ at right of the broadening at half maximum and (b) Value of 2θ at left of the broadening at half maximum.

For (103) peak, the line broadening at full width half maximum (FWHM):

βhkl = (63.0458373-62.7531513)

= 0.6635651

In radian,

βhkl = 0.6635651×(π/180)

= 0.0115813958

Fig. 5.2, Fig. 5.3, Fig. 5.4, Fig. 5.5, Fig. 5.6, Fig. 5.7, Fig. 5.8, Fig. 5.9, Fig. 5.10, Fig. 5.11, Fig. 5.12 and Fig. 5.13 shows analysis of the first six peaks. Bragg's angle (θ) and the line broadening at full width half maximum (FWHM) is obtained from these figures.

5.3 XRD analysis of 0.3% P25: ZnO tetraphenylporphyrin doped ZnO nanoparticles

The XRD patterns of the prepared samples of ZnO nanoparticles with 0.3% P25 doping were shown in **Fig. 5.14** Which is determined by placing the value of 2θ along x-axis and intensity along y-axis. All the diffraction peaks could be well indexed as the ZnO wurtzite structure found in the standard reference data.

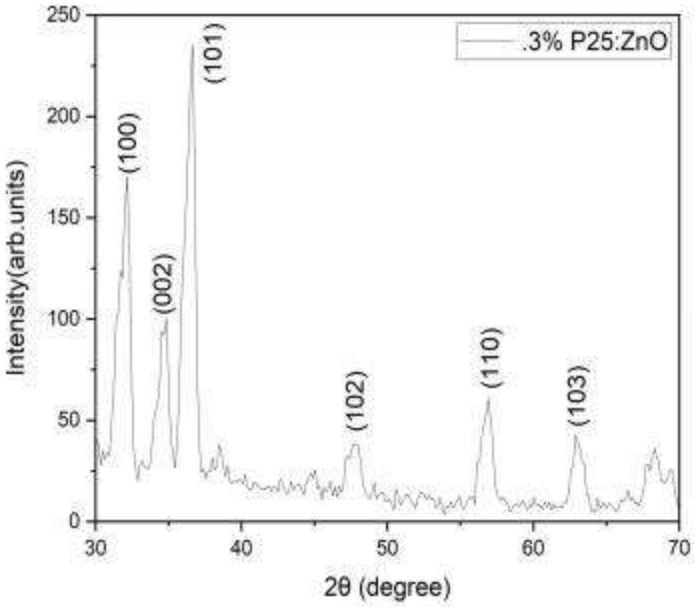

Fig. 5.14 XRD pattern of 0.3 % P25:ZnO doped ZnO nanoparticles

Analysis of the first six peaks are shown in **Fig. 5.15, Fig. 5.16, Fig. 5.17, Fig. 5.18, Fig. 5.19, Fig. 5.20, Fig. 5.21, Fig. 5.22, Fig. 5.23, Fig. 5.24, Fig. 5.25 and Fig. 5.26.** Bragg's angle (θ) and the line broadening at full width half maximum (FWHM) is obtained from these figures.

Analysis of first peak (100)

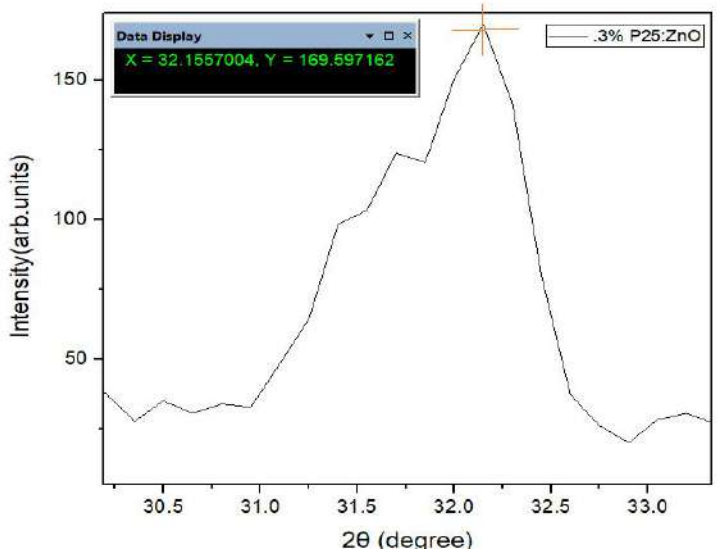

Here,
2θ=32.155700
θ=16.0778502

Fig. 5.15 Measurement of θ of peak (100)

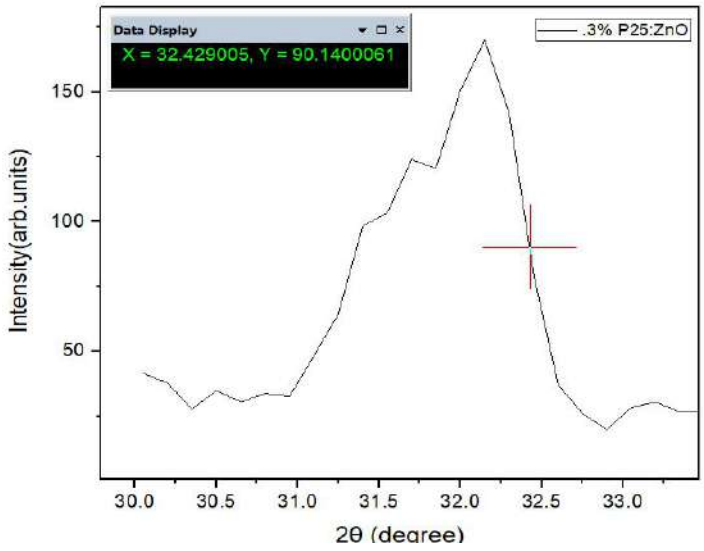

(a)

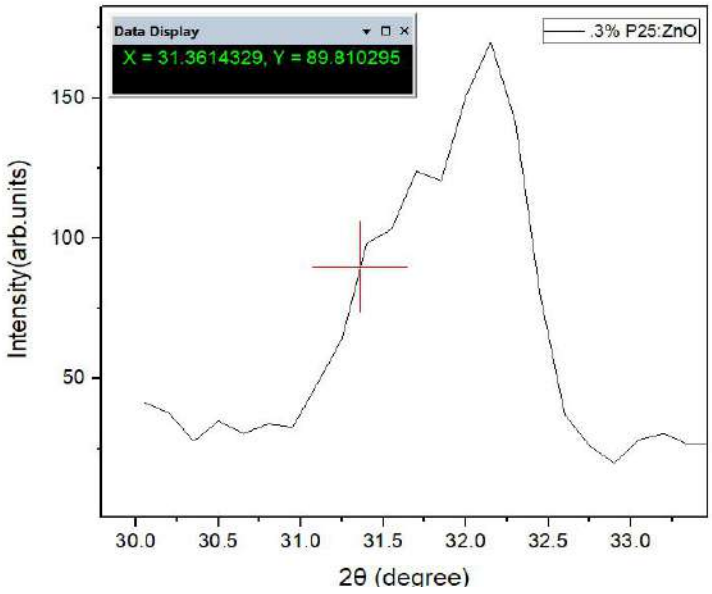

(b)

Fig. 5.16 Measurement of βhk lof peak (100): (a) Value of 2θ at right of the broadening at half maximum and (b) Value of 2θ at left of the broadening at half maximum.

For (100) peak, the line broadening at full width half maximum (FWHM):

Bhkl = (32.1557004-31.3614329)

= 1.0675721

In radian,

Bhkl = 1.067572×(π/180)

= 0.0186326481

Analysis of second peak (002)

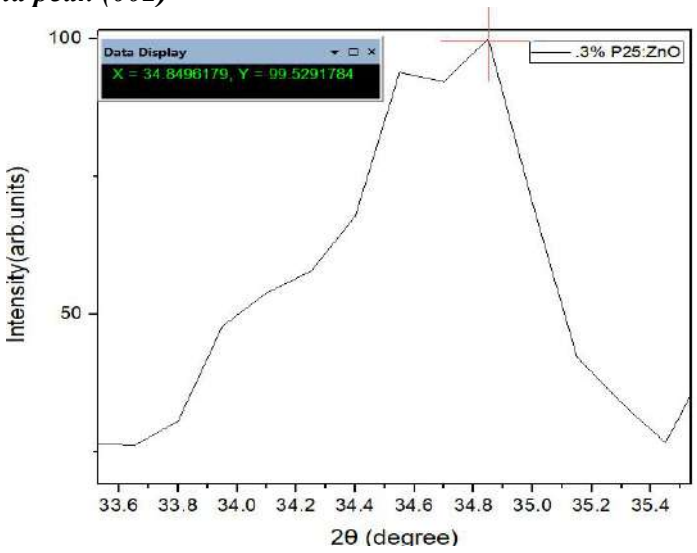

Here,
2θ=34.8496
θ=17.4248

Fig. 5.17 Measurement of θ of peak (002)

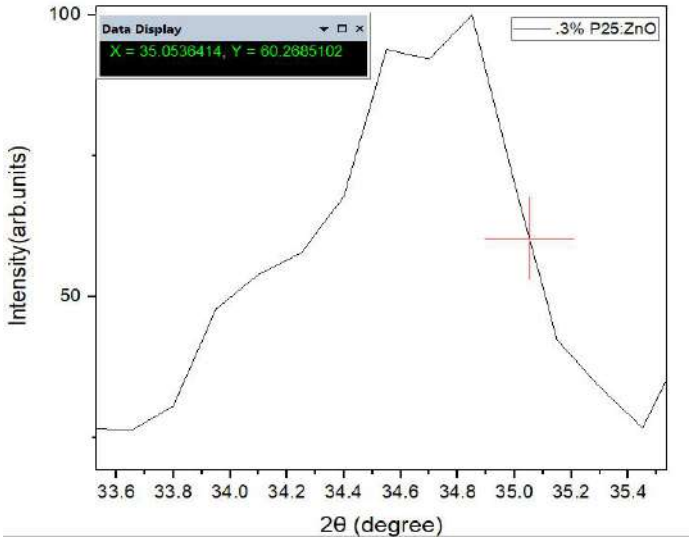

(a)

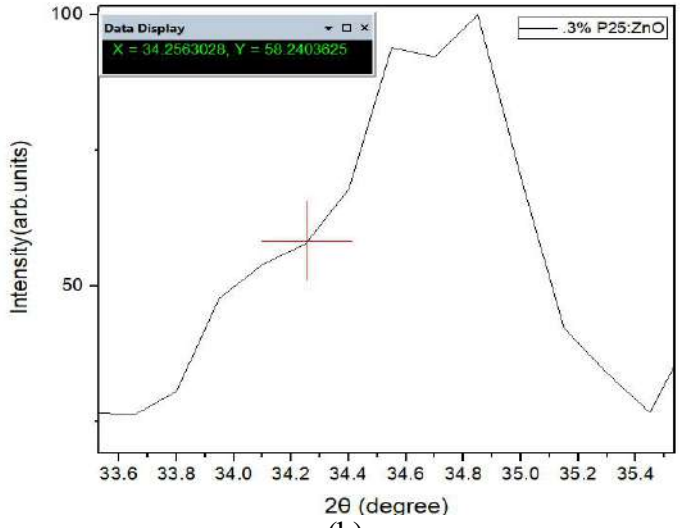

(b)

Fig. 5.18 Measurement of βhkl of peak (002): (a) Value of 2θ at right of the broadening at half maximum and (b) Value of 2θ at left of the broadening at half maximum.

For (002) peak, the line broadening at full width half maximum (FWHM):
βhkl = (35.0536414-34.2563028)
= 0.7973386

In radian,
βhkl = 0.7973386× (π/180)
= 0.0139161838

analysis of third peak (101)

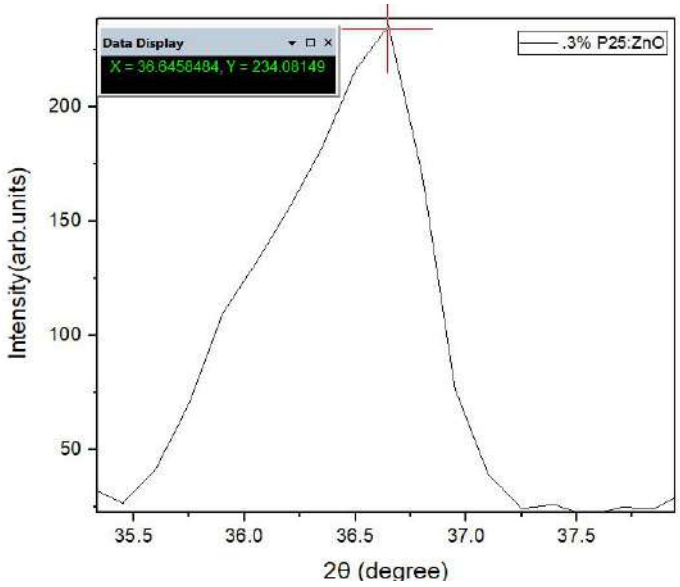

Here,
2θ=
36.6458
θ=18.3229

Fig. 5.19 Measurement of θ of peak (101)

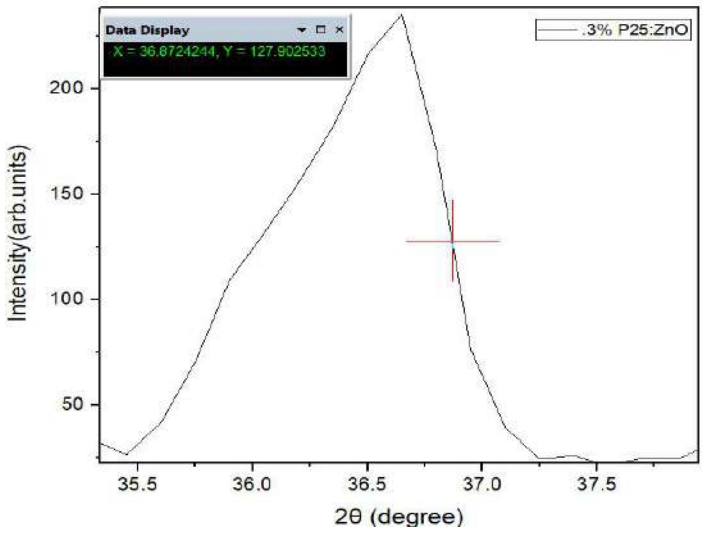

(a)

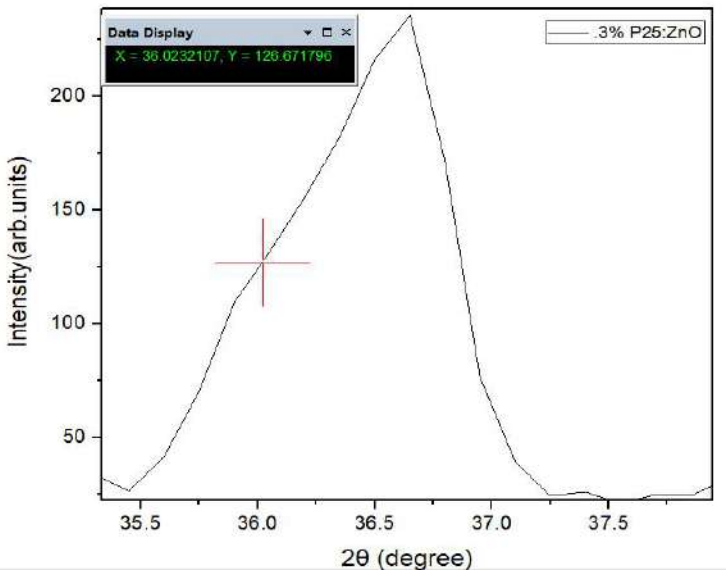

(b)

Fig. 5.20 Measurement of β_{hkl} of peak (101): (a) Value of 2θ at right of the broadening at half maximum and (b) Value of 2θ at left of the broadening at half maximum.

For (101) peak, the line broadening at full width half maximum (FWHM):

B_{hkl} = (36.8724244-36.0232107)
= 0.8492137

In radian,

β_{hkl} = 0.8492137×(π/180)
= 0.01482157

Analysis of fourth peak (102)

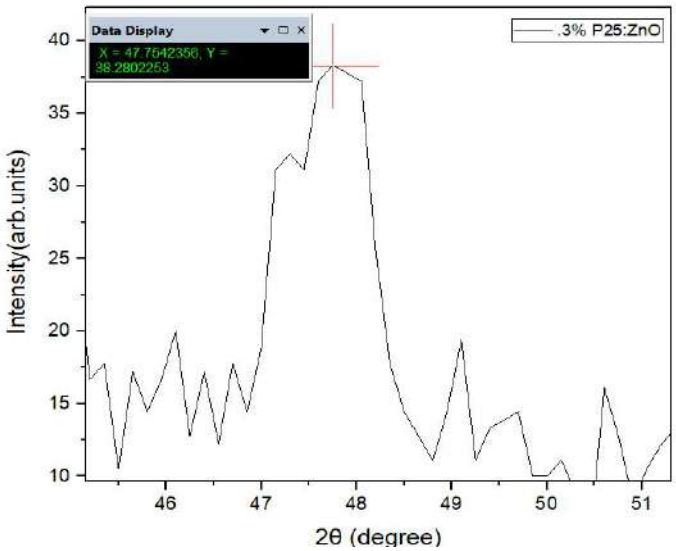

Here,
2θ= 47.754236
θ=23.87711 78

Fig. 5.21 Measurement of θ of peak (102)

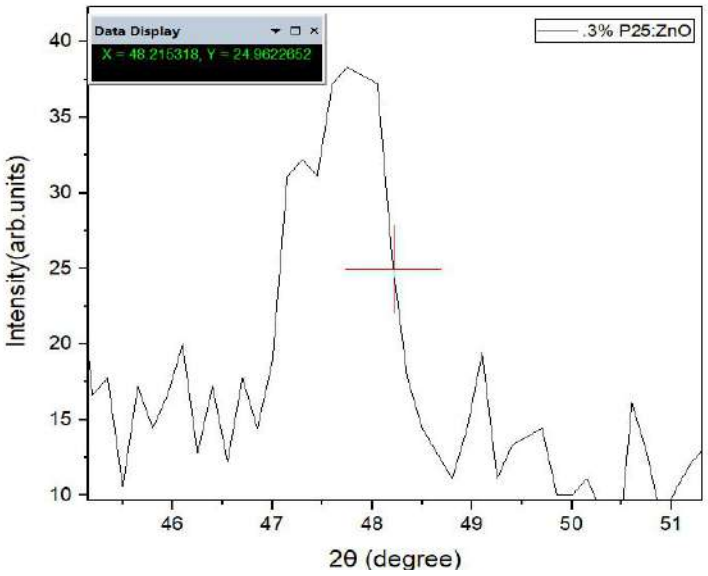

(a)

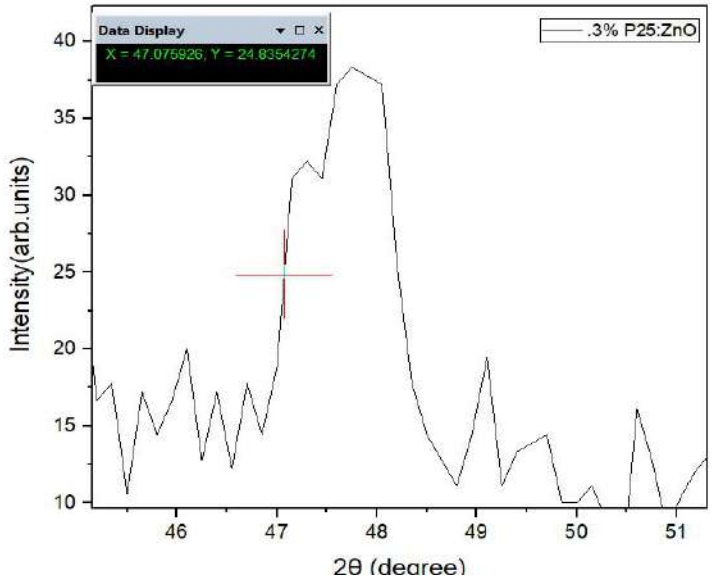

(b)

Fig. 5.22 Measurement of β_{hkl} of peak (102): (a) Value of 2θ at right of the broadening at half maximum and (b) Value of 2¬ı at left of the broadening at half maximum.

For (102) peak, the line broadening at full width half maximum (FWHM):

Bhkl = (48.215318-47.075926)

= 1.139392

In radian,

Bhkl = 1.139392×(π/180)

= 0.019886

Analysis of fifth peak (110)

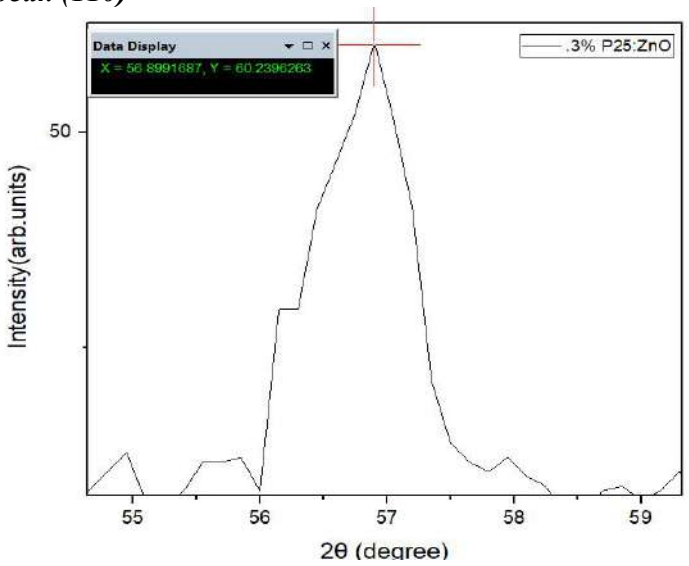

Here,
2θ=56.899169
θ=28.44958

Fig. 5.23 Measurement of θ of peak (110)

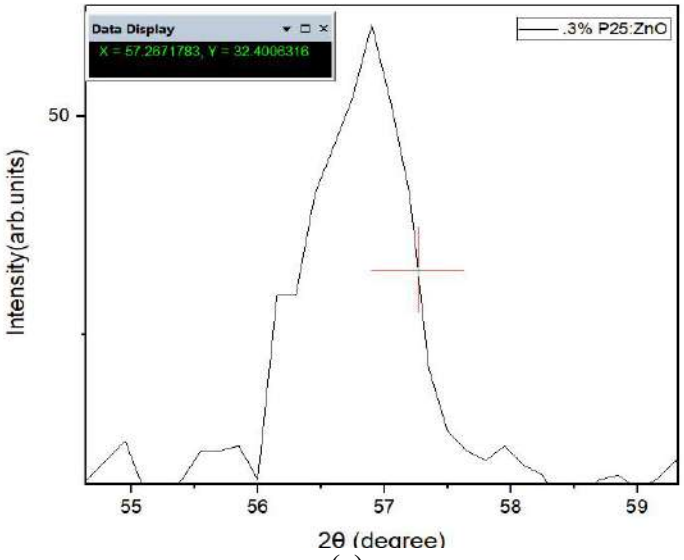

(a)

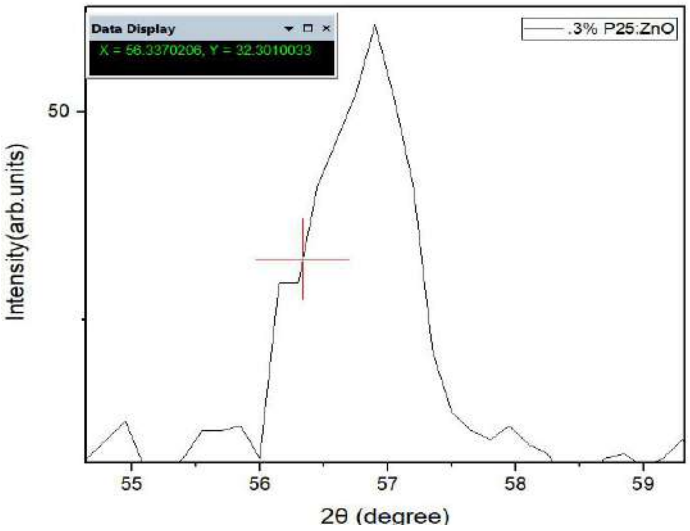

(b)

Fig. 5.24 Measurement of β_{hkl} of peak (110): (a) Value of 2θ at right of the broadening at half maximum and (b) Value of 2θ at left of the broadening at half maximum.

For (110) peak, the line broadening at full width half maximum (FWHM):

β_{hkl} = (57.2671783-56.3370206)

= 0.9301577

In radian,

β_{hkl} = 0.9301577×(π/180)

= 0.0162343

Analysis of sixth peak (103)

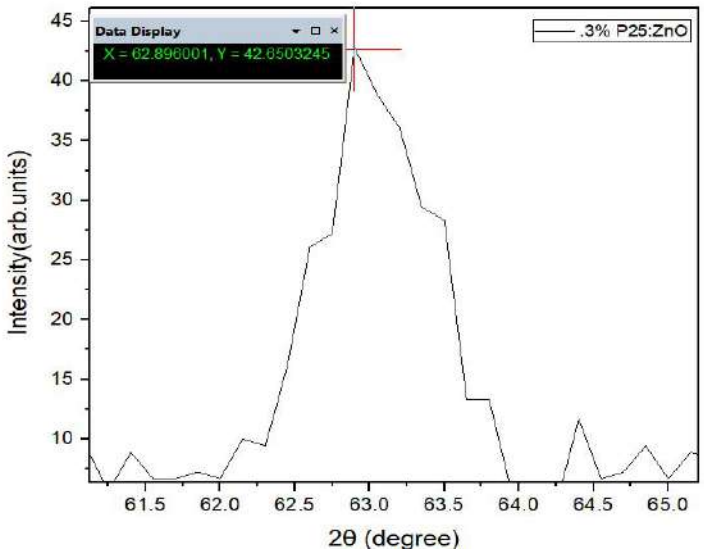

Here,
2θ=62.896 00
θ=31.4480 05

Fig. 5.25 Measurement of θ of peak (103)

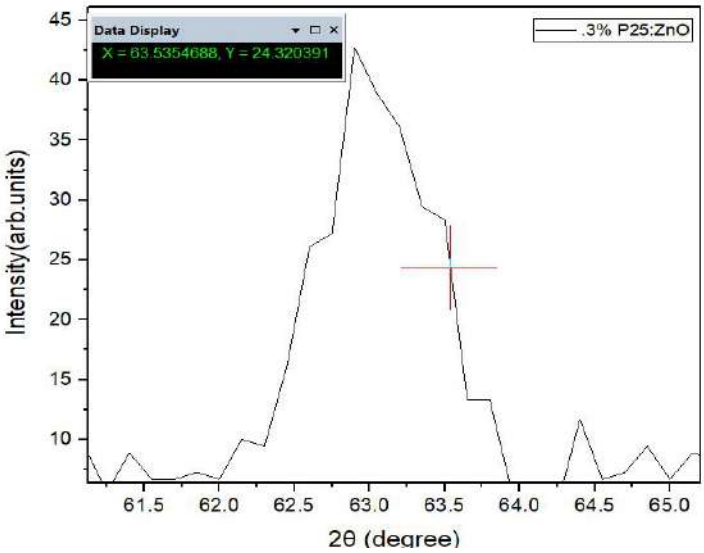

(a)

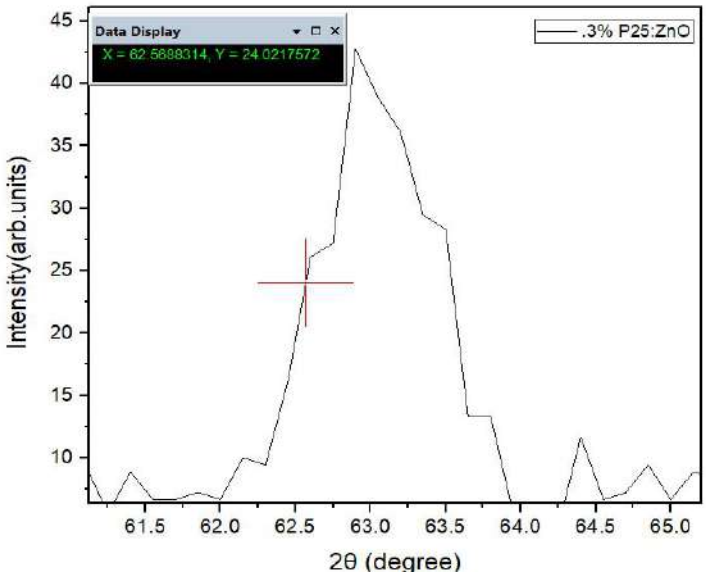

(b)

Fig. 5.26 Measurement of βhkl of peak (103): (a) Value of 2θ at right of the broadening at half maximum and (b) Value of 2θ at left of the broadening at half maximum.

For (103) peak, the line broadening at full width half maximum (FWHM):

βhkl = (63.16241-62.7531)

= 0.48710

In radian,

βhkl = 0.48710×(π/180)

= 0.0085014

5.4 XRD analysis of 0.2% P25: ZnO tetraphenyl porphyrin doped ZnO nanoparticles

The XRD patterns of the prepared samples of ZnO nanoparticles with 1% P25 doping were shown in **Fig. 5.27**. Which is determined by placing the value of 2θ along x-axis and intensity along y-axis. All the diffraction peaks could be well indexed as the ZnO wurtzite structure found in the standard reference data.

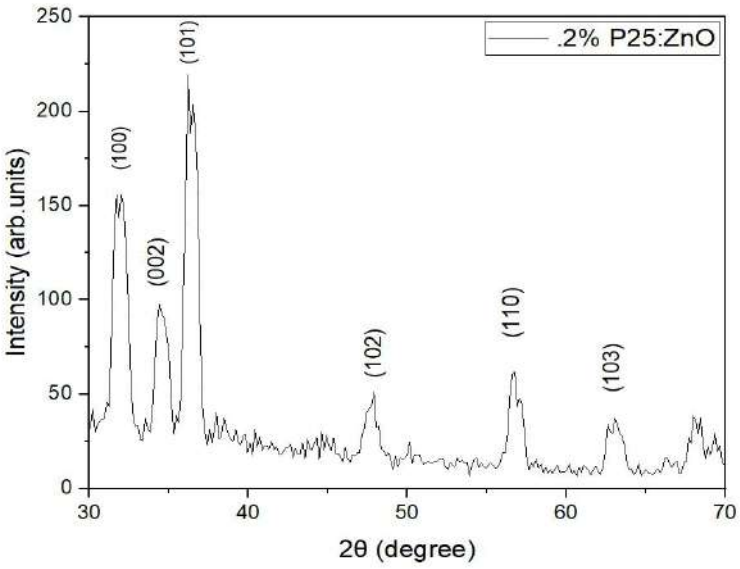

Fig. 5.27 XRD pattern of .2 % P25 doped ZnO nanoparticles

Fig. 5.28, Fig. 5.29, Fig. 5.30, Fig. 5.31, Fig. 5.32, Fig. 5.33, Fig. 5.34, Fig. 5.35, Fig. 5.36, Fig. 5.37, Fig. 5.38 and Fig. 5.39 shows analysis of the first six peaks. Bragg's angle (θ) and the line broadening at full width half maximum (FWHM) is obtained from these figures.

Analysis of first peak (100)

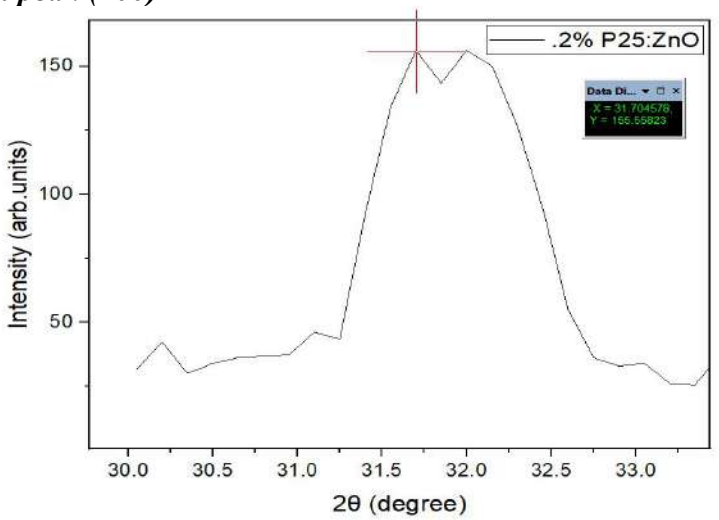

Here,
2θ=31.704 58
θ=15.8522 89

Fig. 5.28 Measurement of θ of peak (100)

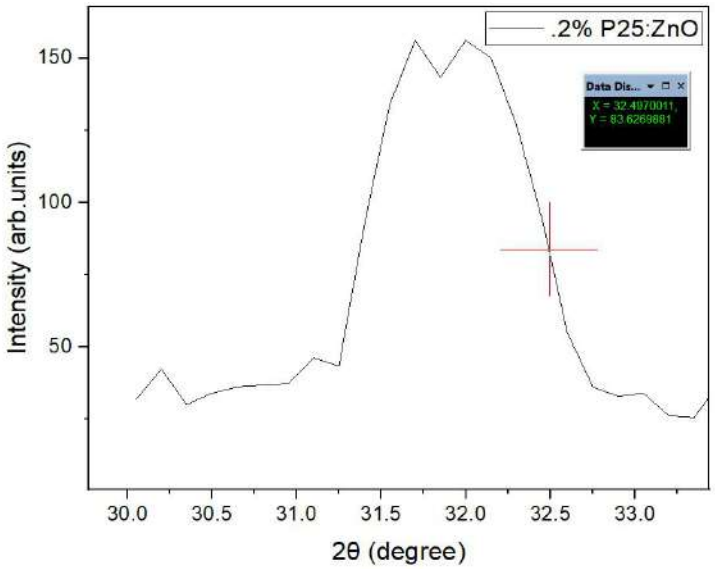

(a)

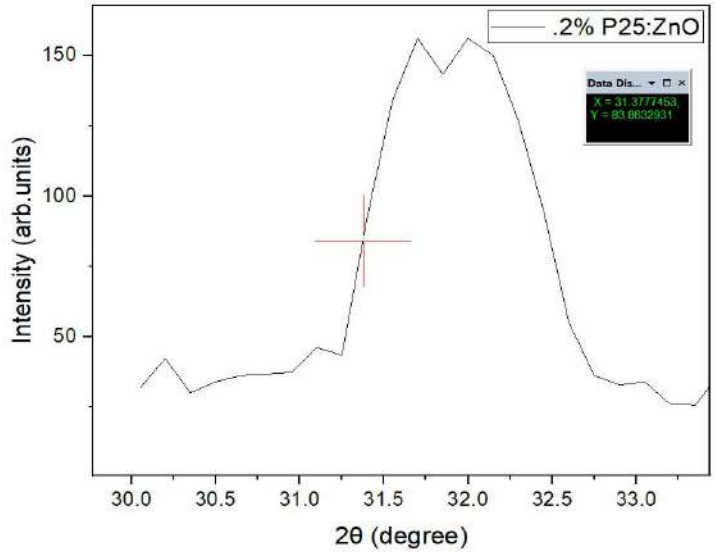

(b)

Fig. 5.29 Measurement of βhkl of peak (100): (a) Value of 2θ at right of the broadening at half maximum and (b) Value of 2θ at left of the broadening at half maximum.

For (100) peak, the line broadening at full width half maximum (FWHM):

βhkl = (32.4970011-31.3777453)

= 1.1192558

In radian,

βhkl = 1.1192558×(π/180)

= 0.0195346989

Analysis of second peak (002)

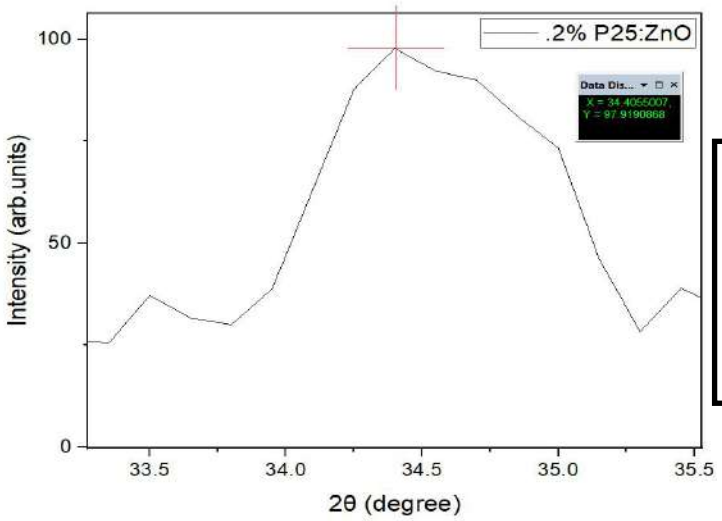

Here,
2θ=34.405
5007
θ=17.2027
5035

Fig. 5.30 Measurement of θ of peak (002)

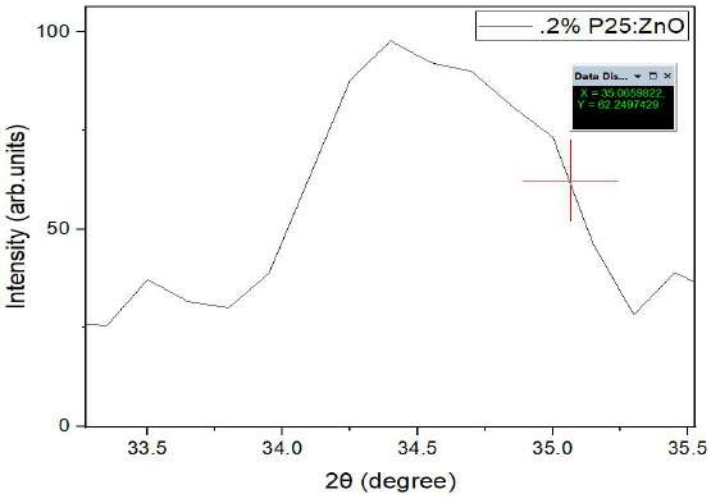

(a)

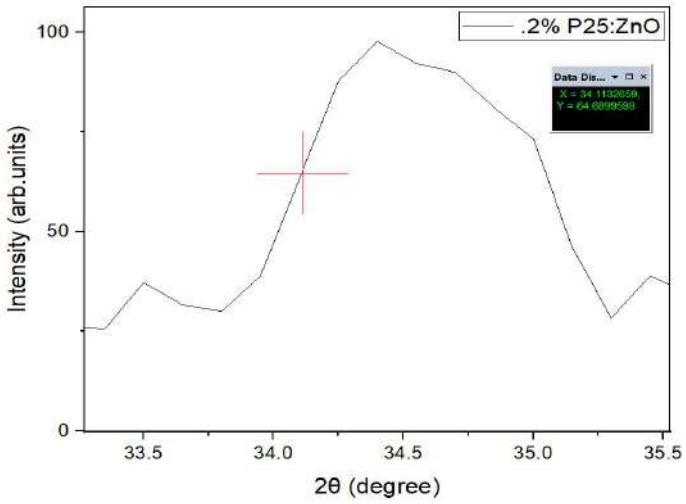

(b)

Fig. 5.31 Measurement of βhkl of peak (002): (a) Value of 2θ at right of the broadening at half maximum and (b) Value of 2θ at left of the broadening at half maximum.

For (002) peak, the line broadening at full width half maximum (FWHM):

βhkl = (35.0659822-34.1132659)

= 0.952715

In radian,

βhkl = 0.952715×(π/180)

= 0.0166280

Analysis of third peak (101)

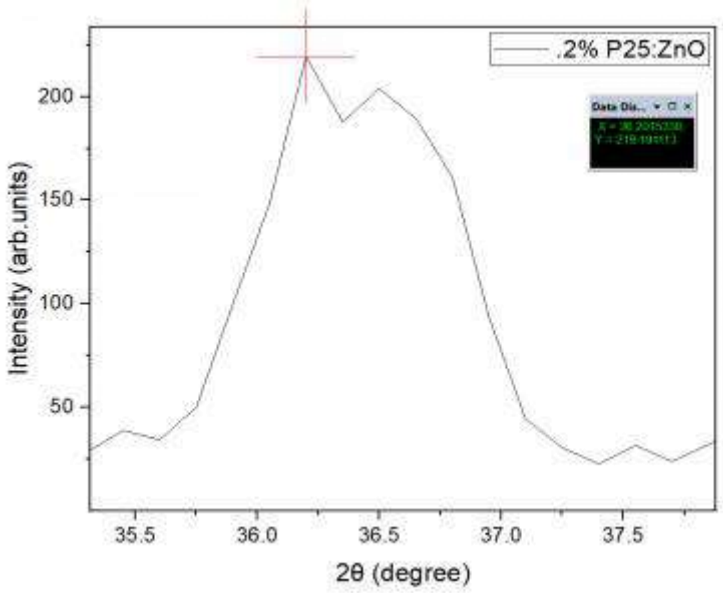

Here,
2θ=36.2015338
θ=18.1007669

Fig. 5.32 Measurement of θ of peak (101)

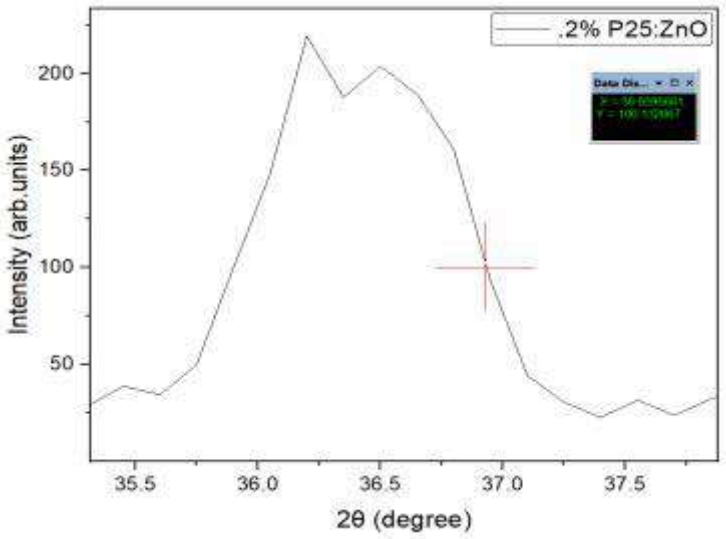

(a)

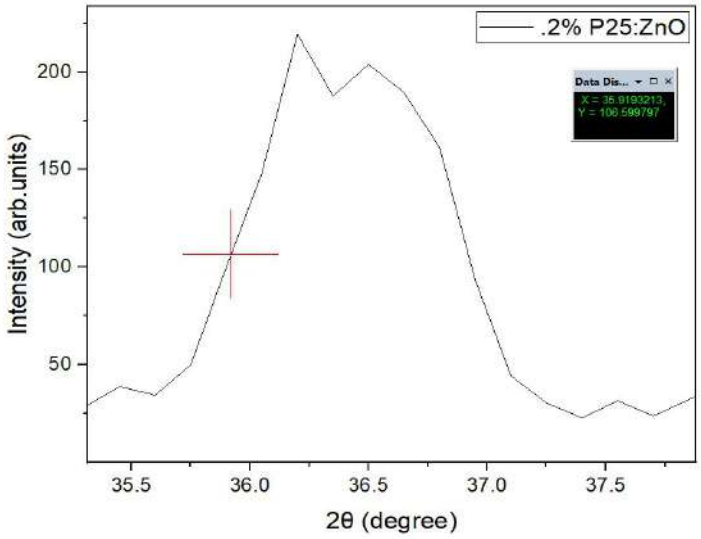

(b)

Fig. 5.33 Measurement of βhkl of peak (101): (a) Value of 2θ at right of the broadening at half maximum and (b) Value of 2θ at left of the broadening at half maximum.

For (101) peak, the line broadening at full width half maximum (FWHM):

βhkl = (36.9295601-35.9193213)

= 1.0102388

In radian,

βhkl = 1.0102388×(π/180)

= 0.01763199

Analysis of fourth peak (102)

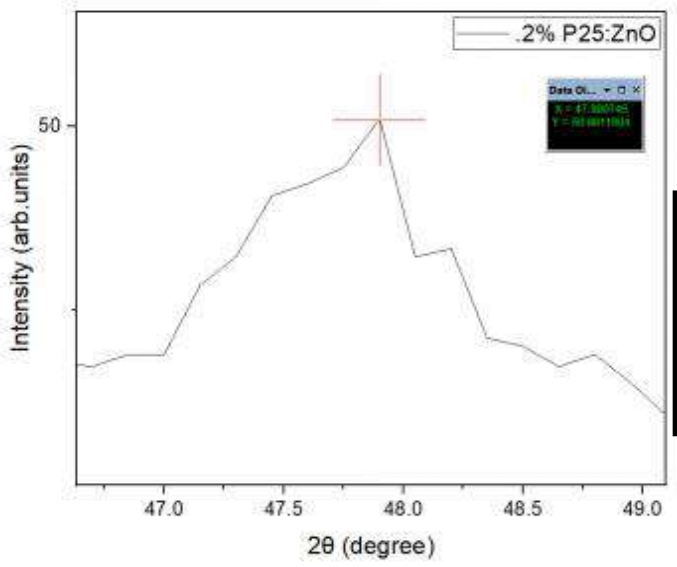

Here,
2θ=47.900745
θ=23.9503725

Fig. 5.34 Measurement of θ of peak (102)

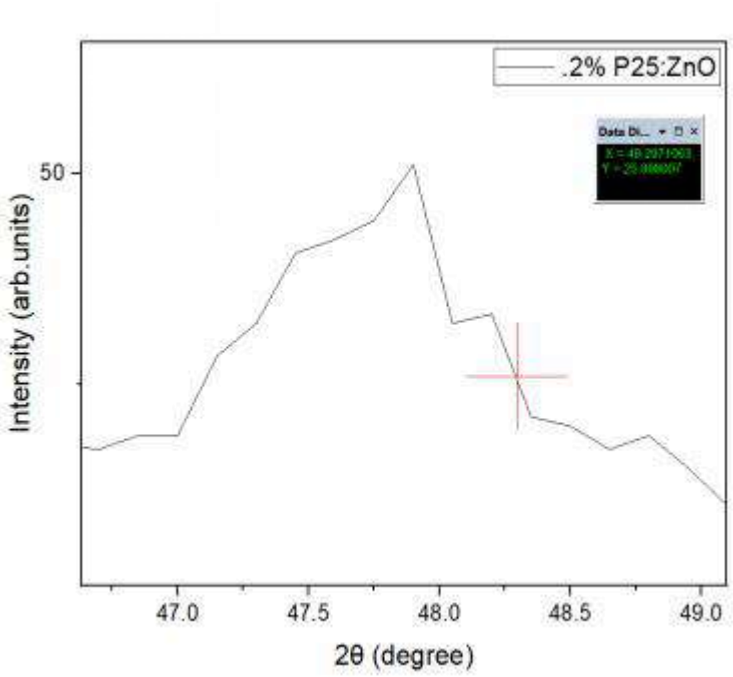

(a)

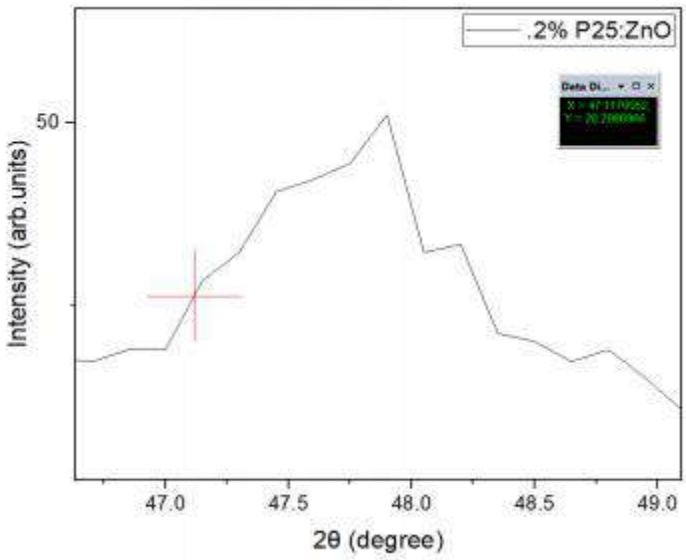

(b)

Fig. 5.35 Measurement of βhkl of peak (102): (a) Value of 2θ at right of the broadening at half maximum and (b) Value of 2θ at left of the broadening at half maximum.

For (102) peak, the line broadening at full width half maximum (FWHM):

βhkl = (48.2971063-47.11700452)

= 1.1801011

In radian,

βhkl = 1.1801011×(π/180)

= 0.020596

Analysis of fifth peak (110)

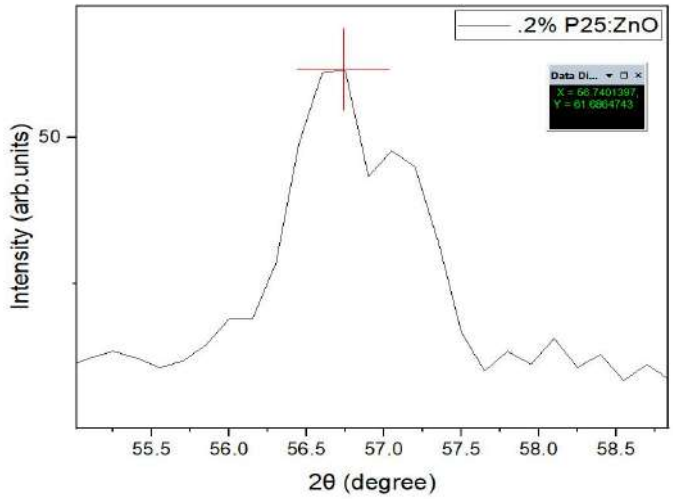

Here,
2θ=56.740
140
θ=28.3700
698

Fig. 5.36 Measurement of θ of peak (110)

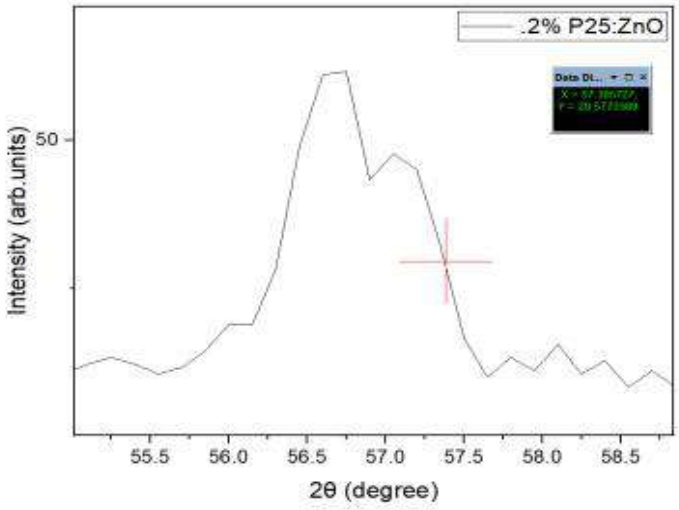

(a)

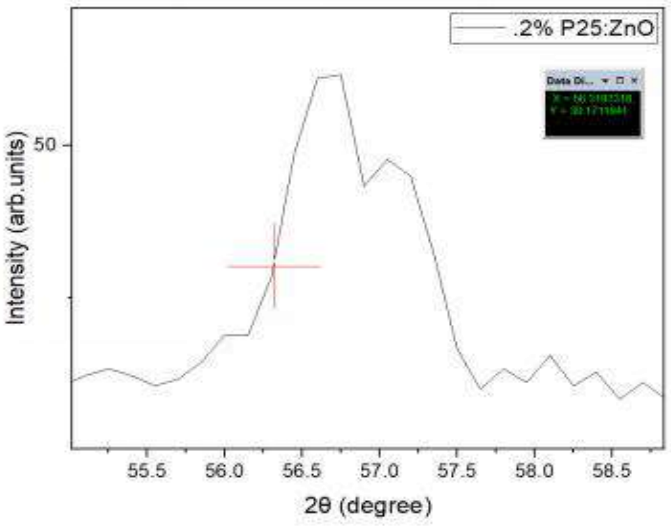

(b)

Fig. 5.37 Measurement of βhklof peak (110): (a) Value of 2θ at right of the broadening at half maximum and (b) Value of 2θ at left of the broadening at half maximum.

For (110) peak, the line broadening at full width half maximum (FWHM):

βhkl = (57.385727-56.3193318)

= 1.0663952

In radian,

βhkl = 1.0663952×(π/180)

= 0.018612107

Analysis of sixth peak (103)

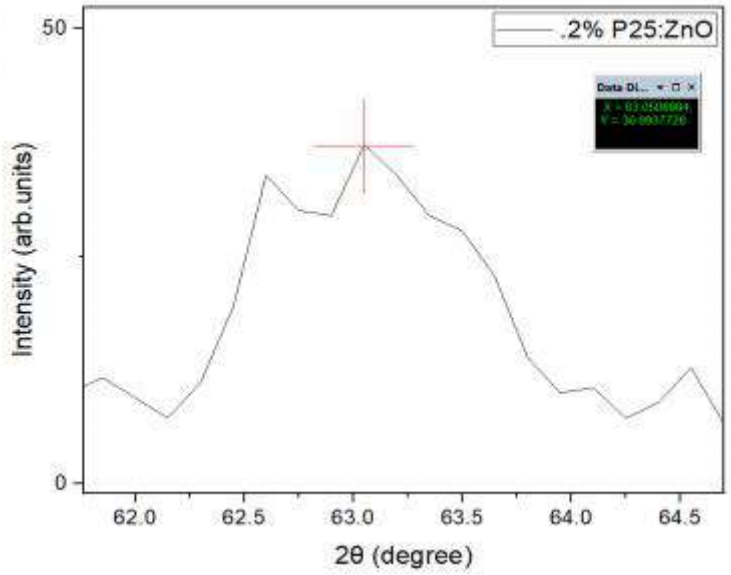

Here,
2θ=63.0508984
θ=31.5254492

Fig. 5.38 Measurement of θ of peak (103)

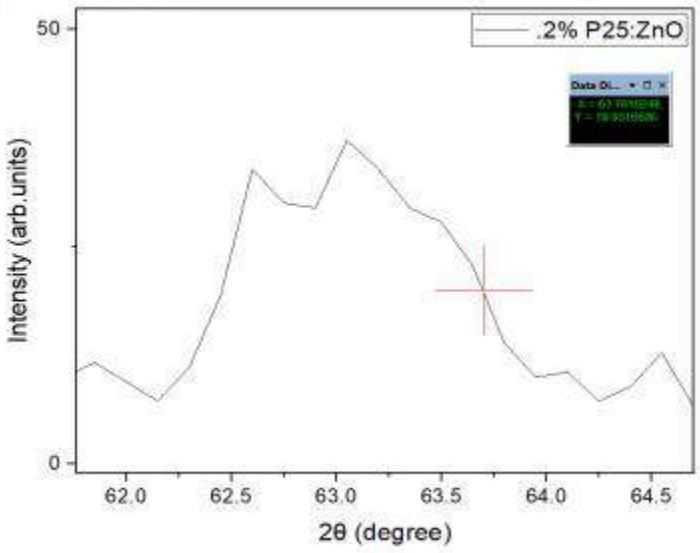

(a)

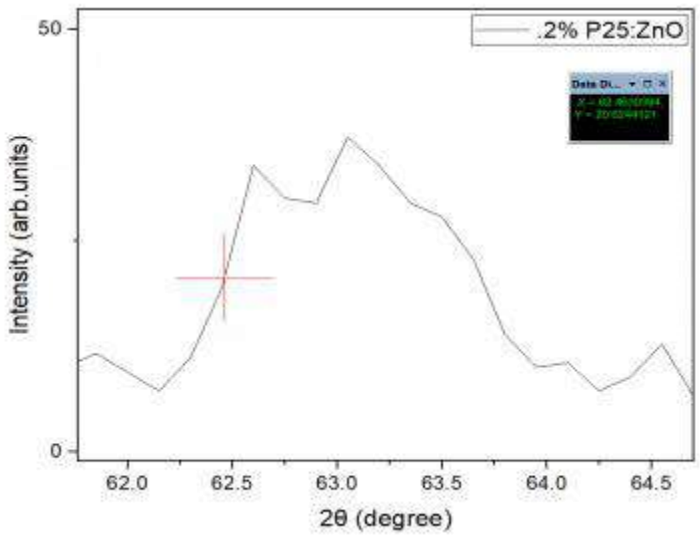

(b)

Fig. 5.39 Measurement of βhkl of peak (103): (a) Value of 2θ at right of the broadening at half maximum and (b) Value of 2θ at left of the broadening at half maximum.

For (103) peak, the line broadening at full width half maximum (FWHM):

βhkl = (63.7010248-62.46300394)

= 1.23802086

In radian,

βhkl = 01.23802086×(π/180)

= 0.0216075

5.5 XRD analysis of 0.1% P25:ZnO tetraphenylporphyrin doped ZnO nanoparticles

The XRD patterns of the prepared samples of ZnO nanoparticles with % P25 doping were shown in **Fig. 5.40**. Which is determined by placing the value of 2θ along x-axis and intensity along y-axis. All the diffraction peaks could be well indexed as the ZnO wurtzite structure found in the standard reference data.

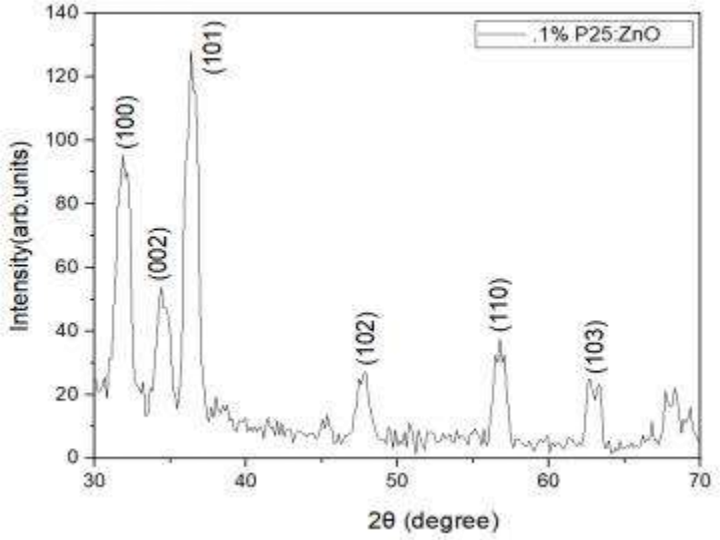

Fig. 5.40 XRD pattern of 0.1 % P25 doped ZnO nanoparticles

Fig. 5.41, Fig.5. 42, Fig. 5.43, Fig. 5.44, Fig. 5.45, Fig. 5.46, Fig. 5.47, Fig. 5.48, Fig. 5.49, Fig. 5.50, Fig. 5.51 and Fig. 5.52 shows analysis of the first six peaks. Bragg's angle (θ) and the line broadening at full width half maximum (FWHM) is obtained from these figures.

Analysis of first peak (100)

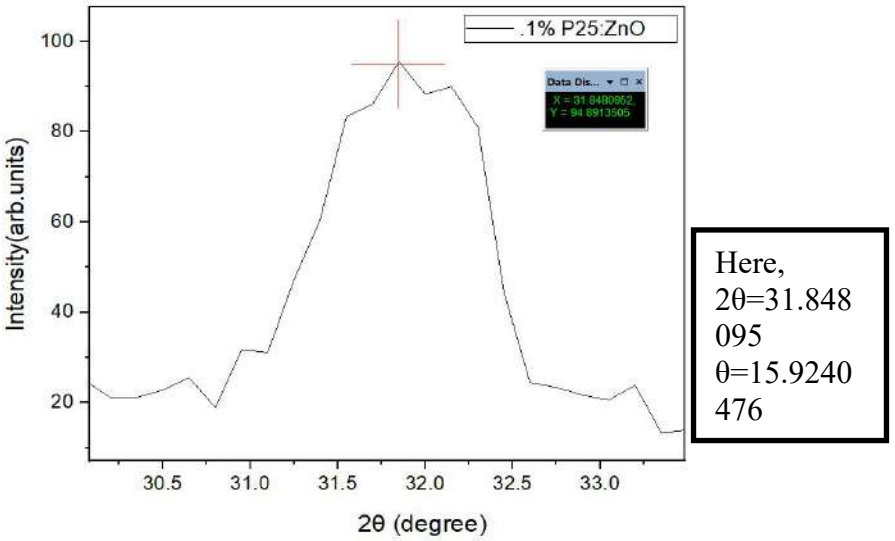

Fig. 5.41 Measurement of θ of peak (100)

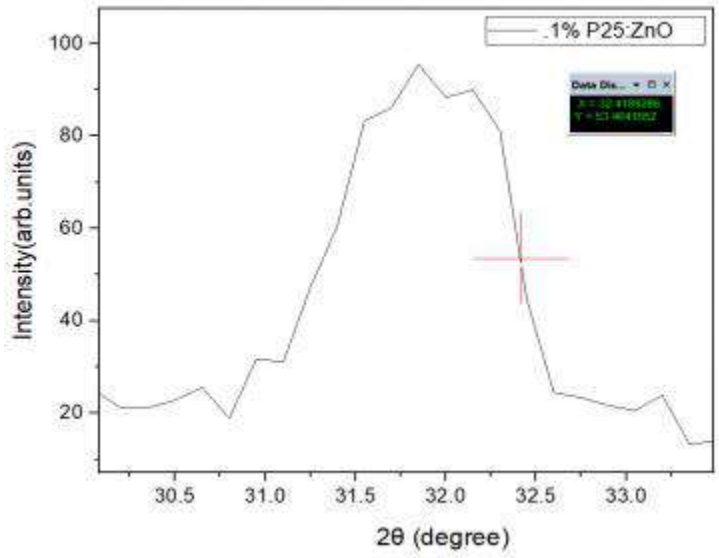

(a)

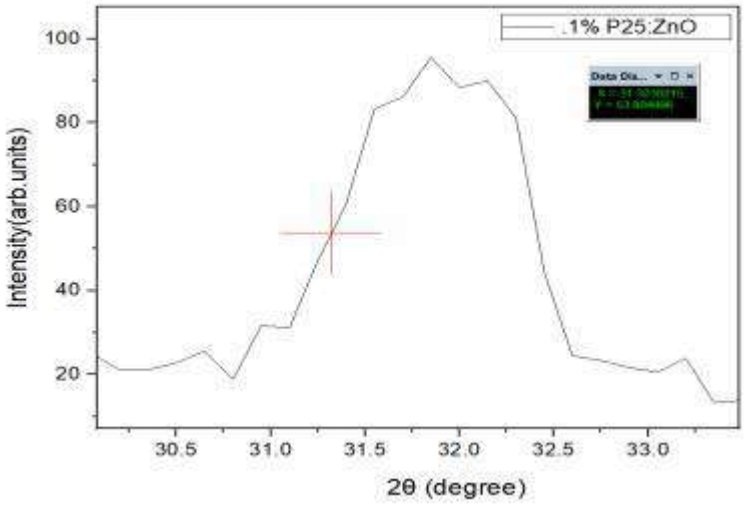

(b)

Fig. 5.42 Measurement of βhkl of peak (100): (a) Value of 2θ at right of the broadening at half maximum and (b) Value of 2θ at left of the broadening at half maximum.

For (100) peak, the line broadening at full width half maximum (FWHM):

βhkl = (32.4189286-31.3230215)

= 1.095907

In radian,

βhkl = 1.095907×(π/180)

= 0.01912718

Analysis of second peak (002)

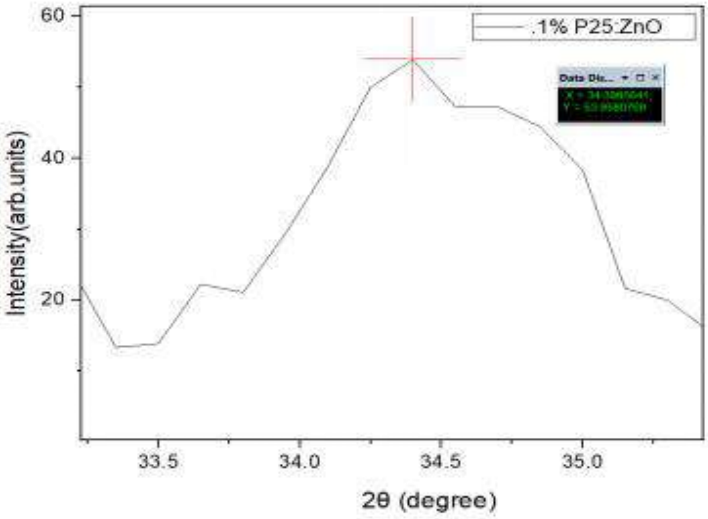

Here,
2θ=34.398564
θ=17.1992821

Fig. 5.43 Measurement of θ of peak (002)

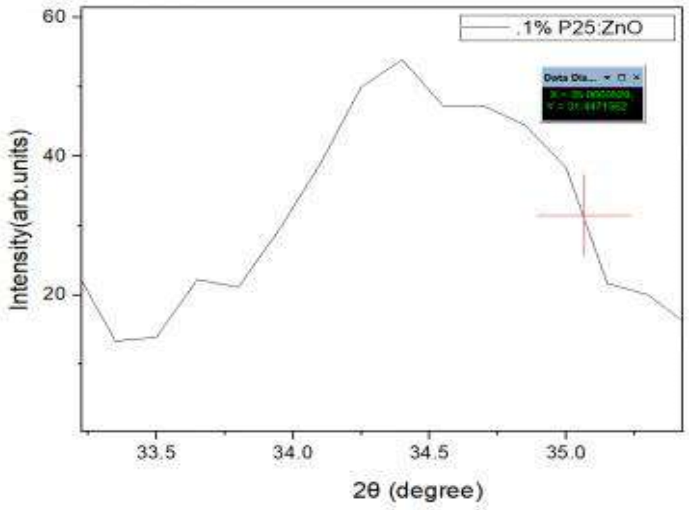

(a)

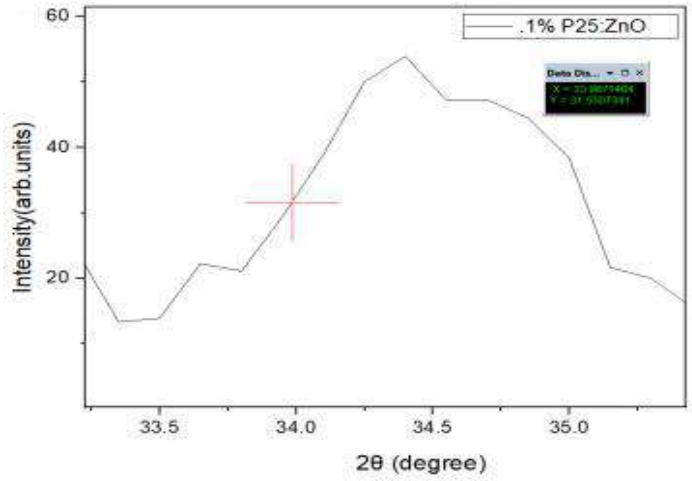

(b)

Fig. 5.44 Measurement of βhkl of peak (002): (a) Value of 2θ at right of the broadening at half maximum and (b) Value of 2θ at left of the broadening at Half maximum.

For (002) peak, the line broadening at full width half maximum (FWHM):

βhkl = (35.0660529-33.9871464)

= 1.078906

In radian,

βhkl = 1.078906×(π/180)

= 0.01883047

Analysis of third peak (101)

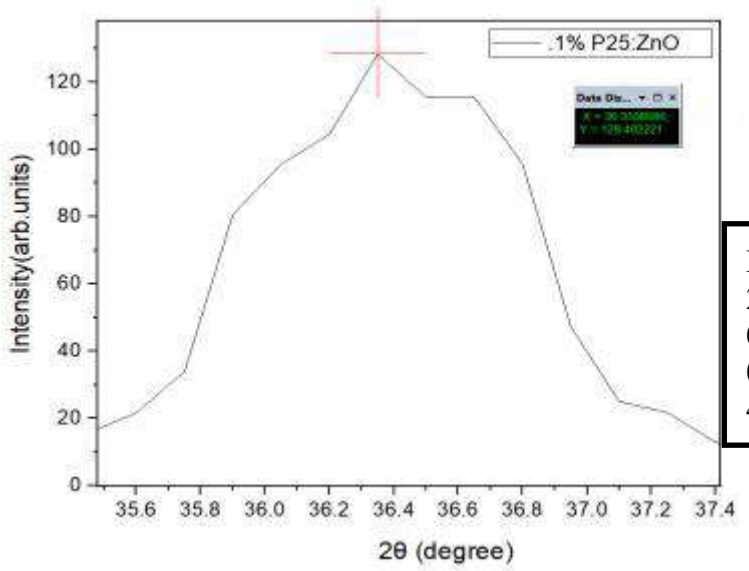

Here,
2θ=36.35081
θ=18.175404

Fig. 5.45 Measurement of θ of peak (101)

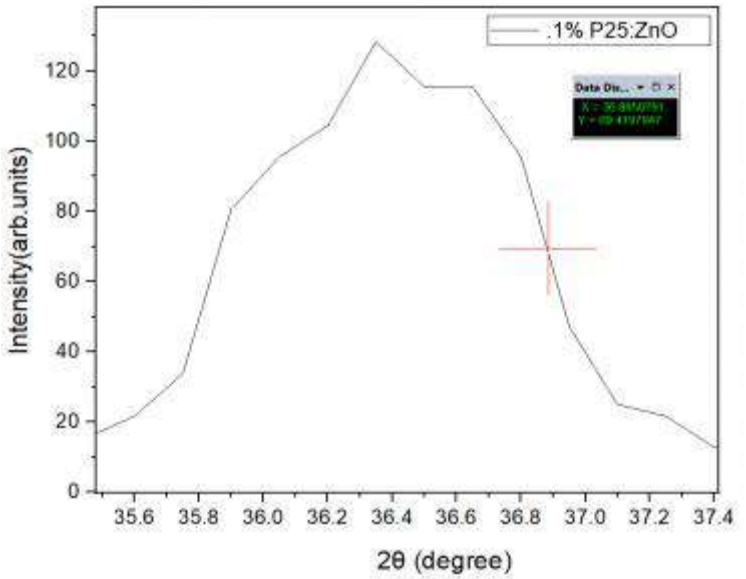

(a)

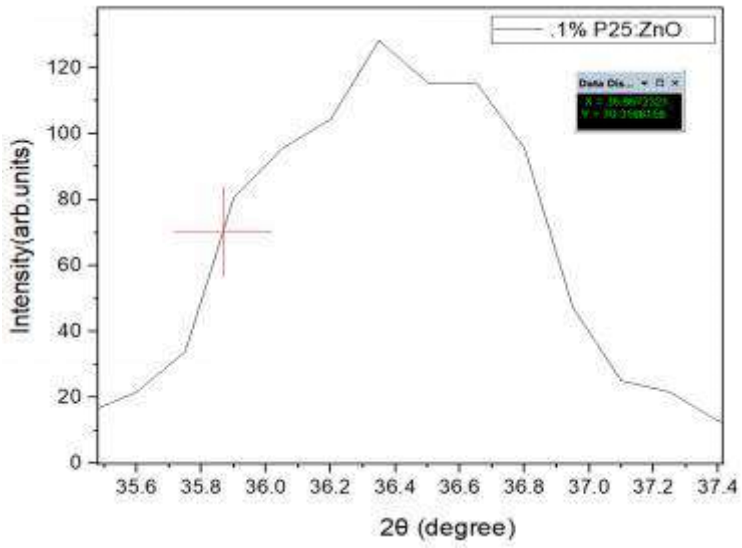

(b)

Fig. 5.46 Measurement of βhkl of peak (101): (a) Value of 2θ at right of the broadening at half maximum and (b) Value of 2θ at left of the broadening at half maximum.

For (101) peak, the line broadening at full width half maximum (FWHM):

βhkl = (36.8850791-35.8672321)

= 1.017847

In radian,

βhkl = 1.017847×(π/180)

= 0.017764878

Analysis of fourth peak (102)

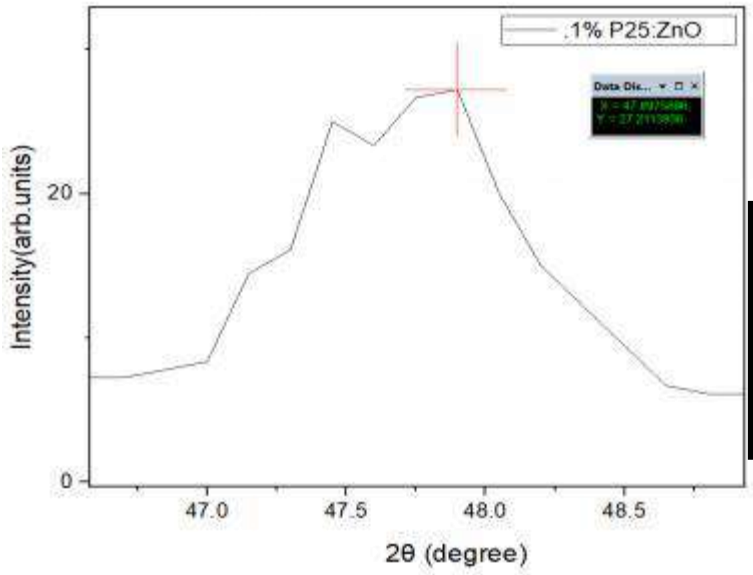

Here,
2θ=47.897589
θ=23.948743

Fig. 5.47 Measurement of θ of peak (102)

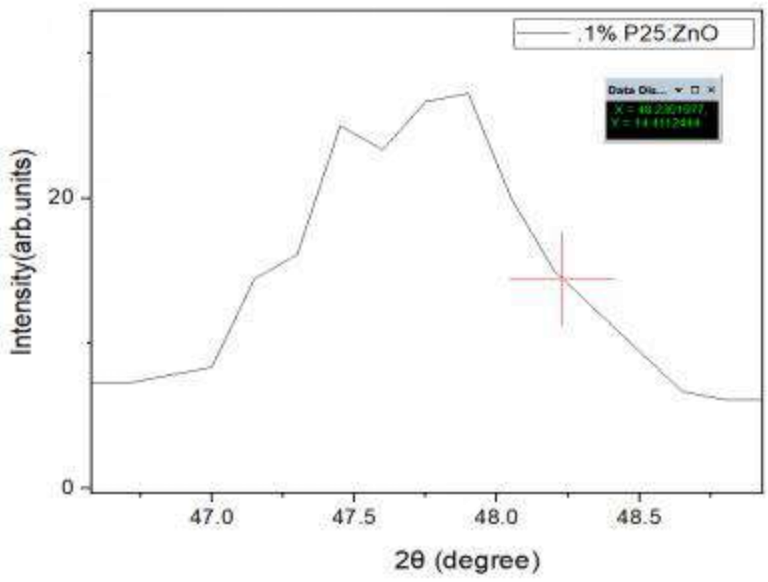

(a)

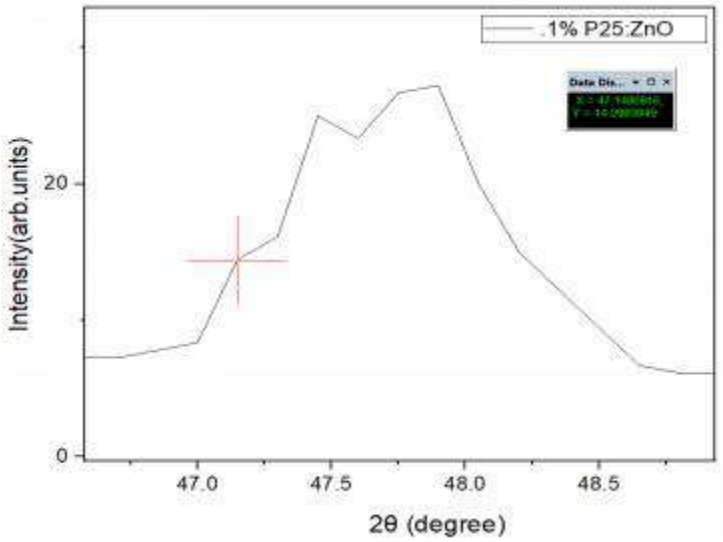

(b)

Fig. 5.48 Measurement of βhklof peak (102): (a) Value of 2θ at right of the broadening at half maximum and (b) Value of 2θ at left of the broadening at half maximum.

For (102) peak, the line broadening at full width half maximum (FWHM):

βhkl = (48.2301977-47.1486816)

= 1.0815161

In radian,

Bhkl = 1.0815161×(π/180)

= 0.0188760169

Analysis of fifth peak (110)

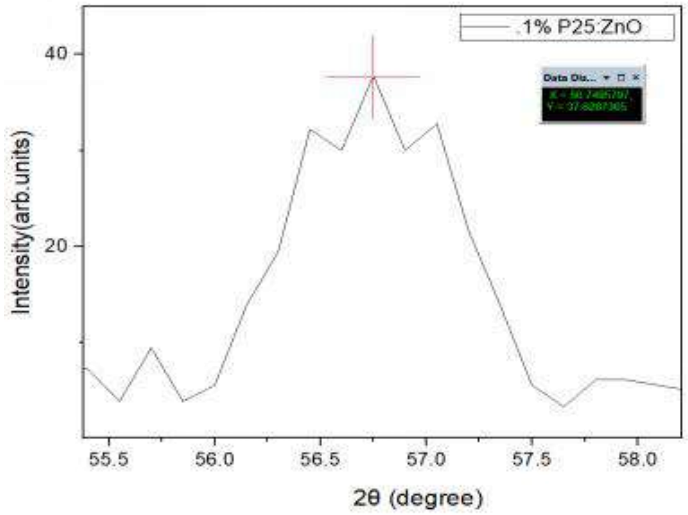

Here,
2θ=56.748580
θ=28.37428 99

Fig. 5.49 Measurement of θ of peak (110)

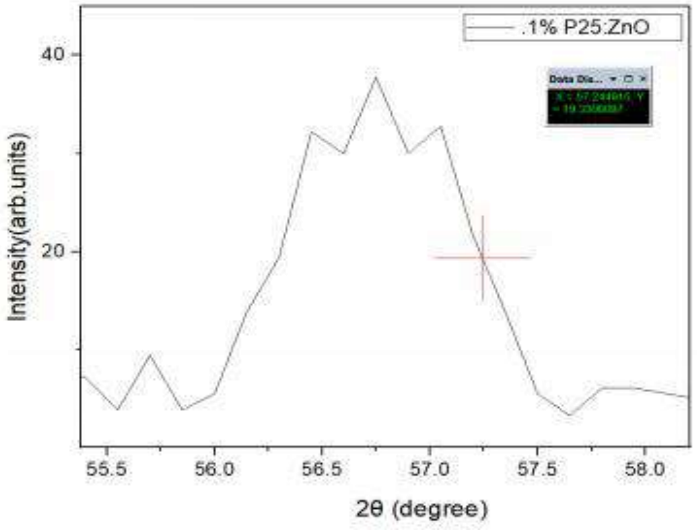

(a)

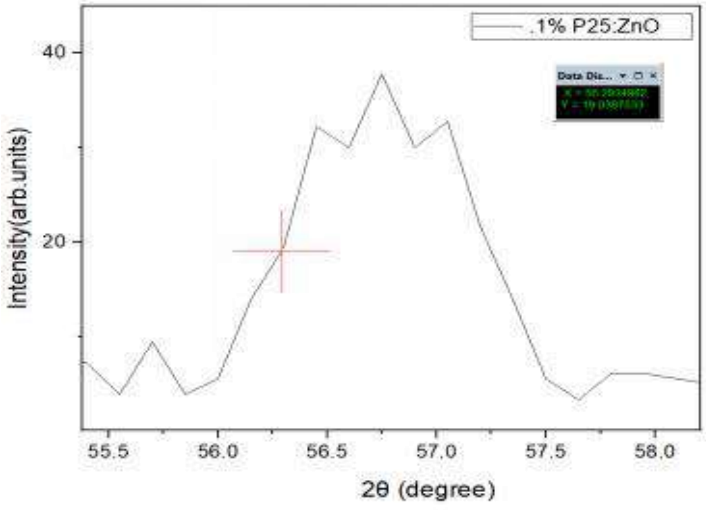

(b)

Fig. 5.50 Measurement of βhkl of peak (110): (a) Value of 2θ at right of the broadening at half maximum and (b) Value of 2θ at left of the broadening at half maximum.

For (110) peak, the line broadening at full width half maximum (FWHM):

βhkl = (57.2449-56.293498)

= 0.951402

In radian,

βhkl = 0.951402×(π/180)

= 0.016605097

Analysis of sixth peak (103)

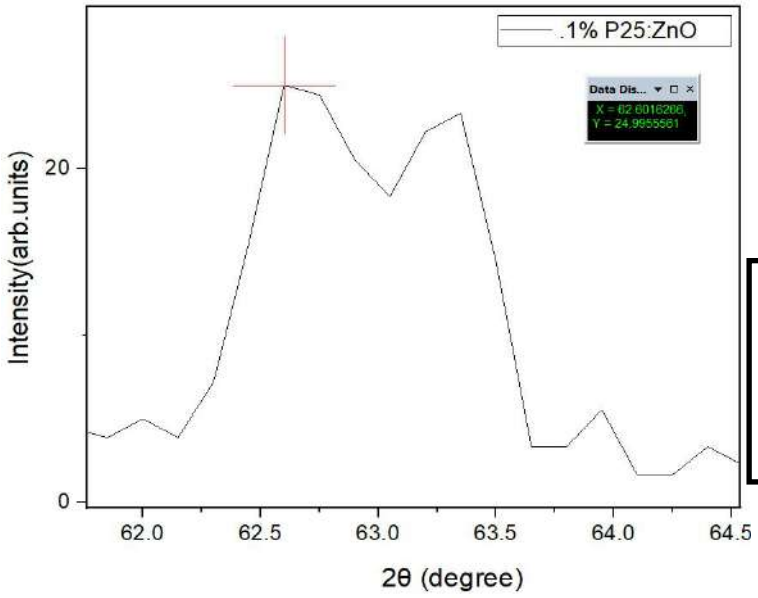

Here,
2θ=62.601627
θ=31.3008138

Fig. 5.51 Measurement of θ of peak (103)

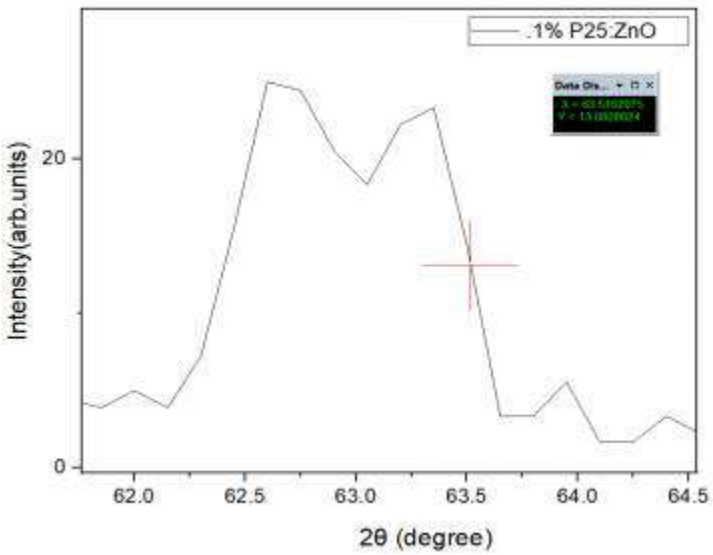

(a)

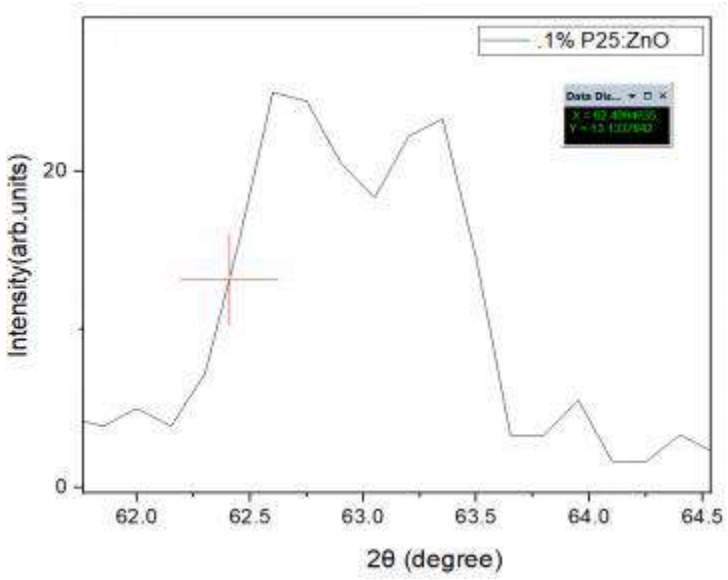

(b)

Fig. 5.52 Measurement of βhkl of peak (103): (a) Value of 2θ at right of the broadening at half maximum and (b) Value of 2θ at left of the broadening at half maximum.

For (103) peak, the line broadening at full width half maximum (FWHM):

βhkl = (63.516297-62.4094635)

= 1.1068335

In radian,

βhkl = 1.1068335×(π/180)

= 0.01931788

5.6 Determination of Lattice parameters.

There are three lattice parameters namely a, b, & c. If the ratio of c and a i.e c/a is equals to about 1.63 then it's a perfect wurtzite structure having a hexagonal unit celll. For a Hexagonal unit cell, a = b. Thus following formulas are used to determine the value of a & c:

Formula for lattice constant a:

$$a = \frac{\lambda}{\sqrt{3}\sin\theta(100)} \tag{5.6}$$

Formula for lattice constant c:

$$c = \frac{\lambda}{\sin\theta(002)} \tag{5.7}$$

Table 5.6 Lattice parameters of ZnO NPs without doping

βhkl	Lattice Parameters (*Å*)	c/a ratio	Structure
(100)	a=3.24	1.6	Hexagonal
(002)	C=5.17		

Table 5.7 Lattice parameters of ZnO NPs with P25 doping

P25 (%)	βhkl	Lattice Parameters (*Å*)	c/a ratio	Structure
0.3 %	(100)	a=3.21	1.601	Hexagonal
	(002)	c=5.14		
0.2 %	(100)	a=3.25	1.6	Hexagonal
	(002)	c=5.20		
0.1 %	(100)	a=3.24	1.604	Hexagonal
	(002)	c=5.20		

Table 5.6 & Table 5.7 concludes that the structure of ZnO NPs both with and without doping is hexagonal as the ratio c/a is almost 1.6.

5.7 Determination of crystallite parameters using Williamson and Hall Method

Three modified W-H models are used to determined crystallite size (D), lattice strain (ε), stress (σ) and energy density (u) of ZnO NPs with and without doping.

1. Uniform deformation model (UDM)
2. Uniform stress deformation model (USDM)
3. Uniform deformation energy density model (UDEDM)

5.7.1 Determination of crystallite size and lattice strain by Uniform deformation model (UDM)

The W-H equation can be written as

$$\beta_{hkl} = \frac{K\lambda}{D.\cos\theta} + 4.\varepsilon.\tan\theta \qquad (5.8)$$

Rearranging Eq. (5.8)

$$\beta_{hkl}\cos\theta = \frac{K\lambda}{D} 4.\varepsilon.\sin\theta_{hkl} \qquad (5.9)$$

This equation is identical to straight line equation which represents the uniform deformation model (UDM) equation. It considers the isotropic nature of the crystals.

Plotting of this equation (5.9) in a way that the term (4Sinθ) along X-axis and (β_{hkl}.Cosθ) along Y-axis corresponding to each diffraction peak for ZnO NPs, the slope of this straight line provides the value of the intrinsic strain, whereas the intercept provides the average particle size of the ZnO nanocrystals.

The value of (4Sinθ) and (βhkl.Cosθ) of ZnO NPs with and without ZnO doping are shown in **Table 5.8**, **Table 5.9, Table 5.10 and Table 5.11.**

Table 5.8 Values for UDM plot for ZnO without doping

Peak	**β_{hkl}(rad.)**	**θ**	**cosθ**	**4sinθ**	**β_{hkl}cosθ**
100	0.009875	15.9198	0.96165	1.09718	0.009496
002	0.008684	17.2996	0.95476	1.18947	0.008291
101	0.016277	18.2016	0.94996	1.24944	0.015462
102	0.008473	23.8964	0.91428	1.62034	0.007748
110	0.009056	28.4026	0.87963	1.90266	0.007966
103	0.011581	31.5229	0.85243	2.09136	0.009872

Table 5.9 Values for UDM plot ZnO with .3% P25 doping

Peak	**β_{hkl}(rad.)**	**θ**	**cosθ**	**4sinθ**	**β_{hkl}cosθ**
100	0.01863	16.07785	0.96088	1.10778	0.01790
002	0.01392	17.42481	0.95411	1.19782	0.01327
101	0.01482	18.32292	0.94929	1.25749	0.01407
102	0.01989	23.87711	0.91441	1.61911	0.01817
110	0.01623	28.44958	0.87923	1.90554	0.01427
103	0.01687	31.44800	0.85311	2.08689	0.01439

Table 5.10 Values for UDM plot ZnO with .2% P25 doping

Peak	β_{hkl}(rad.)	θ	cosθ	4sinθ	β_{hkl}cosθ
100	0.0195346	15.852289	0.961969	1.0928633	0.0187917
002	0.016628	17.20275	0.95526	1.183015	0.015884
101	0.017631	18.100767	0.95051	1.242756	0.016759
102	0.020596	23.95037	0.913897	1.6237806	0.0188226
110	0.018612	28.370069	0.879896	1.900658	0.0163767
103	0.0216075	31.525449	0.852408	2.0915089	0.0184184

Table 5.11 Values for UDM plot ZnO with .1% P25 doping

Peak	β_{hkl}(rad.)	θ	cosθ	4sinθ	β_{hkl}cosθ
100	0.0191272	15.924047	0.961626	1.09745	0.018393
002	0.0188305	17.09928	0.95528	1.18278	0.0179883
101	0.017765	18.175404	0.95010	1.247708	0.016877
102	0.0188760	23.948794	0.913908	1.62368	0.017250
110	0.0166050	28.374289	0.8798619	1.90091	0.014610
103	0.0193178	31.3008	0.854451	2.07812	0.0165061

Now, by placing 4sinθ values along the x-axis and cosθ values along y-axis Fig. 5.57, Fig. 5.58, Fig. 5.59, & Fig. 5.60 is drawn. From these figures, y-intercept and slope are obtained to determine the parameters crystallite size (D) and lattice strain (ε). Equations for detrmining these parameters are:

$$D = \frac{K\lambda}{y-intercept} \tag{5.10}$$

$$\varepsilon = slope \tag{5.11}$$

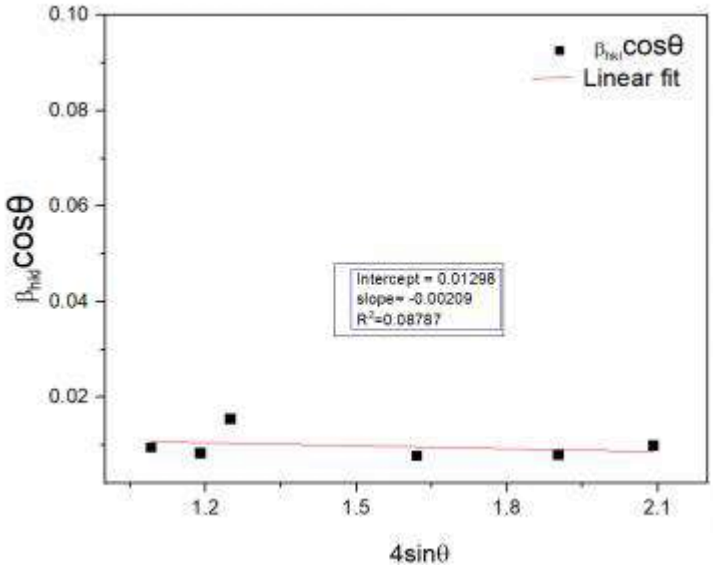

Fig. 5.53 Plot of $\beta_{hkl}\cos\theta$ versus $4\sin\theta$ for ZnO NPs withot doping.

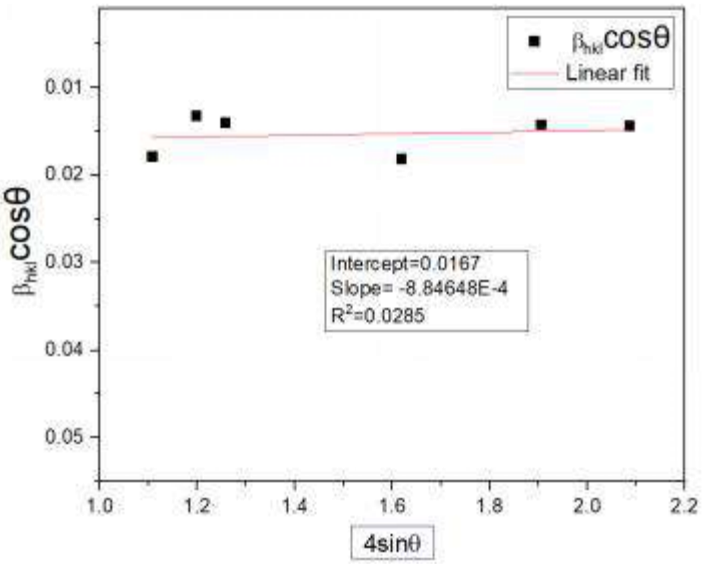

Fig. 5.54 Plot of $\beta_{hkl}\cos\theta$ versus $4\sin\theta$ for ZnO NPs with .3% P25 doping.

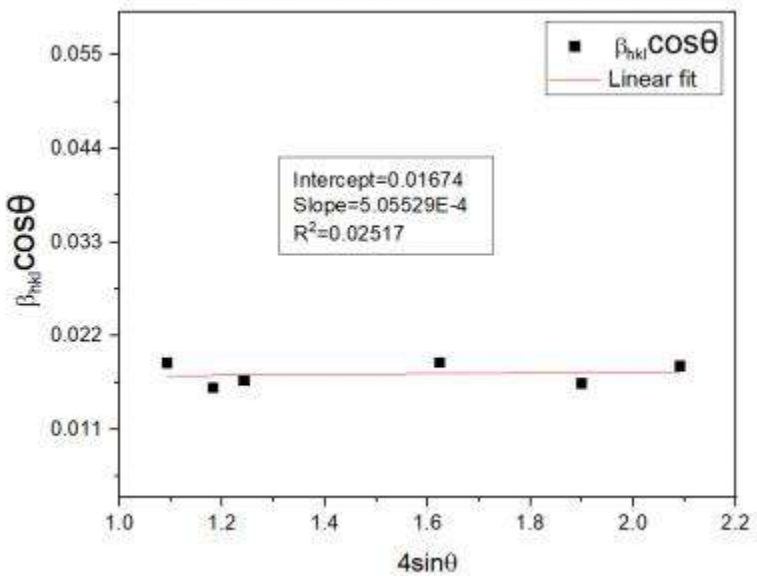

Fig. 5.55 Plot of $\beta_{hkl}\cos\theta$ versus $4\sin\theta$ for ZnO NPs with .2% P25 doping.

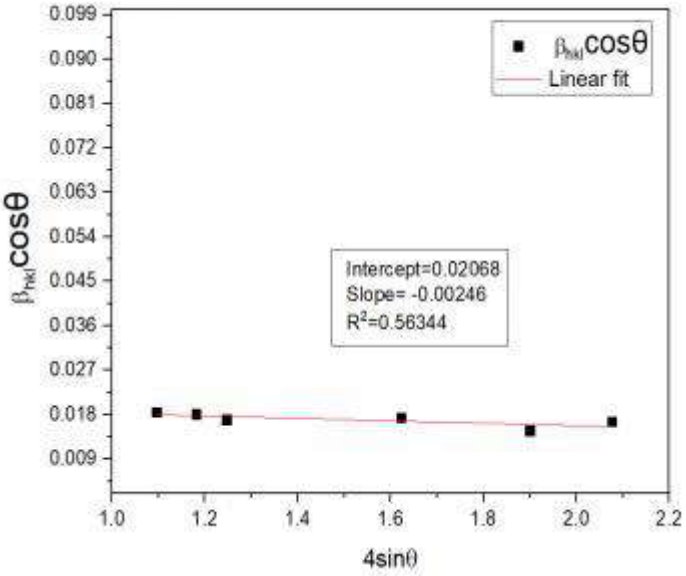

Fig. 5.56 Plot of $\beta_{hkl}\cos\theta$ versus $4\sin\theta$ for ZnO NPs with .1% P25 doping.

Crystallite size (D) & lattice strain (ε) obtained from UDM is shown in Table 5.12.

Table 5.12 Values of Crystallite size (D) & lattice strain (ε) of ZnO NPs with and without P25 doping obtained by UDM.

P25 %	Crystallite Size (nm)	Lattice Strain (ε)($*10^{-3}$)
0	10.67	2.09
.3	8.29	8.84
.2	8.27	5.05
.1	6.70	2.46

5.7.2 Uniform Stress Deformation Model (USDM)

According to Hooke‘s law, stress and strain have a linear relationship, where stress is expressed as $\sigma = \varepsilon * Y_{hkl}$, Y_{hkl} being the modulus of elasticity or Young‘s modulus. So, strain can be expressed as, $\varepsilon = \sigma/Y_{hkl}$.

Because of the size confinement, the intrinsic strain in the crystals causes a small amount of internal tension. USDM took into account stress-induced XRD peak broadening and the anisotropic aspect of Young's modulus [53]. We get by putting the value of ε in equation (5.9) and rearrangement,

$$\beta hkl \cos\theta hkl = \frac{K\lambda}{D} + 4.\sigma.\frac{\sin\theta_{hkl}}{Y_{hkl}} \tag{5.12}$$

This is the uniform stress deformation model, which considers uniform stress in all crystallographic directions and is based on the modified W–H equation. For cubic crystal, Young's modulus Y_{hkl} can be expressed as [54],

$$Y_{hkl} = \frac{\left[h^2+\frac{(h+2k)^2}{3}+\left(\frac{al}{c}\right)^2\right]^2}{S_{11}\left(h^2+\frac{(h+2k)^2}{3}\right)^2+S_{33}\left(\frac{al}{c}\right)^4+(2S_{13}+S_{44})\left(h^2+\frac{(h+2k)^2}{3}\right)\left(\frac{al}{c}\right)^2} \tag{5.13}$$

Plot of equation (5.12), with the term ($4\sin\theta/Y_{hkl}$) along X-axis and ($\beta_{hkl}.\cos\theta$) along Y-axis corresponding to each peak in the XRD pattern for ZnO nanoparticles, the slope of this plotted straight line provides the value of stress, whereas the intercept gives the average particle size of the ZnO nanocrystals. The value of ($\beta_{hkl}.\cos\theta$) & ($4\sin\theta/Y_{hkl}$) is shown in Table 5.13, Table 5.13, Table 5.13, Table 5.13

Table 5.13 Values for USDM plot ZnO without doping

Peak	**β_{hkl}(rad.)**	**θ**	**4sinθ**	**β_{hkl}cosθ**	Y_{hkl}GPa (10^9)	4sinθ/ Y_{hkl} (10^{-12})
100	0.009875	15.9198	1.09718	0.009496	127.25	8.6222
002	0.008684	17.2996	1.18947	0.008291	144.15	8.2516
101	0.016277	18.2016	1.24944	0.015462	121.43	10.2893
102	0.008473	23.8964	1.62034	0.007748	133.52	12.1356
110	0.009056	28.4026	1.90266	0.007966	127.26	14.9509
103	0.011581	31.5229	2.09136	0.009872	138.59	15.0902

Table 5.14 Values for USDM plot ZnO with .3% P25 doping

Peak	**β_{hkl}(rad.)**	**θ**	**4sinθ**	**β_{hkl}cosθ**	Y_{hkl}GPa (10^9)	4sinθ/ Y_{hkl} (10^{-12})
100	0.01863	16.07785	1.10778	0.01790	127.26	8.7048
002	0.01392	17.42481	1.19782	0.01327	144.09	8.3129
101	0.01482	18.32292	1.25749	0.01407	121.43	10.3556
102	0.01989	23.87711	1.61911	0.01817	133.52	12.1263
110	0.01623	28.44958	1.90554	0.01427	127.26	14.9735
103	0.01687	31.44800	2.08689	0.01439	138.59	15.0580

Table 5.15 Values for USDM plot ZnO with .2% P25 doping

Peak	**β_{hkl}(rad.)**	**θ**	**4sinθ**	**β_{hkl}cosθ**	Y_{hkl}GPa (10^9)	4sinθ/ Y_{hkl} (10^{-12})
100	0.0195346	15.852289	1.0928633	0.0187917	127.26	8.5858
002	0.016628	17.20275	1.183015	0.015884	144.09	8.2102
101	0.017631	18.100767	1.242756	0.016759	121.43	10.2343
102	0.020596	23.95037	1.6237806	0.0188226	133.52	12.1613
110	0.018612	28.370069	1.900658	0.0163767	127.26	14.9352
103	0.0216075	31.525449	2.0915089	0.0184184	138.59	15.0913

Table 5.16 Values for USDM plot ZnO with .1% P25 doping

Peak	**β_{hkl}(rad.)**	**θ**	**4sinθ**	**β_{hkl}cosθ**	Y_{hkl}GPa (10^9)	4sinθ/ Y_{hkl} (10^{-12})
100	0.0191272	15.924047	1.09745	0.018393	127.26	8.6236
002	0.0188305	17.09928	1.18278	0.0179883	144.09	8.2086
101	0.017765	18.175404	1.247708	0.016877	121.43	10.2051
102	0.0188760	23.948794	1.62368	0.017250	133.52	12.1605
110	0.0166050	28.374289	1.90091	0.014610	127.26	14.9372
103	0.0193178	31.3008	2.07812	0.0165061	138.59	14.9947

Now, by placing ($4Sin\theta/Y_{hkl}$) values along the x-axis and ($\beta_{hkl}.Cos\theta$) values along y axis Fig. 5.61, Fig. 5.62, Fig. 5.63, and Fig. 5.64 is drawn. From these figures, y intercept and slope are obtained to determine the parameters crystallite size (D), strain

(ε) and stress (σ). Equations for determining these parameters are:

$$D = \frac{K\lambda}{y-intercept} \tag{5.14}$$

$$\sigma = \text{Slope} \tag{5.15}$$

$$\varepsilon = \frac{\sigma}{\text{Yhkl}} \tag{5.16}$$

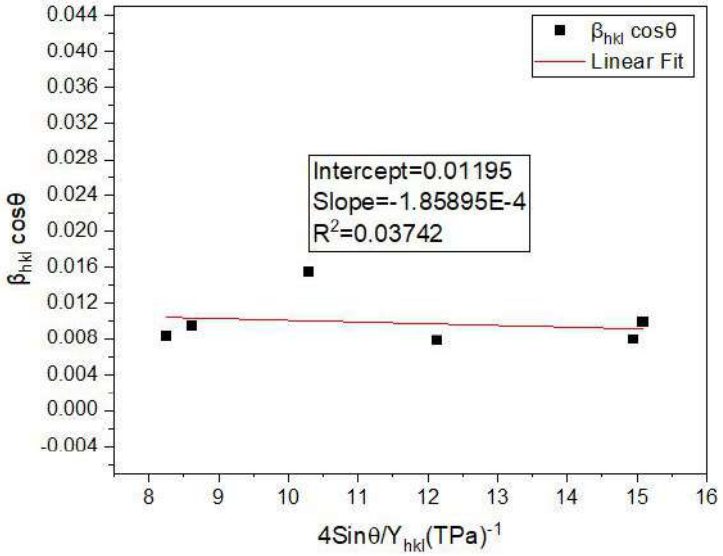

Fig. 5.57 Plot of $\beta_{hkl}\cos\theta$ versus $(4\sin\theta/Y_{hkl})$ for ZnO NPs without doping.

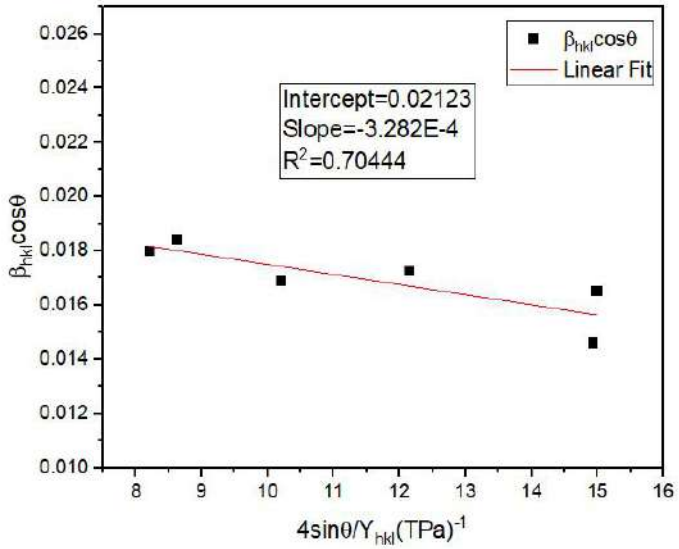

Fig. 5.58 Plot of $\beta_{hkl}\cos\theta$ versus $(4\sin\theta/Y_{hkl})$ for ZnO NPs with 0.1% P25 doping.

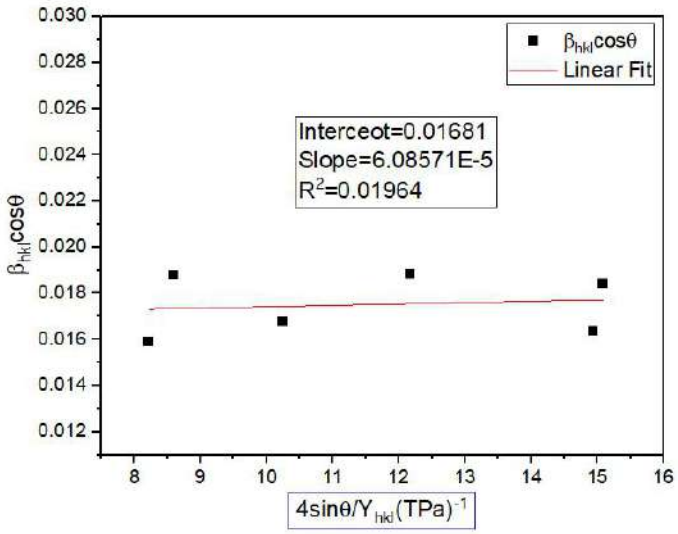

Fig. 5.59 Plot of $\beta_{hkl}\cos\theta$ versus ($4\sin\theta/Y_{hkl}$) for ZnO NPs with .2% P25 doping.

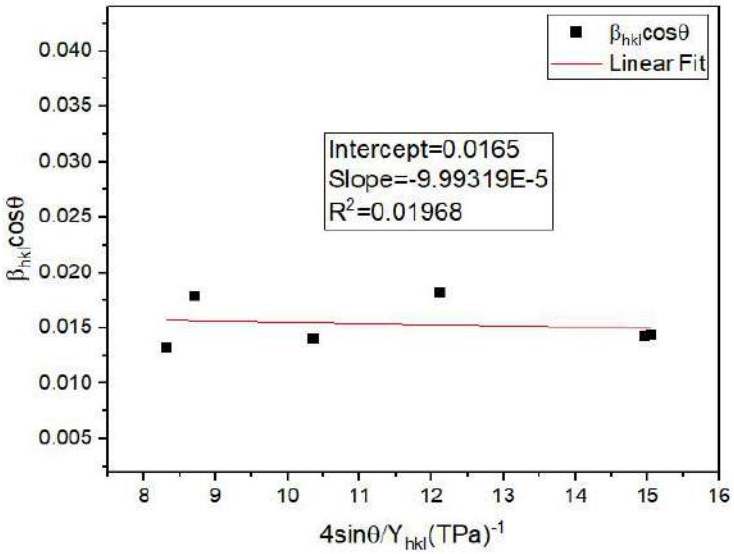

Fig. 5.60 Plot of $\beta_{hkl}\cos\theta$ versus (4Sinθ/Yhkl) for ZnO NPs with .3% P25 doping.

Different crystallite parameters obtained from USDM is shown in **Table 5.17**

Table 5.17 Values of crystallite size (D), lattice strain (ε) & stress (σ) of ZnO NPs with and without NP25 doping obtained by USDM.

TiO_2 P(25) doping (%)	**Crystallite Size(nm)**	**Lattice Strain(ε)×(10^{15})**	**Stress (σ)**
0	11.59	0.14	1.8589×10^{-4}
.1	6.52	0.24	3.282×10^{-4}
.2	8.24	0.46	6.085×10^{-5}
.3	8.4	0.76	9.993×10^{-5}

5.7.3 Uniform Deformation Energy Density Model (UDEDM)

From chapter 4, we know that the UDEDM equation can be written as

$$\beta_{hkl}\cos\theta_{hkl} = \left(\frac{K\lambda}{D}\right) + \left(4\sin\theta_{hkl}\left(\frac{2\mu_{ed}}{Y_{hkl}}\right)^{\frac{1}{2}}\right) \quad (5.17)$$

This equation is identical to straight line equation which represents the uniform deformation energy density model (UDEDM) equation [55]. From this model, energy density value of the crystals can be calculated as per equation (5.17). Plot of this equation (5.17), with the term $(4\sin\theta_{hkl}(\frac{2}{Y_{hkl}})^{\frac{1}{2}}$ along X-axis and $\mathscr{B}_{hkl}.\cos\theta_{hkl}$ along Y-axis corresponding to each diffraction peak for ZnO nanoparticles, the intercept of the plotted straight line provides the average size, whereas the slope gives the energy density value. The value of $\beta_{hkl}\cos\theta$ and $4\sin\theta_{hkl}(\frac{2}{Y_{hkl}})^{\frac{1}{2}}$ for each diffraction peak for ZnO nanoparticles is shown in **Table 5.18, Table 5.19, Table 5.20 and Table 5.21.**

Table 5.18 Values for UDEDM plot for ZnO NPs without doping

Peak	**β_{hkl}(rad.)**	**θ**	**4sinθ**	**$\beta_{hkl}\cos\theta$**	Y_{hkl}GPa (10^9)	$4\sin\theta(2/Y_{hkl})^{1/2}(10^{-6})$
100	0.009875	15.9198	1.09718	0.009496	127.25	4.3495
002	0.008684	17.2996	1.18947	0.008291	144.15	4.4315
101	0.016277	18.2016	1.24944	0.015462	121.43	5.0710
102	0.008473	23.8964	1.62034	0.007748	133.52	6.2714
110	0.009056	28.4026	1.90266	0.007966	127.26	7.5428
103	0.011581	31.5229	2.09136	0.009872	138.59	7.9448

Table 5.19 Values for UDEDM plot ZnO with .3% P25 doping

Peak	**β_{hkl}(rad.)**	**θ**	**4sinθ**	**β_{hkl}cosθ**	Y_{hkl}GPa (10^9)	4sinθ(2/ Y_{hkl})$^{1/2}$(10^{-6})
100	0.01863	16.07785	1.10778	0.01790	127.26	4.39116
002	0.01392	17.42481	1.19782	0.01327	144.09	4.4626
101	0.01482	18.32292	1.25749	0.01407	121.43	5.1037
102	0.01989	23.87711	1.61911	0.01817	133.52	6.2667
110	0.01623	28.44958	1.90554	0.01427	127.26	7.5542
103	0.01687	31.44800	2.08689	0.01439	138.59	7.9278

Table 5.20 Values for UDEDM plot ZnO with .2% P25 doping

Peak	**β_{hkl}(rad.)**	**θ**	**4sinθ**	**β_{hkl}cosθ**	Y_{hkl}GPa (10^9)	4sinθ(2/ Y_{hkl})$^{1/2}$(10^{-6})
100	0.0195346	15.852289	1.0928633	0.0187917	127.26	4.3316
002	0.016628	17.20275	1.183015	0.015884	144.09	4.4074
101	0.017631	18.100767	1.242756	0.016759	121.43	5.0439
102	0.020596	23.95037	1.6237806	0.0188226	133.52	6.2848
110	0.018612	28.370069	1.900658	0.0163767	127.26	7.5349
103	0.0216075	31.525449	2.0915089	0.0184184	138.59	7.9454

Table 5.21 Values for USDM plot ZnO with .1% P25 doping

Peak	**β_{hkl}(rad.)**	**θ**	**4sinθ**	**β_{hkl}cosθ**	Y_{hkl}GPa (10^9)	4sinθ(2/ Y_{hkl})$^{1/2}$(10^{-6})
100	0.0191272	15.924047	1.09745	0.018393	127.26	4.3507
002	0.0188305	17.09928	1.18278	0.0179883	144.09	4.4066
101	0.017765	18.175404	1.247708	0.016877	121.43	5.0640
102	0.0188760	23.948794	1.62368	0.017250	133.52	6.2844
110	0.0166050	28.374289	1.90091	0.014610	127.26	7.5359
103	0.0193178	31.3008	2.07812	0.0165061	138.59	7.8945

Now, by placing $4Sin\theta(2/Yhkl)^{1/2}$values along the x-axis and ($\beta hkl.Cos\theta$) values along y-axis **Fig. 5.61, Fig. 5.62, Fig. 5.63, & Fig. 5.64** is drawn. From these figures, y-intercept and slope are obtained to determine the parameters crystallite size (D), strain (ε) stress (σ) and energy density (u). Equations for determining these parameters are:

$$D = \frac{K\lambda\Gamma}{y-intercept} \tag{5.18}$$

$$\mu_{ed} = (slope)^2 \tag{5.19}$$

$$\sigma = \sqrt{2\mu_{ed}Y_{hkl}} \tag{5.20}$$

$$\varepsilon = \frac{\sigma}{Y_{hkl}} \tag{5.21}$$

Different crystallite parameters obtained from UDEDM is shown in **Table 5.22.**

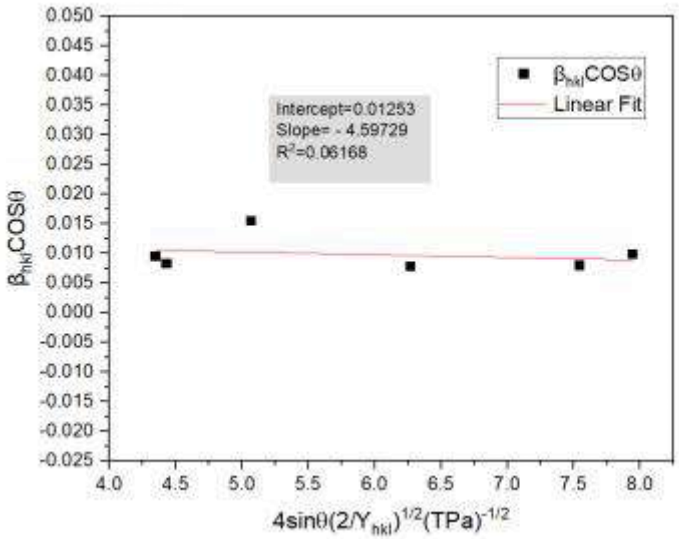

Fig. 5.61 Plot of $\beta_{hkl}\cos\theta$ versus $4Sin\theta(2/Y_{hkl})^{1/2}$ for ZnO NPs withot doping.

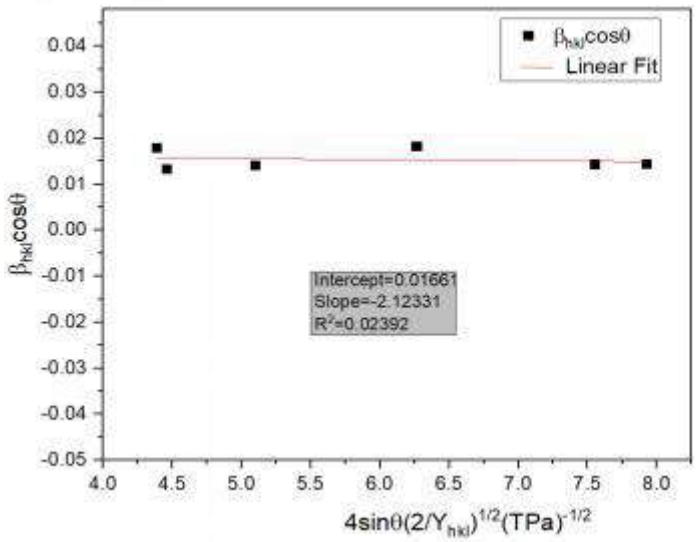

Fig. 5.62 Plot of $\beta_{hkl}\cos\theta$ versus $4Sin\theta(2/Y_{hkl})^{1/2}$for ZnO NPs with 0.3% P25 doping.

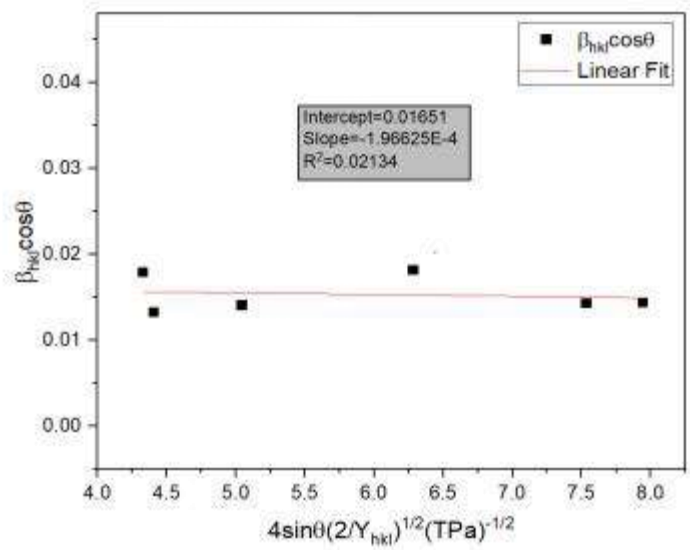

Fig. 5.63 Plot of $\beta_{hkl}\cos\theta$ versus $4\sin\theta(2/Y_{hkl})^{1/2}$for ZnO NPs with 0.2% P25 doping.

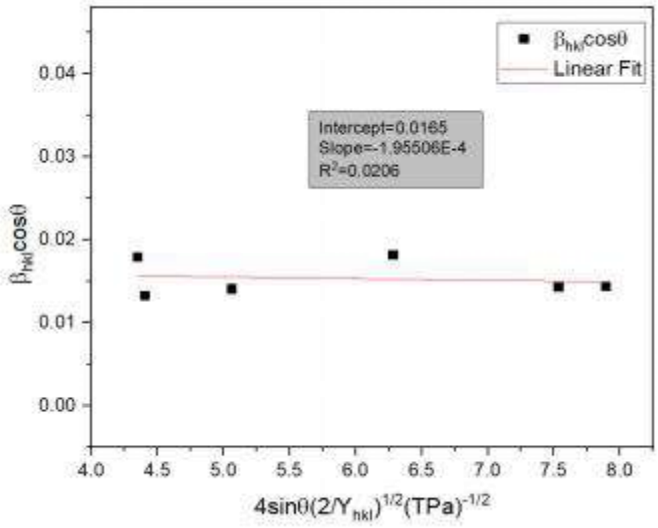

Fig. 5.64 Plot of $\beta_{hkl}\cos\theta$ versus $4\sin\theta(2/Y_{hkl})^{1/2}$for ZnO NPs with 0.1% P25 doping.

Table 5.22 Values of crystallite size (D), lattice strain (ε) stress (σ) & energy density (u) of ZnO NPs with and without P25 doping obtained by UDEDM.

TiO_2 P(25) %	**Crystallite Size(nm)**	**Lattice Strain(10^{-15})**	**Stress (σ)**	**Energy density (u) (Jm^{-3})**
0	11.06	29.88	3950	21.13
.1	0.8	6.37	842	3.8×10^{-08}
.2	0.8	5.46	722	3.8×10^{-08}
.3	0.81	5.40	714	4.51

5.8 Size-Strain Plot (SSP) Method

The Size-Strain Plot (SSP) equation can be written as

$$(d_{hkl}\beta_{hkl}\cos\theta_{hkl})^2 = \frac{K\lambda}{D}(d^2{}_{hkl}\beta_{hkl}\cos\theta_{hkl}) + (\frac{\varepsilon}{2})^2 \quad (5.22)$$

Where dhkl is the lattice distance between the <h k l> planes and for the hexagonal crystal structure,

$$d_{hkl} = \frac{a}{[\sqrt{4/3(h^2+k^2+hk+\left(\frac{al}{c}\right)^2}]} \quad (5.23)$$

K is a constant that depends on the shape of the particles.

Table 5.23 Values for SSP plot for ZnO NPs without doping

Peak	**β_{hkl}(rad.)**	**$\beta_{hkl}\cos\theta$**	**$d_{hkl}(10^{-10})$**	**$d_{hkl}^2(10^{-20})$**	**$d_{hkl}^2\beta_{hkl}\cos\theta$ (10^{-20})**	**$(d_{hkl}\beta_{hkl}\cos\theta)^2$**
100	0.009875	0.009496	2.7987	7.82768	0.0743379	0.0070597
002	0.008684	0.008291	2.5818	6.6656	0.055266	0.0004580
101	0.016277	0.015462	2.4599	6.0512	0.0935636	0.001446
102	0.008473	0.007748	1.8974	3.6000	0.0278928	0.002161
110	0.009056	0.007966	1.6153	2.6092	0.0207848	0.0001655
103	0.011581	0.009872	1.4660	2.1491	0.0212159	0.0002094

Table 5.24 Values for UDEDM plot ZnO with .3% P25 doping

Peak	**β_{hkl}(rad.)**	**$\beta_{hkl}\cos\theta$**	**$d_{hkl}(10^{-10})$**	**$d_{hkl}^2(10^{-20})$**	**$d_{hkl}^2\beta_{hkl}\cos\theta$ (10^{-20})**	**$(d_{hkl}\beta_{hkl}\cos\theta)^2$**
100	0.009875	0.009496	2.7987	7.82768	0.0140145	0.002509
002	0.008684	0.008291	2.5818	6.6656	0.0884991	0.00117378
101	0.016277	0.015462	2.4599	6.0512	0.0851410	0.00119792
102	0.008473	0.007748	1.8974	3.6000	0.0654624	0.001190419
110	0.009056	0.007966	1.6153	2.6092	0.03724293	0.000531317
103	0.011581	0.009872	1.4660	2.1491	0.0309255	0.000445030

Table 5.25 Values for UDEDM plot ZnO with .2% P25 doping

Peak	β_{hk}(rad.)	$\beta_{hkl}\cos\theta$	$d_{hkl}(10^{-10})$	$d_{hkl}^2(10^{-20})$	$d_{hkl}^2\beta_{hkl}\cos\theta$ (10^{-20})	$(d_{hkl}\beta_{hkl}\cos\theta)^2$
100	0.009875	0.009496	2.7987	7.82768	0.014095	0.00276417
002	0.008684	0.008291	2.5818	6.6656	0.1058763	0.00168091
101	0.016277	0.015462	2.4599	6.0512	0.10141206	0.00169953
102	0.008473	0.007748	1.8974	3.6000	0.0677613	0.0012754
110	0.009056	0.007966	1.6153	2.6092	0.0427126	0.00069977
103	0.011581	0.009872	1.4660	2.1491	0.03958298	0.00072907

Table 5.26 Values for USDM plot ZnO with .1% P25 doping

Peak	β_{hkl}(rad.)	$\beta_{hkl}\cos\theta$	$d_{hkl}(10^{-10})$	$d_{hkl}^2(10^{-20})$	$d_{hkl}^2\beta_{hkl}\cos\theta$ (10^{-20})	$(d_{hkl}\beta_{hkl}\cos\theta)^2$
100	0.009875	0.009496	2.7987	7.82768	0.143974	0.0026481
002	0.008684	0.008291	2.5818	6.6656	0.119847	0.0021585
101	0.016277	0.015462	2.4599	6.0512	0.102126	0.0017235
102	0.008473	0.007748	1.8974	3.6000	0.0621	0.00107137
110	0.009056	0.007966	1.6153	2.6092	0.038120	0.00055693
103	0.011581	0.009872	1.4660	2.1491	0.035473	0.00058554

Table 5.23, Table 5.24, Table 5.25 &**Table 5.26** shows the values of $d_{hkl}^2\beta_{hkl}\cos\theta$ & $(d_{hkl}\beta_{hkl}\cos\theta)^2$ for each diffraction peaks of ZnO NPs with 0%, 0.7%, 1%, 2% P25 doping respectively. Now, by placing $d_{hkl}^2\beta_{hkl}\cos\theta$values along the x-axis and $(d_{hkl}\beta_{hkl}\cos\theta)^2$ values along y-axis **Fig. 5.65, Fig. 5.66, Fig. 5.67, & Fig. 5.68** is drawn. From these figures, y-intercept and slope are obtained to determine the parameters crystallite size (D), & strain (ε). Equations for determining these parameters are:

$$\frac{K\lambda}{D} = Slope \tag{5.24}$$

$$(\frac{\varepsilon}{2})^2 = y - intercept \tag{5.25}$$

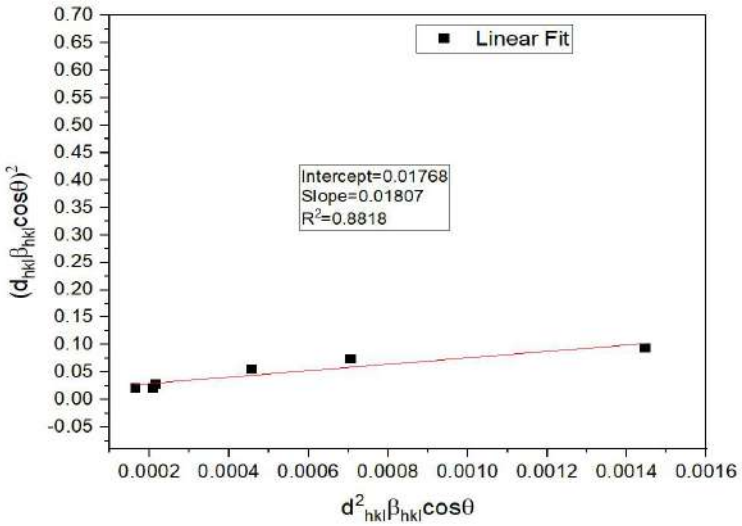

Fig. 5.65 Plot of $(d_{hkl}\beta_{hkl}\cos\theta)^2$ versus $d_{hkl}^2\beta_{hkl}\cos\theta$ for ZnO NPs without doping.

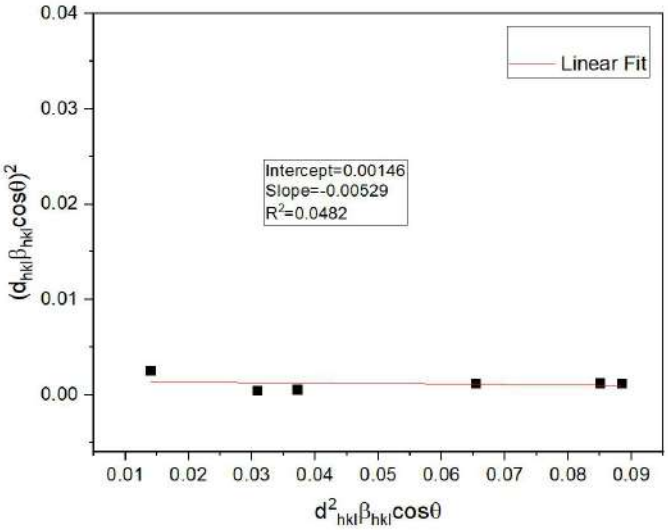

Fig. 5.66 Plot of $(d_{hkl}\beta_{hkl}\cos\theta)^2$ versus $d_{hkl}^2\beta_{hkl}\cos\theta$ for ZnO NPs with 0.3% P25 doping.

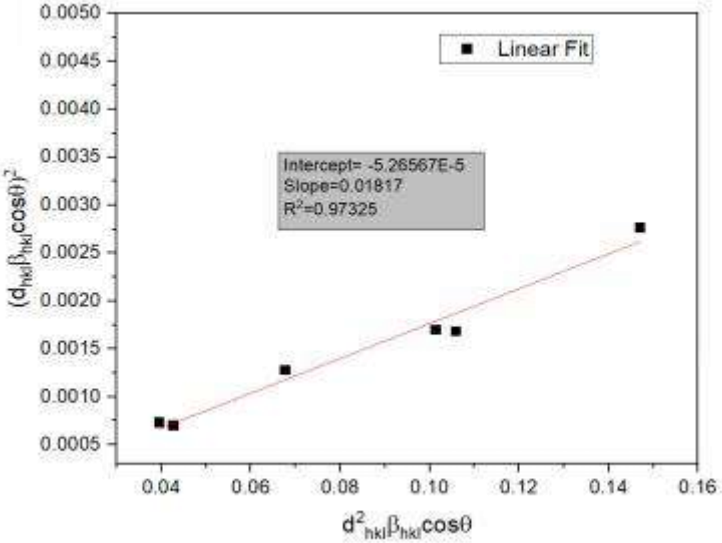

Fig. 5.67 Plot of $(d_{hkl}\beta_{hkl}\cos\theta)^2$ versus $d_{hkl}^2\beta_{hkl}\cos\theta$ for ZnO NPs with 0.2% P25 doping.

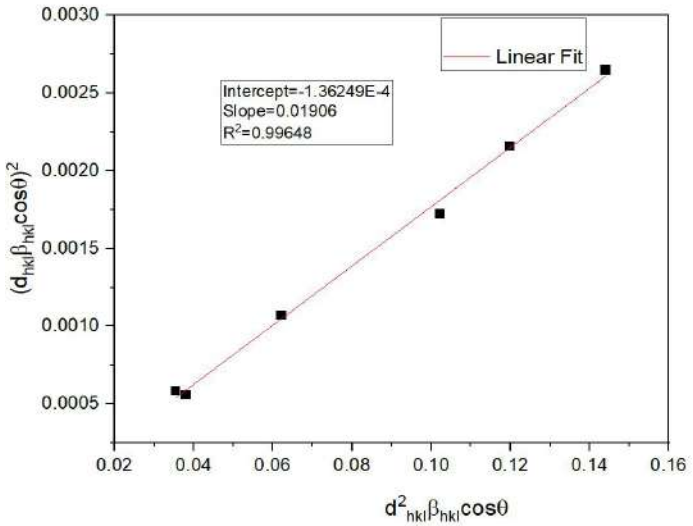

Fig. 5.68 Plot of $(d_{hkl}\beta_{hkl}\cos\theta)^2$ versus $d_{hkl}^2\beta_{hkl}\cos\theta$ for ZnO NPs with 0.1% P25 doping.

Crystallite size & lattice strain obtained using equations (5.24) & (5.25) is shown in **Table 5.27.**

Table 5.27 Values of crystallite size (D) & lattice strain of ZnO NPs with and without P25 doping obtained by SSP method.

TiO_2 P25 (%)	**Crystallite Size (nm)**	**Lattice Strain(ε)($\times10^{-3}$)**
0	7.5	265.9
.3	25.5	76.41
.2	7.4	14.5
.1	7.08	23.3

5.9 Halder-Wagner Method

In Halder-Wagner method, describes the crystallite size and lattice strain profiles with the Lorentzian and the Gaussian function, respectively. Consequently, we have

$$\frac{\beta^*_{hkl}}{d^*_{hkl}} = \frac{1}{D}.\left(\beta^*_{hkl}/{d^*_{hkl}}^2\right) + \left(\frac{\varepsilon}{2}\right)^2 \qquad (5.26)$$

Where β*hkl= βhkl.cosθ/λ and d*hkl= 2dhkl.sinθ/λ.

Equation (5.26) is used to determine the crystallite size, and the lattice strain.

Table 5.28 Values for H-W method for ZnO NPs without doping

Peak	$\beta_{hkl}\cos\theta$	β_{hkl}^{*}	$d_{hkl}(10^{-10})$	$d_{hkl}^{*}(10^{-10})$	$(\beta_{hkl}^{*}/d_{hkl}^{*})^2$ (10^{20})	β_{hkl}/d_{hkl} (10^{20})
100	0.009496	0.61667	2.7987	9.96642	0.0000382	0.0006208
002	0.008291	0.05383	2.5818	9.970717	0.0000291	0.0005414
101	0.015462	0.10040	2.4599	9.97893	0.000101	0.001008
102	0.007748	0.050311	1.8974	9.98189	0.0000254	0.000504
110	0.007966	0.051727	1.6153	9.97847	0.0000268	0.0005195
103	0.009872	0.064104	1.4660	9.954317	0.0000414	0.0006469

Table 5.29 Values for H-W method for ZnO NPs with .3% P25 doping

Peak	$\beta_{hkl}\cos\theta$	β_{hkl}^{*}	$d_{hkl}(10^{-10})$	$d_{hkl}^{*}(10^{-10})$	$(\beta_{hkl}^{*}/d_{hkl}^{*})^2$ (10^{20})	β_{hkl}/d_{hkl2} (10^{20})
100	0.009496	0.11626	2.7987	10.0627	0.0001334	0.001148
002	0.008291	0.08621	2.5818	10.0406	0.0000737	0.0008551
101	0.015462	0.09136	2.4599	10.0431	0.0000827	0.0009057
102	0.007748	0.11807	1.8974	9.9743	0.0001401	0.001186
110	0.007966	0.09268	1.6153	9.9935	0.00008600	0.0009280
103	0.009872	0.09344	1.4660	9.9330	0.00008849	0.0009470

Table 5.30 Values for H-W method for ZnO NPs with .2% P25 doping

Peak	$\beta_{hkl}\cos\theta$	β_{hkl}^{*}	$d_{hkl}(10^{-10})$	$d_{hkl}^{*}(10^{-10})$	$(\beta_{hkl}^{*}/d_{hkl}^{*})^2$ (10^{20})	β_{hkl}/d_{hkl2} (10^{20})
100	0.009496	0.122012	2.7987	9.9251	0.0001511	0.001238
002	0.008291	0.103142	2.5818	9.9165	0.0001081	0.001048
101	0.015462	0.10882	2.4599	9.9254	0.0001202	0.001104
102	0.007748	0.12222	1.8974	10.0030	0.0001492	0.001221
110	0.007966	0.106342	1.6153	9.9679	0.0001138	0.001070
103	0.009872	0.1196	1.4660	9.9550	0.0001443	0.001206

Table 5.31 Values for H-W method for ZnO NPs with .1% P25 doping

Peak	$\beta_{hkl}\cos\theta$	β_{hkl}^*	$d_{hkl}(10^{-10})$	$d_{hkl}^*(10^{-10})$	$(\beta_{hkl}^*/d_{hkl}^*)^2$ (10^{20})	β_{hkl}/d_{hkl2} (10^{20})
100	0.009496	0.119435	2.7987	9.9689	0.0001435	0.001201
002	0.008291	0.116807	2.5818	9.9184	0.0001386	0.001187
101	0.015462	0.10959	2.4599	9.9650	0.0001209	0.001103
102	0.007748	0.11201	1.8974	10.0029	0.0001253	0.001119
110	0.007966	0.09487	1.6153	9.9692	0.0000905	0.0009545
103	0.009872	0.10718	1.4660	9.8913	0.0001174	0.001095

Table 5.28, Table 5.29, Table 5.30 &**Table 5.31** shows the values of (β^*hkl/d^*hkl^2) & $(\beta^*hkl/\ d^*hkl)^2$for each diffraction peaks of ZnO NPs with 0%, 0.3%, 0.2%, 0.1% P25 doping respectively. Now, by placing (β^*hkl/d^*hkl^2) values along the x-axis and $(\beta^*hkl/\ d^*hkl)^2$values along y-axis **Fig. 5.69, Fig. 5.70, Fig. 5.72, & Fig. 5.73** is drawn. From these figures, slope and y-intercept are obtained to determine the parameters crystallite size (D) & strain (ε). Equations for determining these parameters are:

$$D = \frac{1}{Slope} \tag{5.27}$$

$$\varepsilon = 2\sqrt{y - intercept} \tag{5.28}$$

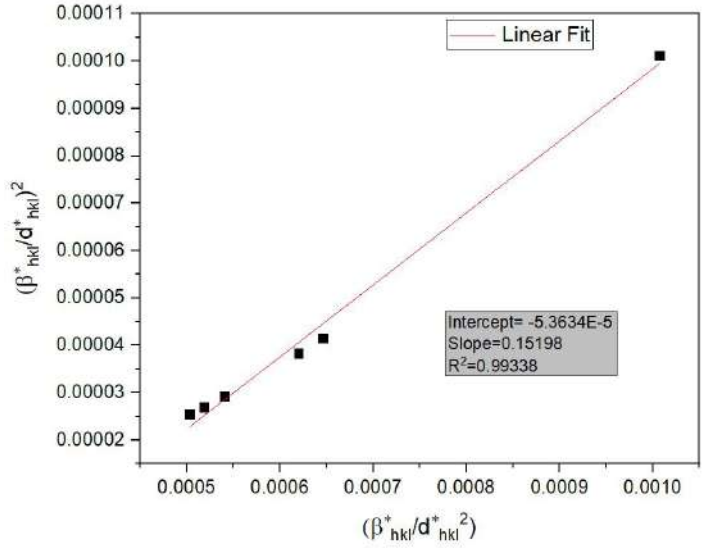

Fig. 5.69 Plot of $(\beta^*hkl/\ d^*hkl)^2$versus (β^*hkl/d^*hkl^2) for ZnO NPs without doping.

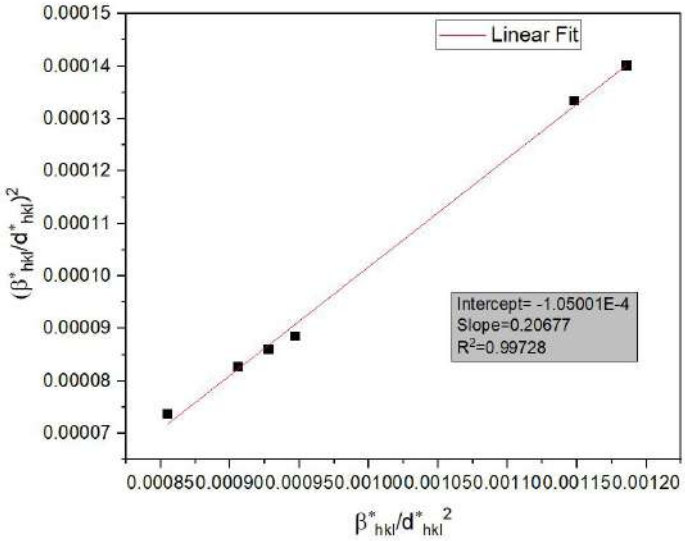

Fig. 5.70 Plot of $(\beta^*_{hkl}/ d^*_{hkl})^2$versus $(\beta^*_{hkl}/d^*_{hkl}{}^2)$ for ZnO NPs with 0.3% P25 doping.

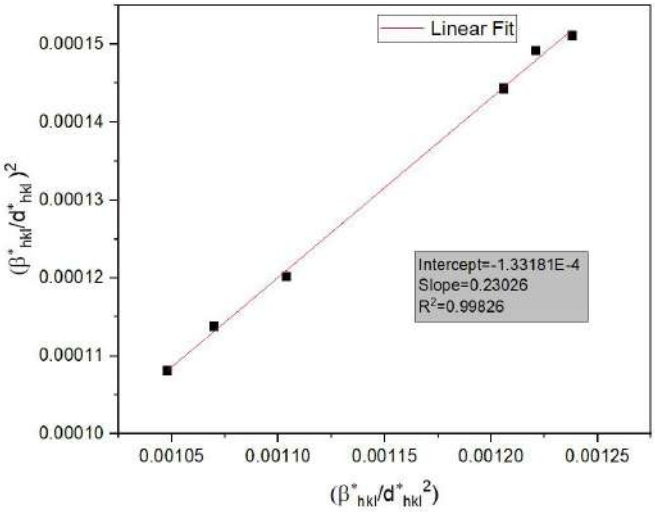

Fig. 5.71 Plot of $(\beta^*_{hkl}/ d^*_{hkl})^2$versus $(\beta^*_{hkl}/d^*_{hkl}{}^2)$ for ZnO NPs with 0.2% P25 doping.

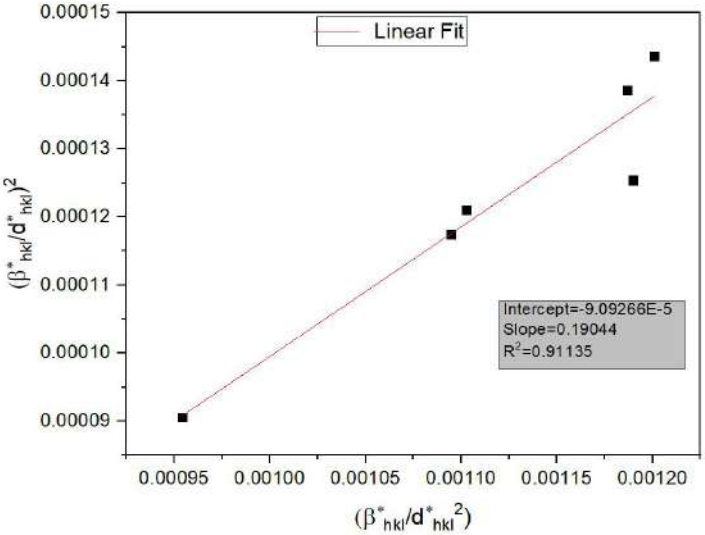

Fig. 5.72 Plot of $(\beta^*hkl/ d^*hkl)^2$versus (β^*hkl/d^*hkl^2) for ZnO NPs with 0.1% P25 doping.

Table 5.32 shows the results obtained from equations (5.27) & (5.28).

Table 5.32 Values of crystallite size (D) & lattice strain of ZnO NPs with and without P25 doping obtained by H-W method.

P25 %	Crystallite Size (nm)	Lattice Strain (ε) ($\times 10^{-3}$)
0	6.58	14.6
.3	4.84	20.5
.2	4.34	23.08
.1	5.25	19.07

5.10 Wagner-Agua Method

Wagner and Agua offered an analytical technique which is applied to determine the values of crystallite size and lattice strain from following equation:

$$(\beta_{hkl}\cos\theta_{hkl})^2 = (4\varepsilon_{WA}\sin\theta_{hkl})^2 + (\frac{K\lambda}{D_{WA}})^2 \quad (5.29)$$

Where is the Wagner-Agua crystallite size and is the Wagner-Agua lattice strain. **Table 5.28, Table 5.29, Table 5.30** &**Table 5.31** shows the values of $(\beta^*_{hkl}/d^*_{hkl}{}^2)$ & $(\beta^*_{hkl}/d^*_{hkl})^2$ for each diffraction peaks of ZnO NPs with 0%, 0.1%, 0.2%, 0.3% P25 doping respectively.

Table 5.33 Values for Wagner-Agua method for ZnO NPs without doping

Peak	**β_{hkl}(rad.)**	**cosθ**	**4sinθ**	**$\beta_{hkl}\cos\theta$**	**$(\beta_{hkl}\cos\theta)^2$**	**$(4\sin\theta)^2$**
100	0.0195346	0.961969	1.0928633	0.0187917	0.000088	1.2036437
002	0.016628	0.95526	1.183015	0.015884	0.000067	1.414838
101	0.017631	0.95051	1.242756	0.016759	0.000237	1.5611003
102	0.020596	0.913897	1.6237806	0.0188226	0.000059	1.653297
110	0.018612	0.879896	1.900658	0.0163767	0.0000624	3.620115
103	0.0216075	0.852408	2.0915089	0.0184184	0.0000960	4.37378

Table 5.34 Values for Wagner-Agua method for ZnO NPs with 0.3% P25 doping

Peak	β_{hkl}(rad.)	cosθ	4sinθ	β_{hkl}cosθ	$(\beta_{hkl}\cos\theta)^2$	$(4\sin\theta)^2$
100	0.0195346	0.961969	1.0928633	0.0187917	0.0003200	1.22699
002	0.016628	0.95526	1.183015	0.015884	0.0001760	1.43472
101	0.017631	0.95051	1.242756	0.016759	0.0001979	1.581054
102	0.020596	0.913897	1.6237806	0.0188226	0.000330	2.62148
110	0.018612	0.879896	1.900658	0.0163767	0.000203	3.63093
103	0.0216075	0.852408	2.0915089	0.0184184	0.000207	4.35473

Table 5.35 Values for Wagner-Agua method for ZnO NPs with 0.2% P25 doping

Peak	β_{hkl}(rad.)	cosθ	4sinθ	β_{hkl}cosθ	$(\beta_{hkl}\cos\theta)^2$	$(4\sin\theta)^2$
100	0.0195346	0.961969	1.0928633	0.0187917	0.000349	1.193774
002	0.016628	0.95526	1.183015	0.015884	0.000249	1.399489
101	0.017631	0.95051	1.242756	0.016759	0.000278	1.544303
102	0.020596	0.913897	1.6237806	0.0188226	0.000353	2.636401
110	0.018612	0.879896	1.900658	0.0163767	0.000265	3.612280
103	0.0216075	0.852408	2.0915089	0.0184184	0.000338	4.37437

Table 5.36 Values for Wagner-Agua method for ZnO NPs with 0.1% P25 doping

Peak	β_{hkl}(rad.)	cosθ	4sinθ	β_{hkl}cosθ	$(\beta_{hkl}\cos\theta)^2$	$(4\sin\theta)^2$
100	0.0195346	0.961969	1.0928633	0.0187917	0.0000335	1.204286
002	0.016628	0.95526	1.183015	0.015884	0.0003204	1.39877
101	0.017631	0.95051	1.242756	0.016759	0.0002822	1.55675
102	0.020596	0.913897	1.6237806	0.0188226	0.000295	2.63607
110	0.018612	0.879896	1.900658	0.0163767	0.000213	3.613420
103	0.0216075	0.852408	2.0915089	0.0184184	0.000272	4.318499

Now, by placing (4sinθ)2values along the x-axis and $(\beta_{hkl}\cos\theta)^2$values along y-axis **Fig. 5.72, Fig. 5.73, Fig. 5.74, & Fig. 5.74** is drawn. From these Wagner-Agua plots, y-intercept and slope are obtained to determine the parameters crystallite size (Dwa) & strain (εwa). The intercept of the plotted straight line gives the crystallite size and the slope provides the intrinsic strain. Equations for determining these parameters are:

$$D_{WA=\frac{1}{\sqrt{y-intercept}}.K\lambda} \quad (5.30)$$

$$\varepsilon_{WA} = \sqrt{Slope} \quad (5.31)$$

.

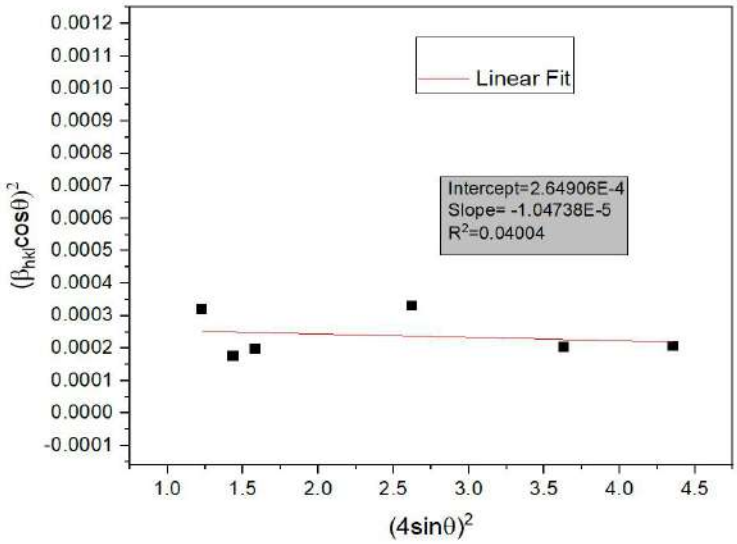

Fig. 5.73 Plot of $(\beta_{hkl}\cos\theta)^2$versus $(4\sin\theta)^2$for ZnO NPs with 0.3% P25 doping.

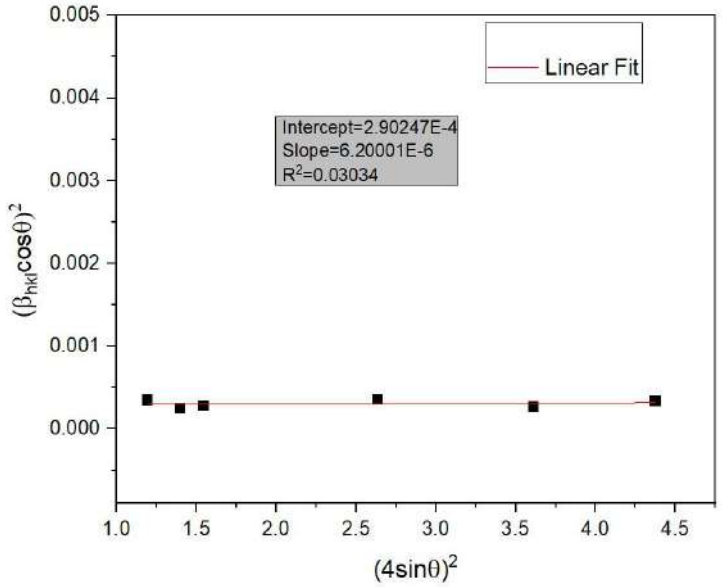

Fig. 5.74 Plot of $(\beta_{hkl}\cos\theta)^2$versus $(4\sin\theta)^2$for ZnO NPs with 0.2% P25 doping.

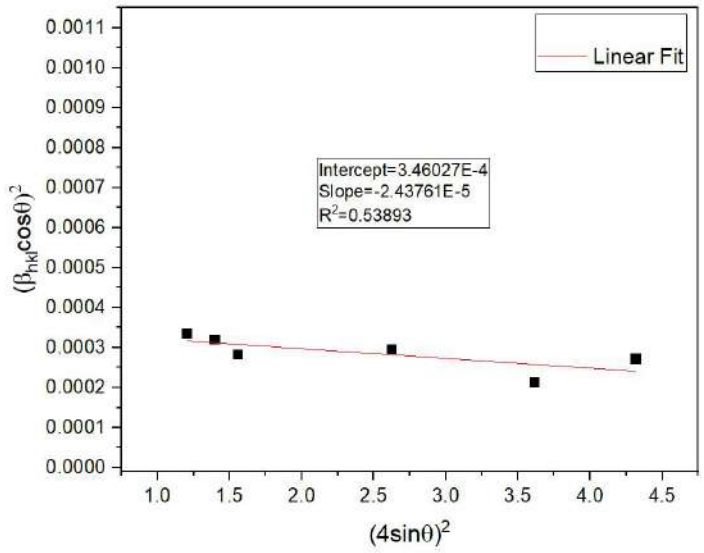

Fig. 5.75 Plot of $(\beta_{hkl}\cos\theta)^2$ versus $(4\sin\theta)^2$ for ZnO NPs with 0.1% P25 doping. Crystallite size & lattice strain obtained using equations (5.30) & (5.31) is shown in **Table 5.37.**

Table 5.37 Values of crystallite size (DWA) & lattice strain (εWA) of ZnO NPs with and without P25 doping obtained by Wagner-Agua method.

P25 (%)	Crystallite Size (nm)	Lattice Strain (ε_{WA})($\times 10^{-3}$)
0	12.08	3.16
.3	8.2	3.23
.2	8	2.48
.1	7.3	4.93

5.11 Summarization of Results

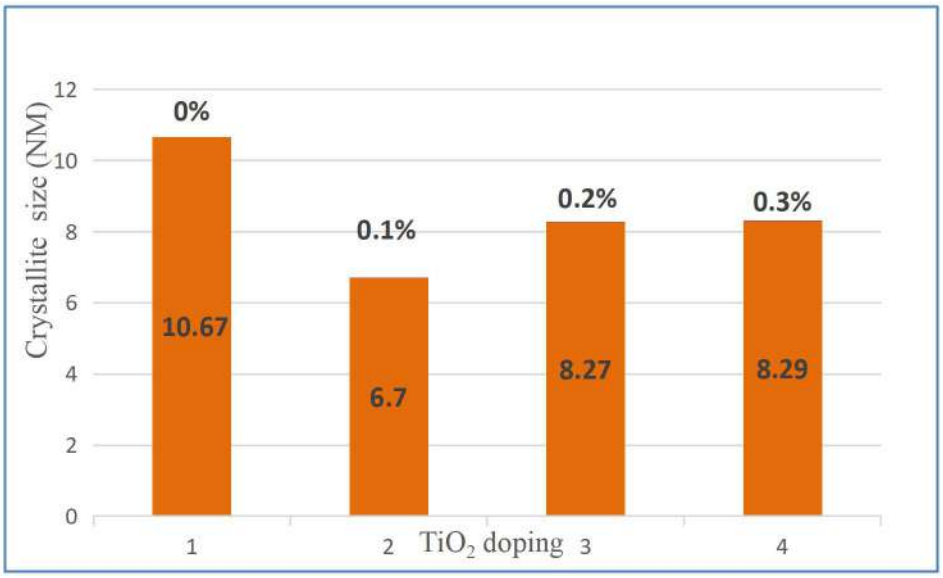

Fig. 5.75 Variation of Crystallite size (D) of ZnO with and without TiO_2 [P25] doping obtained from UDM Of W-H method.

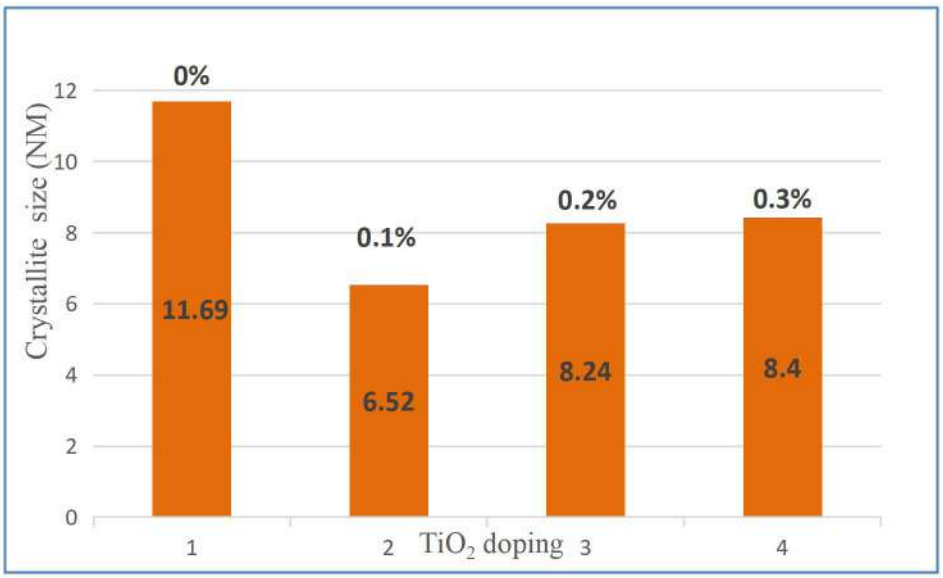

Fig. 5.76 Variation of Crystallite size (D) of ZnO with and without TiO_2 [P25] doping obtained from USDM Of W-H method.

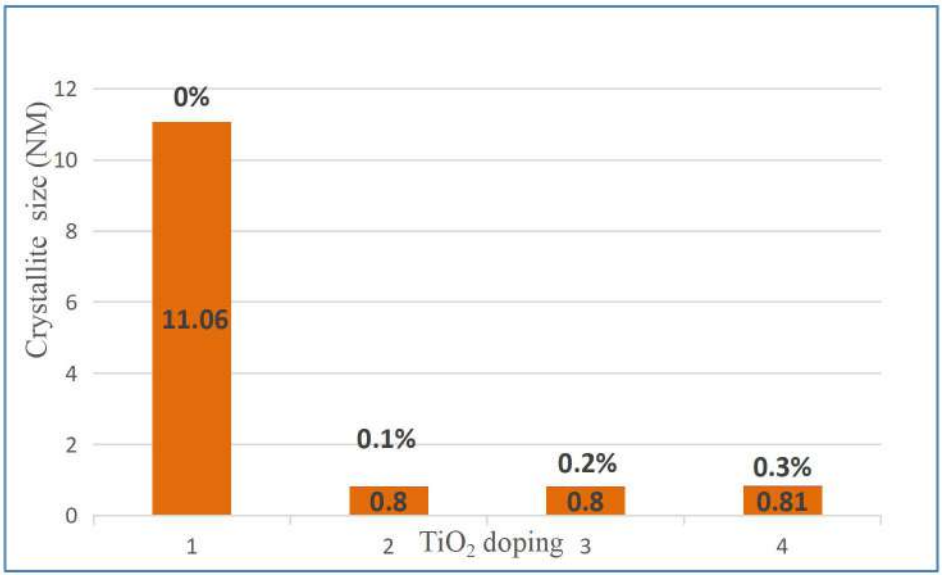

Fig. 5.77 Variation of Crystallite size (D) of ZnO with and without TiO_2 [P25] doping obtained from UDEDM Of W-H method.

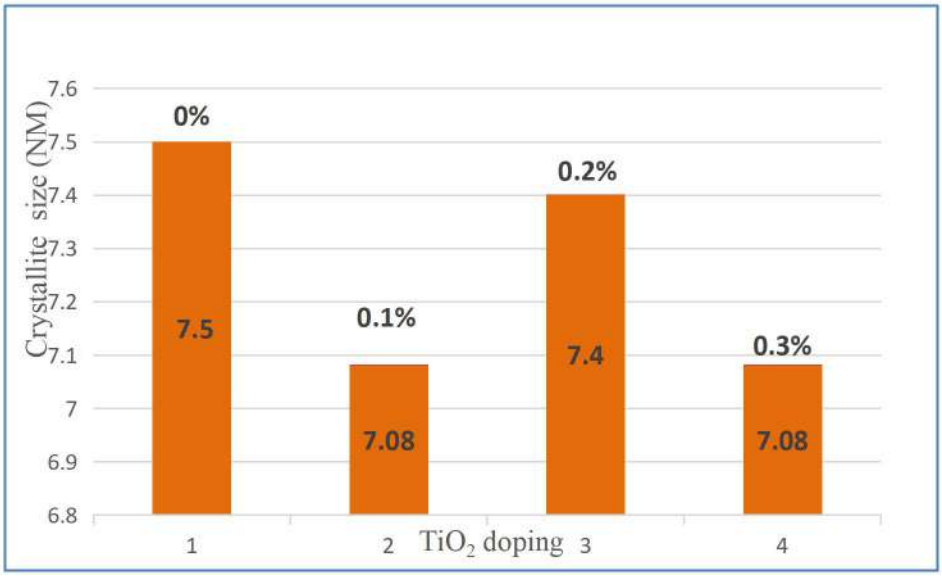

Fig. 5.78 Variation of Crystallite size (D) of ZnO with and without TiO_2 [P25] doping obtained from SSP method.

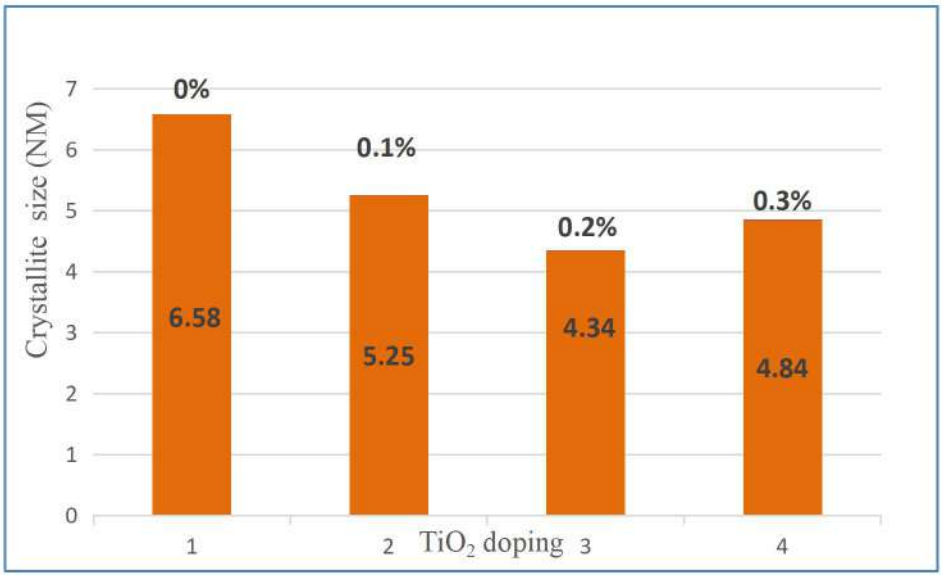

Fig. 5.79 Variation of Crystallite size (D) of ZnO with and without TiO_2 [P25] doping obtained from **H**alder-**w**agner method.

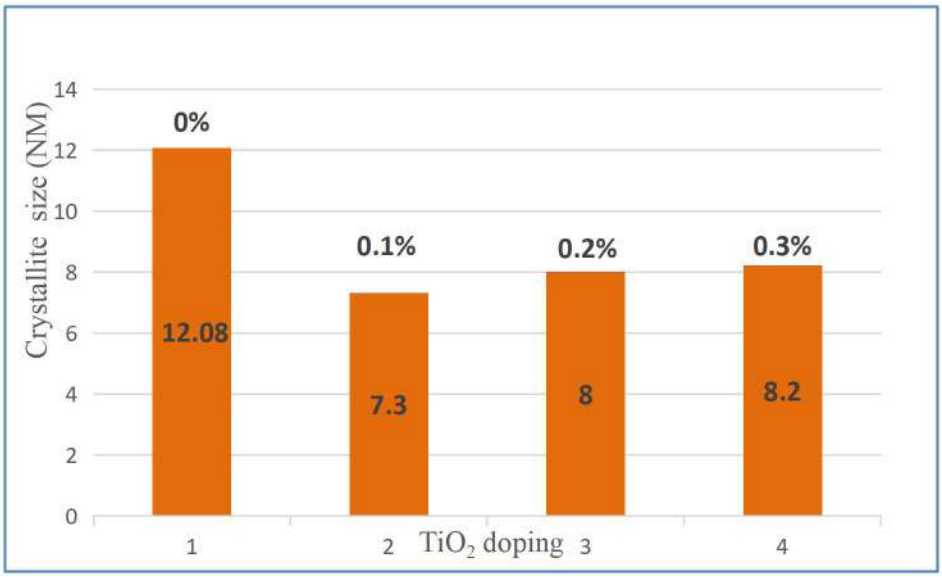

Fig. 5.80 Variation of Crystallite size (D) of ZnO with and without TiO_2 [P25] doping obtained from **W**agner-**A**gua method.

Variation of crystallite size (D) of ZnO without P(25) doping and with various concentration of P(25) doping is shown in **Fig. 5.75, Fig. 5.76, Fig. 77,Fig. 5.77, Fig. 5.78, Fig. 5.79, Fig. 5.80.** From all the methods its clear that the crystallite size (D) increases without doping. The size calculated with .1 % P(25) doping is slightly bigger than 0.2% doped and 0.3% doped.

Variation of crystallite size (D)obtained from six different methods for ZnO nanoparticles with 0%, 0.1%, 0.2% & 0.3% P(25)doping respectively. The average crystallite size (D) obtained from UDM, USDM, UDEDM, and W-A method are pretty similar, but the value of (D) obtained from SSP method are lower than the value obtained from the other methods.

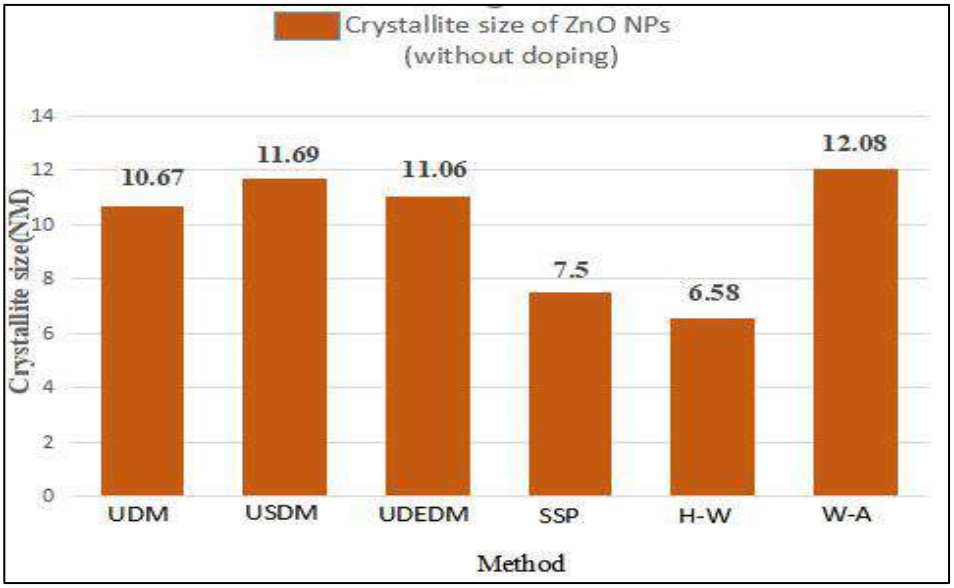

Fig. 5.81 Variation of crystallite size (D) of ZnO without doping obtained from six different methods.

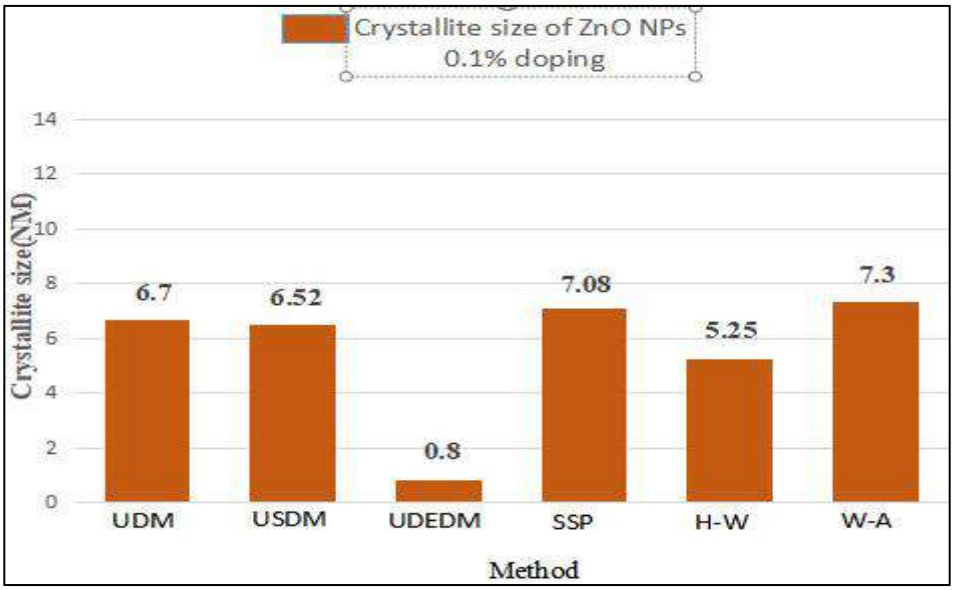

Fig. 5.82 Variation of crystallite size (D) of ZnO with 0.1% P25 type TiO_2 doping obtained from six different methods.

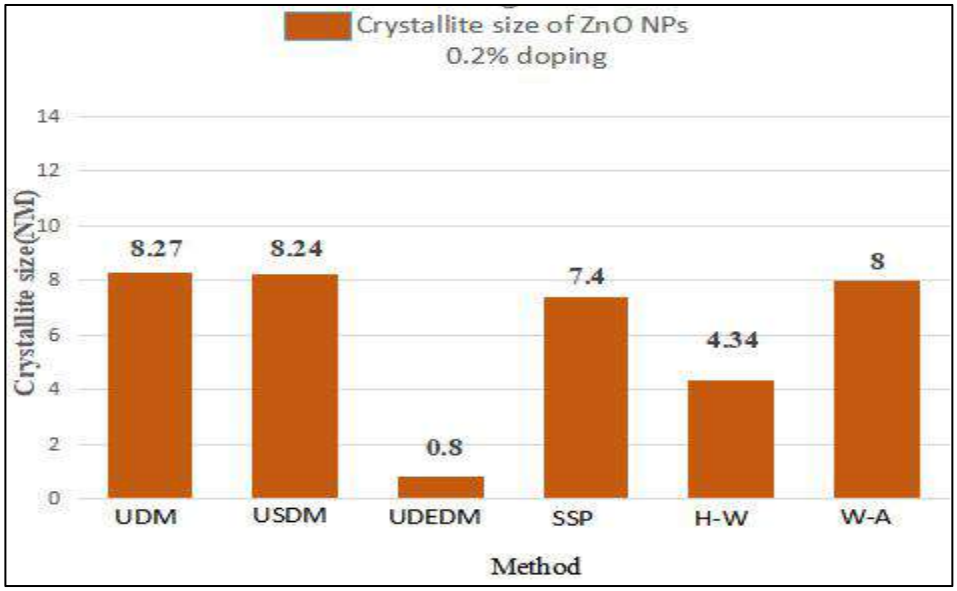

Fig. 5.83 Variation of crystallite size (D) of ZnO with 0.2% P25 type TiO_2 doping obtained from six different methods.

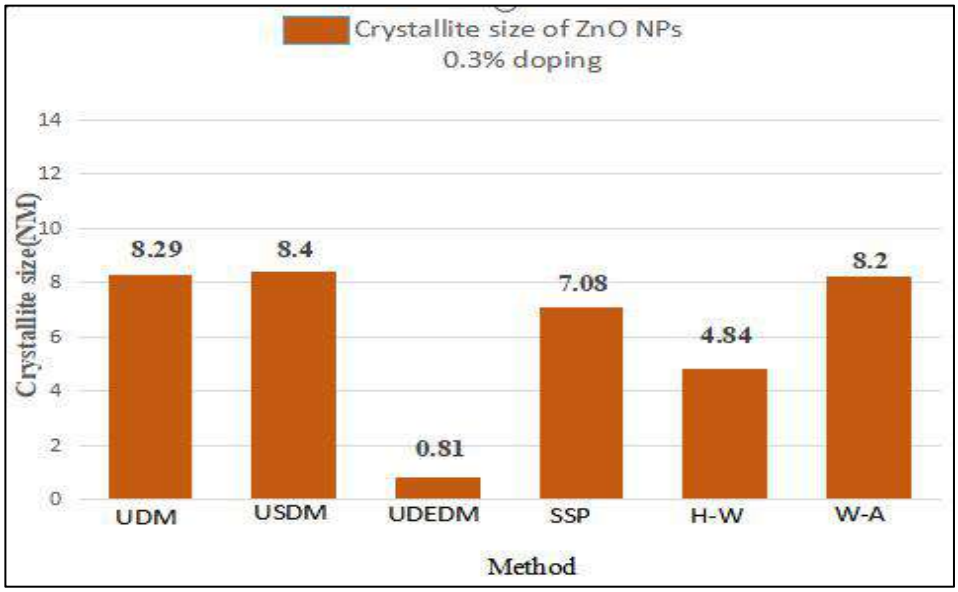

Fig. 5.84 Variation of crystallite size (D) of ZnO with 0.3% P25 TiO_2 doping obtained from six different methods.

Table 5.38 Geometrical parameters of ZnO nanoparticles using different methods

TiO2 [P25] doping (%)	Williamson and Hall Method						SSP Method	Halder-Wagner Methode	Wagner-Agua Method
	UDM	USDM		UDEDM					
	(ε) ($\times 10^{-3}$)	(ε) ($\times 10^{-15}$)	σ Pa	(ε) ($\times 10^{-10}$)	σ Pa	μ Jm^{-3}	(ε) ($\times 10^{-3}$)	(ε) ($\times 10^{-3}$)	(ε) ($\times 10^{-3}$)
0	2.09	0.14	1.8589×10^{-4}	29.88	3950	21.13	265.9	14.6	3.16
.3	8.84	0.76	9.993×10^{-5}	5.40	714	4.51	76.41	20.5	3.23
.2	5.05	0.46	6.085×10^{-5}	5.46	722	3.8×10^{-08}	14.5	23.08	2.48
.1	2.46	0.24	3.282×10^{-4}	6.37	842	3.8×10^{-08}	23.3	19.07	4.93

Table 5.38 shows the parameters of ZnO nanoparticles obtained from different Methods. The values of lattice strain (ε) calculated by W-H modified method are significantly lower than the value of SSP ,Halder-Wagner and Wagner-Agua Method. This increase in estimated strain value is actually due to the contribution of low and mid angle XRD data.Further,calculated higher value of strain, obtained in SSP method, may be attributed to the lattice dislocations [56], that plays a significant role in broadening of the reflection peaks at lower angles. Determining structural properties in analysis that used at high diffraction angle for significant accuracy result, and in SSP method that used at a low diffraction angle for better accuracy.

From all the methods crystallite size and lattice strain decreases with the increase of doping percentage concentration.Grain boundaries, strain, stresses, stacking faults, and coherency stress are the possible sources of the difference. Also,the photo electrode films were treated by hot-compression, which may generate few crystal disorders and in turn reduce the lattice strain. However, among all other methods, the SSP and W-A method is more accurate and favoured since points fit the linear line better than any other method.

CHAPTER 6

CONCLUSION

The ZnO nanoparticles films at different percentage of P(25) doping were prepared by employing Dr. blade coating method, that is inspected for crystallinity and structural properties using the X-ray Diffraction (XRD) technique. The construction of ZnO nanoparticles was a hexagonal wurtzite structure at both with and without doping conditions. XRD technique, Williamson-Hall models, Size-StrainPlot, Halder-Wagner Method and Wagner-Agua technique performed to calculate various properties of ZnO NPs, such as crystallite size, lattice strain, stress& energy density. The values of lattice strain (ε) calculated by W-H modified method are significantly lower than the value of SSP ,Halder-Wagner and Wagner-Agua Method. Determining structural properties in analysis that used at high diffraction angle for significant accuracy result, and in SSP method that used at a low diffraction angle for better accuracy. Crystallite size and lattice strain decreases with the increase of doping percentage concentration.Grain boundaries, strain, stresses, stacking faults, and coherency stress are the possible sources of the difference. The intensity of the diffraction peaks decrease greatly with the increase of doping concentration, indicating a loss of crystallinity because of lattice distortion.Among all the methods SSP, Wagner-Agua and Halder-Wagner method shows more accurate values as the point fit the linear line much better than other methods.

REFERENCES

[1] Md. Jahangir Alam, S. M. Ali Zaker Shawon, M. Sultana, Md. Wasikur Rahman and M. M. R. Khan, "Kinetic study of biodiesel production from soybean oil," 2014 POWER AND ENERGY SYSTEMS: TOWARDS SUSTAINABLE ENERGY, 2014, pp. 1-5.

[2] M. Hatamvand et al., "Recent advances in fiber-shaped and planar-shaped textile solar cells", *Nano Energy*, vol. 71, p. 104609, 2020.

[3] J. Ajayan, D. Nirmal, P. Mohankumar, M. Saravanan, M. Jagadesh and L. Arivazhagan, "A reviewof photovoltaic performance of organic/inorganic solar cells for future renewable and sustainable energy technologies", Superlattices and Microstructures, vol. 143, p. 106549, 2020. S. Hingorani, V. Pillai, P. Kumar, M. Multani and D. Shah, "Microemulsion mediated synthesis of zinc-oxide nanoparticles for varistor studies", Materials Research Bulletin, vol. 28, no. 12, pp. 1303-1310, 1993.

[4] Thanh, Nguyen TK, N. Maclean, and S. Mahiddine. "Mechanisms of nucleation and growth of nanoparticles in solution." Chemical reviews 114, no. 15 (2014): 7610-7630.

[5] Koczkur, Kallum M., Stefanos Mourdikoudis, Lakshminarayana Polavarapu, and Sara E. Skrabalak. "Polyvinylpyrrolidone (PVP) in nanoparticle synthesis." Dalton Transactions 44, no. 41 (2015): 17883-17905.

[6] Grégory Guisbiers, Sergio Mejía-Rosales, and Francis Leonard Deepak, ―Nanomaterial Properties: Size and Shape Dependencies‖, *Journal of Nanomaterials,* Vol. 2012, pp. 1-2, 2012.

[7] S. Sakohara, M. Ishida and M. Anderson, "Visible Luminescence and Surface Properties of Nanosized ZnO Colloids Prepared by Hydrolyzing Zinc Acetate", The Journal of Physical Chemistry B, vol. 102, no. 50, pp. 10169-10175, 1998.

[8] F. Xu and L. Sun, "Solution-derived ZnO nanostructures for photoanodes of dye-sensitized solar cells", Energy Environ. Sci., vol. 4, no. 3, pp. 818-841, 2011.

[9] B. O'Regan and M. Grätzel, "A low-cost, high-efficiency solar cell based on dye-sensitized colloidal TiO2 films", Nature, vol. 353, no. 6346, pp. 737-740, 1991. Available: 10.1038/353737a0. Hierarchically structured photoelectrodes for dye-sensitized solar cells", Journal of Materials Chemistry, vol. 21, no. 19, p. 6769, 2011.

[10] S. Hingorani, V. Pillai, P. Kumar, M. Multani and D. Shah, "Microemulsion mediated synthesis of zinc-oxide nanoparticles for varistor studies", Materials Research Bulletin, vol. 28, no. 12, pp. 1303- 1310, 1993.

[11] M. Choudhury, S. Kato, N. Kishi and T. Soga, "Nickel tetraphenylporphyrin doping into ZnO nanoparticles for flexible dye-sensitized solar cell application", Japanese Journal of Applied Physics,vol. 56, no. 4, pp. 04CS05, 2017.

[12] B. D. Cullity and S. R. Stock, "Diffraction I: Directions of Diffracted Beams," in Elements of X-ray Diffraction,3rd edition, New Jersey, Prentice Hall, 2001, pp. 81-99, 174-177.

[13] H. Sarma and K. C. Sarma, "X-ray Peak Broadening Analysis of ZnO Nanoparticles Derived by Precipitation method," International Journal of Scientific and Research Publications, vol. 4, pp. 1-7, 2014.

[14] Titus, Deena, E. James Jebaseelan Samuel, and Selvaraj Mohana Roopan. "Nanoparticle characterization techniques." In Green Synthesis, Characterization and Applications of Nanoparticles, pp. 303-319. Elsevier, 2019.

[15] Ibrahim Khan, Khalid Saeed and Idrees Khan, ―Nanoparticles: Properties, applications and toxicities‖, *Arabian Journal of Chemistry*, Vol. 12, pp. 908-993, 2019.

[16] Nanoparticles, 19 November, http://www.reachinformation.com/de_ne/nanoparticle.aspx Nanoparticles.

[17] Morris, James E. "Nanoparticle properties." In Nanopackaging, pp. 201-217. Springer, Cham, 2018.

[18] Berni, Anette, Martin Mennig, and Helmut Schmidt. "Doctor blade.", *In Sol-gel technologies forglass producers and users*, pp. 89-92. Springer, Boston, MA, 2004.

[19] Sabir, Sidra, Muhammad Arshad, and Sunbal Khalil Chaudhari. "Zinc oxide nanoparticles forrevolutionizing agriculture: synthesis and applications." The Scientific World Journal 2014 (2014).

[20] Behera, Omkar. "Synthesis and Characterization of ZnO nanoparticles of various sizes andApplications in Biological systems." PhD diss., 2011.

[21] Borysiewicz MA, ―ZnO as a Functional Material, a Review‖, *Crystals,* Vol. 9, pp. 505, 2019.

[22] R. Kumar, A. Umar, G. Kumar, H. S. Nalwa, A. Kumar and M. S. Akhtar, ―Zinc oxide nanostructurebased dye-sensitized solar cells‖, Journal of Materials Science, pp. 3, 2016.

[23] Suntako, Rudeerat. "Cure characteristics and mechanical properties of ZnO nanoparticles as activator in unfilled natural rubber." In Advanced Materials Research, vol. 1044, pp. 23-26. Trans Tech Publications Ltd, 2014.

[24] Goel, Sahil & Kumar, Binay, ―A review on piezo-/ferro-electric properties of morphologically diverse ZnO nanostructures‖, *Journal of Alloys and Compounds,* Vol. 816, pp. 152491, 2019.

[25] Rahman, Faiz, ―Zinc oxide light-emitting diodes: A review‖, *Optical Engineering,* Vol. 58, pp. 1, 2019.

[26] Wu, Yongling Linda, A. I. Y. Tok, Freddy Yin Chiang Boey, Xian Ting Zeng, and Xin Hai Zhang. "Surface modification of ZnO nanocrystals." Applied Surface Science 253, no. 12 (2007): 5473- 5479.

[27] Panda, Debashis, and Tseung-Yuen Tseng. "One-dimensional ZnO nanostructures: fabrication, optoelectronic properties, and device applications." Journal of Materials Science 48, no. 20 (2013): 6849-6877.

[28] Sumetha Suwanboon, Pongsaton Amornpitoksuk, and Phuwadol Bangrak, ―Physical and chemical properties of multifunctional ZnO nanostructures prepared by precipitation and hydrothermal methods‖, *Ceramics International,* Vol. 40, pp. 975-983, 2014.

[29] Theerthagiri, J., Sunitha Salla, R. A. Senthil, P. Nithyadharseni, A. Madankumar, Prabhakarn Arunachalam, T. Maiyalagan, and Hyun-Seok Kim. "A review on ZnO nanostructured materials: energy, environmental and biological applications." *Nanotechnology* 30, no. 39 (2019): 392001.

[30] Schematic diagram of XRD, https://www.researchgate.net/figure/Schematic-diagram-of-XRD- Connolly-2007_fig25_294596476, 13 September 2021.

[31] X-RAY DIFFRACTION (XRD), https://www.rigaku.com/de/node/713 , 13 September 2021.

[32] Hildebrandt, G. "The Discovery of the Diffraction of X-rays in Crystals—A Historical Review." Crystal Research and Technology 28, no. 6 (1993): 747-766.

[33] Eckert, Michael. "Max von Laue and the discovery of X-ray diffraction in 1912." (2012): A83-A85.

[34] Short history of x-ray, https://authors.library.caltech.edu/5456/1/hrst.mit.edu/hrs/materials/public/X-rays/diffraction.htm, 13 September 2021.

[35] Mohite, Rajkkumar M. "Studies of doped and undoped nanostructured zinc oxide thin films for solarcell application." (2015).

[36] X-Ray Crystallography, http://www.tulane.edu/~sanelson/eens211/x-ray, 13 September 2021.

[37] Howatt, G. N., R. G. Breckenridge, and J. M. Brownlow. "Fabrication of thin ceramic sheets forcapacitors." Journal of the American Ceramic Society 30, no. 8 (1947): 237-242.

[38] Dann, Sandra E. Reactions and characterization of solids. Vol. 2. Royal Society of Chemistry, 2000.

[39] Cullity, B., S. R. Stock, and S. Stock. "Elements of X-ray Diffraction, 3rd editionPrentice Hall." New Jersey (2001).

[40] M. S. H. Choudhury, N. Kishi, and T. Soga, -Compression of ZnO nanoparticle films at elevated temperature for flexible dye-sensitized solar cells‖, *Journal of Alloys and Compounds,* Vol. 656, pp. 476-480, 2016.

[41] Gibson P and Holzwarth U, -The Scherrer equation versus the Debye–Scherrer equation‖, *NATURE NANOTECHNOLOGY*, Vol. 6, pp. 534, 2011.

[42] Danilchenko, S. N., O. G. Kukharenko, C. Moseke, I. Yu Protsenko, L. F. Sukhodub, and B. J. C. R. Sulkio-Cleff. "Determination of the bone mineral crystallite size and lattice strain from diffraction line broadening." Crystal Research and Technology: Journal of Experimental and Industrial Crystallography 37, no. 11 (2002): 1234-1240.

[43] Monshi, Ahmad, Mohammad Reza Foroughi, and Mohammad Reza Monshi. "Modified Scherrer equation to estimate more accurately nano-crystallite size using XRD." World journal of nanoscience and engineering 2, no. 3 (2012): 154-160.

[44] Ungár, Tamás, Jenő Gubicza, Gábor Ribárik, and A. Borbély. "Crystallite size distribution and dislocation structure determined by diffraction profile analysis: principles and practical application to cubic and hexagonal crystals." Journal of applied crystallography 34, no. 3 (2001): 298-310.

[45] Biju, V., Neena Sugathan, V. Vrinda, and S. L. Salini. "Estimation of lattice strain in nanocrystallinesilver from X-ray diffraction line broadening." Journal of materials science 43, no. 4 (2008): 1175- 1179.

[46] Nye, John Frederick. Physical properties of crystals: their representation by tensors and matrices. Oxford university press, 1985.

[47] Gibson P and Holzwarth U, -The Scherrer equation versus the Debye–Scherrer equation‖, *NATURE NANOTECHNOLOGY*, Vol. 6, pp. 534, 2011.

[48] Danilchenko, S. N., O. G. Kukharenko, C. Moseke, I. Yu Protsenko, L. F. Sukhodub, and B. J. C. R. Sulkio-Cleff. "Determination of the bone mineral crystallite size and lattice strain from diffraction line broadening." Crystal Research and Technology: Journal of Experimental and Industrial Crystallography 37, no. 11 (2002): 1234-1240.

[49] Monshi, Ahmad, Mohammad Reza Foroughi, and Mohammad Reza Monshi. "Modified Scherrer equation to estimate more accurately nano-crystallite size using XRD." World journal of nanoscience and engineering 2, no. 3 (2012): 154-160.

[50] Ungár, Tamás, Jenő Gubicza, Gábor Ribárik, and A. Borbély. "Crystallite size distribution and dislocation structure determined by diffraction profile analysis: principles and practical application to cubic and hexagonal crystals." Journal of applied crystallography 34, no. 3 (2001): 298-310.

[51] Biju, V., Neena Sugathan, V. Vrinda, and S. L. Salini. "Estimation of lattice strain in nanocrystallinesilver from X-ray diffraction line broadening." Journal of materials science 43, no. 4 (2008): 1175- 1179.

[52] Nye, John Frederick. Physical properties of crystals: their representation by tensors and matrices. Oxford university press, 1985.

[53] Mote, V. D., Yp Purushotham, and B. N. Dole. "Williamson-Hall analysis in estimation of lattice strain in nanometer-sized ZnO particles." Journal of theoretical and applied physics 6, no. 1 (2012): 1-8.

[54] Balzar, Davor, and Hassel Ledbetter. "Voigt-function modeling in Fourier analysis of size- and strain-broadened X-ray diffraction peaks." Journal of Applied Crystallography 26, no. 1 (1993): 97- 103.

[55] Halder, N. C., and C. N. J. Wagner. "Separation of particle size and lattice strain in integral breadth measurements." Acta Crystallographica 20, no. 2 (1966): 312-313.

[56] Karthikeyan, Muthukkumaran, and Sukkee Um. "Synthesis, characterization, and transport properties of single-layer pure and molybdenum-doped vanadium oxide thin films on metallicconductive substrates." Thin Solid Films 606 (2016): 63-73.

[57] Cullity, B. D., and S. R. Stock. "Elements of X-ray Diffraction, 3rd edn Prentice Hall." NewYork (2001): 174-177.

[58] Sarma, Hiten, and K. C. Sarma. "X-ray peak broadening analysis of ZnO nanoparticles derived by precipitation method." International Journal of Scientific and Research Publications 4, no. 3 (2014): 1-7.

[59] Gibson P and Holzwarth U, ‐The Scherrer equation versus the Debye–Scherrer equation‖, *NATURE NANOTECHNOLOGY*, Vol. 6, pp. 534, 2011.

[60] Danilchenko, S. N., O. G. Kukharenko, C. Moseke, I. Yu Protsenko, L. F. Sukhodub, and B. J. C. R. Sulkio-Cleff. "Determination of the bone mineral crystallite size and lattice strain from diffraction line broadening." Crystal Research and Technology: Journal of Experimental and Industrial Crystallography 37, no. 11 (2002): 1234-1240.

[61] Monshi, Ahmad, Mohammad Reza Foroughi, and Mohammad Reza Monshi. "Modified Scherrer equation to estimate more accurately nano-crystallite size using XRD." World journal of nanoscience and engineering 2, no. 3 (2012): 154-160.

[62] Ungár, Tamás, Jenő Gubicza, Gábor Ribárik, and A. Borbély. "Crystallite size distribution and dislocation structure determined by diffraction profile analysis: principles and practical application to cubic and hexagonal crystals." Journal of applied crystallography 34, no. 3 (2001): 298-310.

[63] Biju, V., Neena Sugathan, V. Vrinda, and S. L. Salini. "Estimation of lattice strain in nanocrystallinesilver from X-ray diffraction line broadening." Journal of materials science 43, no. 4 (2008): 1175- 1179.

[64] Nye, John Frederick. Physical properties of crystals: their representation by tensors and matrices. Oxford university press, 1985.

[65] Mote, V. D., Yp Purushotham, and B. N. Dole. "Williamson-Hall analysis in estimation of lattice strain in nanometer-sized ZnO particles." Journal of theoretical and applied physics 6, no. 1 (2012): 1-8.

[66] Balzar, Davor, and Hassel Ledbetter. "Voigt-function modeling in Fourier analysis of size- and strain-broadened X-ray diffraction peaks." Journal of Applied Crystallography 26, no. 1 (1993): 97- 103.

[67] Halder, N. C., and C. N. J. Wagner. "Separation of particle size and lattice strain in integral breadth measurements." Acta Crystallographica 20, no. 2 (1966): 312-313.

[68] Karthikeyan, Muthukkumaran, and Sukkee Um. "Synthesis, characterization, and transport properties of single-layer pure and molybdenum-doped vanadium oxide thin films on metallicconductive substrates." Thin Solid Films 606 (2016): 63-73.

[69] Cullity, B. D., and S. R. Stock. "Elements of X-ray Diffraction, 3rd edn Prentice Hall." NewYork (2001): 174-177.

[70] Sarma, Hiten, and K. C. Sarma. "X-ray peak broadening analysis of ZnO nanoparticles derived by precipitation method." International Journal of Scientific and Research Publications 4, no. 3 (2014): 1-7.

[71] Gibson P and Holzwarth U, ‐The Scherrer equation versus the Debye–Scherrer equation‖, *NATURE NANOTECHNOLOGY*, Vol. 6, pp. 534, 2011.

[72] Gibson P and Holzwarth U, ‐The Scherrer equation versus the Debye–Scherrer equation‖,

NATURE NANOTECHNOLOGY, Vol. 6, pp. 534, 2011.

[73] Danilchenko, S. N., O. G. Kukharenko, C. Moseke, I. Yu Protsenko, L. F. Sukhodub, and B. J. C. R. Sulkio-Cleff. "Determination of the bone mineral crystallite size and lattice strain from diffraction line broadening." Crystal Research and Technology: Journal of Experimental and Industrial Crystallography 37, no. 11 (2002): 1234-1240.

[74] Monshi, Ahmad, Mohammad Reza Foroughi, and Mohammad Reza Monshi. "Modified Scherrer equation to estimate more accurately nano-crystallite size using XRD." World journal of nanoscience and engineering 2, no. 3 (2012): 154-160.

[75] Ungár, Tamás, Jenő Gubicza, Gábor Ribárik, and A. Borbély. "Crystallite size distribution and dislocation structure determined by diffraction profile analysis: principles and practical application to cubic and hexagonal crystals." Journal of applied crystallography 34, no. 3 (2001): 298-310.

[76] Biju, V., Neena Sugathan, V. Vrinda, and S. L. Salini. "Estimation of lattice strain in nanocrystallinesilver from X-ray diffraction line broadening." Journal of materials science 43, no. 4 (2008): 1175- 1179.

[77] Nye, John Frederick. Physical properties of crystals: their representation by tensors and matrices. Oxford university press, 1985.

[78] Mote, V. D., Yp Purushotham, and B. N. Dole. "Williamson-Hall analysis in estimation of lattice strain in nanometer-sized ZnO particles." Journal of theoretical and applied physics 6, no. 1 (2012): 1-8.

[79] Balzar, Davor, and Hassel Ledbetter. "Voigt-function modeling in Fourier analysis of size- and strain-broadened X-ray diffraction peaks." Journal of Applied Crystallography 26, no. 1 (1993): 97- 103.

[80] Halder, N. C., and C. N. J. Wagner. "Separation of particle size and lattice strain in integral breadth measurements." Acta Crystallographica 20, no. 2 (1966): 312-313.

[81] Karthikeyan, Muthukkumaran, and Sukkee Um. "Synthesis, characterization, and transport properties of single-layer pure and molybdenum-doped vanadium oxide thin films on metallicconductive substrates." Thin Solid Films 606 (2016): 63-73.

[82] Cullity, B. D., and S. R. Stock. "Elements of X-ray Diffraction, 3rd edn Prentice Hall." NewYork (2001): 174-177.

[83] Sarma, Hiten, and K. C. Sarma. "X-ray peak broadening analysis of ZnO nanoparticles derived by precipitation method." International Journal of Scientific and Research Publications 4, no. 3 (2014): 1-7.